Dissertation

Thermodynamic stability and mechanical properties of nanocrystalline high-entropy alloys

Benjamin Schuh

Leoben, October 2018

This work was financially supported by the Austrian Science Fund (FWF) in the framework of research project P24429 and by the European Research Council under ERC Grant Agreement No. 340185 USMS.

Erich Schmid Institute of Materials Science

Austrian Academy of Sciences

Jahnstraße 12

Affidavit

I declare in lieu and oath, that I wrote this thesis and performed the associated research myself, using only literature cited in this volume.

Leoben, October 2018

Danksagung

Zuerst möchte ich mich bei Professor Reinhard Pippan und Dr. Anton Hohenwarter für die Übertragung und Betreuung dieser Dissertation bedanken, denn ohne Euch wäre diese einzigartige Erfahrung nicht möglich gewesen. Besonderer Dank gilt dabei Toni, der mir über all die Jahre immer mit Rat und Tat zur Seite gestanden hat und der es mir ermöglicht hat unsere Forschungsarbeit auf zahlreichen Konferenzen zu präsentieren.

Große Wertschätzung will ich hier auch für Peter Kutleša, Herwig und Gabi Felber, Silke Modritsch, Robin Neubauer und Franz Hubner ausdrücken, die mit ihrer tollen Unterstützung in allen technischen und metallographischen Belangen den Erfolg dieser Dissertation erst möglich gemacht haben. Ein besonderer Dank gilt dabei auch Sabine Wilfling und Daniela Brunner, die mir in organisatorischen Angelegenheiten immer unter die Arme gegriffen haben und auch die abenteuerlichsten Dienstreise-Urlaubskombinationen geduldig ertragen haben.

Vielen Dank gilt auch meinen Bürokollegen Patrice Kreiml, Sabine Bodner und Andreas Umgeher für die lockere und lustige Atmosphäre im Büro, die auch den mühsamsten Tag immer erträglich gemacht hat. Insbesondere möchte ich mich auch bei Oliver Renk für die vielen motivierenden Gespräche und die tolle Hilfe über all die Jahre bedanken. Für die großartige Stimmung am Institut sowie den kollegialen und ungezwungenen Umgang miteinander möchte ich mich auch bei all meinen Mit-Dissertanten, den Post-Docs und Studenten am ESI bedanken, die ich über so viele Jahre Freunde und Kollegen nennen durfte. Dank Euch bin ich auch an schwierigen Tagen jedes Mal gerne auf das Institut gekommen und ihr habt für unvergleichliche Arbeitsbedingungen gesorgt, die die Jahre wie im Flug vergehen ließen. Meine Anerkennung will ich hier auch für Bernhard Völker ausdrücken, der mich über viele Jahre hinweg mit TEM Untersuchungen unterstützt hat. Insbesondere möchte ich mich auch bei Barbara Putz, Andreas Kleinbichler und Vladica Nikolić für die vielen tollen Aktivitäten außerhalb des Instituts bedanken. Danke Vladi für die freundschaftlichen Ratschläge und die lustigen Reisen nach den Konferenzen. Ebenso großer Dank gilt auch Karoline Kormout für die amüsanten Tratschpausen und die Begleitung durch diverse amerikanische und japanische Spelunken.

Ihr habe ich es auch zu verdanken, dass ich Lisa Kormout kennen gelernt habe, die das letzte Jahr meiner Dissertation zu etwas ganz Besonderem gemacht hat. Von ganzem Herzen danke ich Dir für Deine liebevolle Unterstützung, die diese turbulente Zeit um so vieles ruhiger und schöner gemacht hat und für die unvergessliche Zeit außerhalb des Institutes.

Zu guter Letzt möchte ich natürlich auch meiner Familie danken, deren Rückhalt mein Studium und die Dissertation erst ermöglicht hat. Vielen Dank, dass ihr mich bei all meinen Plänen immer unterstützt.

Abstract

High-entropy alloys (HEAs) are a new class of multi-component metallic alloys that recently have been introduced to the scientific community. As a result of their sometimes outstanding properties in regards to their mechanical behavior, as well as their corrosion and oxidation resistance, they have gained much interest as potential candidate alloys for future structural applications. The main work performed in this thesis was on one promising, high-performance, face-centered cubic alloy, CrCoNi, and two body-centered cubic HEAs, AlTiVNb and TiZrNbHfTa. These alloys were processed via high-pressure torsion in order to achieve a nanocrystalline microstructure and subsequently subjected to various annealing treatments. This was done for two reasons: I) The thermodynamic stability of the alloys could be probed by the ensuing microstructural investigations on the annealed samples. II) Microstructure-property relationships could be established by mechanical testing of the nanocrystalline and heat-treated materials.

The performed studies were among the first to investigate these materials in the nanocrystalline state. It was demonstrated that in this grain size regime the CrCoNi alloy is competitive in regards to its performance in tensile tests with a comparable structural material, 316L steel. Additionally, the nanocrystalline TiZrNbHfTa alloy showed outstanding properties by retaining almost the same level of ductility compared to the coarse-grained material, while the tensile strength was more than doubled. By performing systematic annealing studies it could be shown that, while the investigated alloys were frequently believed to be stable, single-phase alloys, the (near) equilibrium microstructures of the alloys include multiple phases over an extended temperature range. This has important implications since, in the case of both bcc alloys, the ensuing phase decompositions lead to a strong deterioration of the mechanical properties, especially ductility. This could severely influence their feasibility as structural materials. Interestingly, the CrCoNi alloy was highly prone to abnormal grain growth, which enabled the possibility of engineering a bimodal distribution of grain sizes, a frequently suggested strategy to reach outstanding combinations of strength and ductility. By employing this method one microstructural state with an ultra-high tensile strength and a significantly increased elongation to failure compared to the nanocrystalline material could be achieved.

In conclusion, the performed work sheds new light on the mechanical behavior as well as the microstructural and thermal stability of HEAs in the nanocrystalline grain size regime.

Table of Content

1.

Motivation and aim of the present work

High-entropy alloys (HEAs) are a new class of multicomponent metallic materials that have recently been introduced to the scientific community [1,2]. They sometimes show supreme properties in comparison to commercially available materials in regards to mechanical properties [3–5], but also corrosion [6,7] and oxidation resistance [8,9]. Therefore, HEAs have attracted a massive research interest, as can be seen easily on the ever-growing number of publications, Figure 1. The main reason for the ongoing interest in HEA research lies in the vast compositional space possible to explore [10–12]. Traditional alloying approaches usually rely on a single-base element, hence composition wise a majority of alloys are only located at the edges of the phase diagrams, while HEA research aims to investigate the centers of the phase diagrams. This, in addition with the loose definition of HEAs, gives rise to a colossal number of possible alloys. While the enormous number of HEAs suggest a strong likelihood of interesting discoveries, it also emphasizes one of the greatest challenges in current HEA research – the need for efficient high-throughput experimental techniques [11,12].

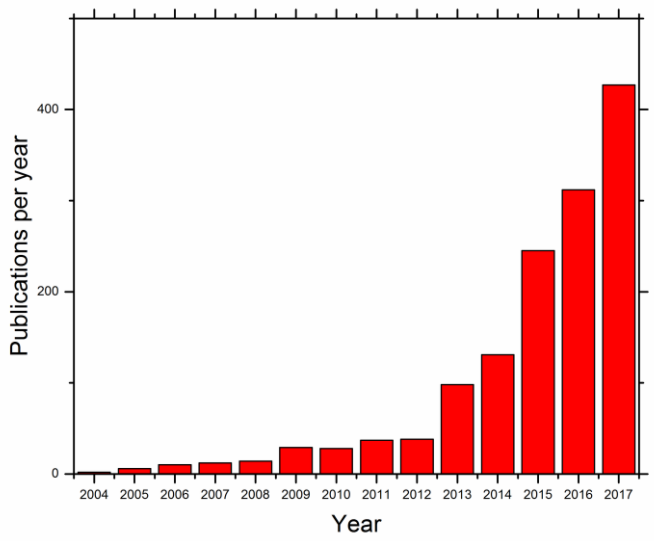

Figure 1: Number of HEA publications per year according to Scopus [13].

In the first decade of HEA research a strong focus was the search for single-phase alloys – however, a majority of investigations were performed after casting and in non-equilibrium conditions, which often lead to inaccuracies regarding the thermodynamic stability and the equilibrium microstructures of the reported alloys [12,14,15]. Additionally, many studies solely relied on X-ray diffraction (XRD) data for determining the number of phases present, however, this technique has deficiencies if second phases only occur in small volume fractions.

The starting point of the thesis was an investigation of the author on the microstructural stability of a prototype HEA system, the equiatomic CrMnFeCoNi alloy, which was believed to be a single-phase, face-centered cubic (fcc) alloy with an exceptional thermal stability [16,17]. Nonetheless, after low temperature annealing treatments of nanocrystalline (NC) specimens a phase decomposition occurred, which greatly changed the mechanical properties of the material [18]. This initiated further investigations into popular "single-phase" HEA systems to analyze their thermodynamic stability and to probe the concept of entropic stabilization. Therefore, one subvariant of the CrMnFeCoNi alloy with a lower configurational entropy, the equiatomic CrCoNi alloy, was studied. Additionally, two equiatomic, body-centered cubic (bcc) refractory HEA (RHEA) systems were investigated, the AlTiVNb and the TiZrNbHfTa alloy. Such RHEA systems are commonly thought of as candidate alloys in the high temperature regime in the future [19–21].

These alloys were processed down to a NC grain size regime, with the following motivations:

- NC materials feature an abundance of grain boundaries, which act as fast diffusion pathways and preferential nucleation sites for second phases. Therefore, studies of thermodynamic stability can be performed within very reasonable time-frames.

- High-resolution techniques, such as transmission electron microscopy or atom probe tomography only allow the investigation of a very limited sample volume. As a consequence, site specific preparation techniques are often required in coarse grained materials to study certain features, such as grain boundary segregation. In NC materials even in such small samples several grains as well as grain boundaries are usually present and therefore often all features of interest are included in a single sample.

- In order to evaluate if HEAs in the NC grain size regime behave mechanically different than conventional alloys. Along with this motivation, it was possible to study the effect of additional phases in NC materials. From NC-synthesis it is known that certain limitations in the achievable strength are given. Therefore, nowadays a lot of research is devoted to study nanocomposite materials. Such composites can also be achieved by exploiting the thermodynamic instability in HEAs.

Subsequent heat treatments often revealed dramatic changes in the microstructure and mechanical properties of the investigated alloys over an extended temperature range. All publications are the first or among the first to show these thermodynamic instabilities of the reported alloys in the NC grain size regime, which has important implications regarding their feasibility as candidate alloys for future structural applications.

The thesis starts with a basic introduction to HEAs and a set of important properties attributed to such alloys, named the "core effects", which are currently highly controversially discussed, and partly also disproved, in the literature. It is followed by a summary of the obtained results, which also comprises of a short conclusion highlighting the novelty of the performed research and an outlook into future research. In the last part of the thesis all publications are attached.

2.

Introduction

2.1 High-Entropy Alloys

HEAs are a novel type of alloys that got first introduced to the research community in 2004 [1,2]. The original definition of HEAs was "alloys composed of five or more principal elements in equimolar ratios" [2]. An alternative was also named, which has become the most common definition of HEA systems to date, namely that a HEA is any multicomponent alloy, where the principal elements are distributed between 5 at.% and 35 at.% [2]. Early on some suggestions were based on the configurational entropy, claiming that the configurational entropy should at least be 1.61*R (R is the gas constant, 8.31 J/(K*mol)), which equals the configurational entropy of an equiatomic quinary alloy assuming an ideal solid solution [12,22]. Also a minimum configurational entropy of 1.5*R was often stated [10,23]. However, such entropy based definitions are rarely used today.

A principal idea behind HEAs is to stabilize a single disordered solid-solution phase by having an extraordinary high configurational entropy ("entropic stabilization") [2,24,25]. This idea of a phase stabilization by engineering an extraordinary high configurational entropy strongly influenced early HEA research. The chemical complexity of these alloys and the fact that no clear solvent/solute exists is also thought to significantly influence HEA properties, such as diffusivity and the mechanical behavior. These concepts were summarized as the four "core effects" by Yeh et al. [25–27]. In recent years, these "core effects" have become increasingly controversial, since they often cannot be substantiated by experimental findings. A short description and discussion of these effects can be found in the following. For a more detailed review the reader is also referred to the articles by Pickering et al. [23] and especially Miracle et al. [12], where particularly the thermodynamics of HEAs are extensively discussed.

Lastly, it also has to be noted that the terminology "high-entropy alloy" is currently under intense debate in the community due to the controversy mentioned above. Therefore, alternative names for this alloy type have been suggested, such as "compositionally complex alloys" [11] and "multiple principal element alloys" [23], and often entail slightly different definitions. The term "compositionally complex alloy" seems to be the most accurate and includes no limitations in the number of occurring phases. In contrast, the term HEA would strictly only be applicable to single-phase alloys. In order to avoid confusion the term HEA will nonetheless be used for all alloys discussed in the introductory part of this work.

2.2 The "Core Effects"

2.2.1 High Entropy Effect

The high-entropy effect is the key concept of HEAs. It states that a HEA should be able to stabilize a single disordered solid solution phase rather than forming various intermetallic phases, which might be an issue, regarding the complex chemical compositions of these alloys. This was explained by the fact that a sufficiently high configurational entropy should be able to overcome the very negative enthalpy of formation of intermetallic phases, especially considering that the configurational entropy of ordered intermetallic phases should be negligible [14,25].

In order to determine which phases are thermodynamically stable in an alloy at a given pressure and temperature, the state with the lowest Gibbs Free Energy of mixing ΔG_{mix} is determined by:

$$\Delta G_{mix} = \Delta H_{mix} - T * \Delta S_{mix}, \qquad \textbf{Equation 1}$$

where T is the temperature, ΔH_{mix} the enthalpy of mixing and ΔS_{mix} the entropy of mixing. When discussing HEAs it is often assumed that the configurational entropy is so dominant that other entropy-contributions can be ignored and ΔS_{mix} is expressed in the form of the Boltzmann equation, where c_i is the mole fraction of the i-th component [28]:

$$\Delta S_{mix} = -R * \sum_{i=1}^{n} c_i * ln(c_i). \qquad \textbf{Equation 2}$$

There are multiple problems with this approach. Firstly, the Boltzmann equation assumes that the solid solution is either an ideal or a regular solution, which means that atoms are distributed in a random fashion. However, a vast majority of solid solutions are sub-regular [29]. This means that the Boltzmann equation should overestimate the configurational entropy of most HEAs. Moreover, in sub-regular solid solutions, the point of maximum configurational entropy is shifted away from the equiatomic composition [12]. Secondly, it has been shown by recent studies that other contributions to the overall entropy of a phase are often not negligible in HEAs [12,30]. Other contributions to entropy are:

1) Vibrational Entropy
2) Magnetic Entropy
3) Electronic Entropy
4) Excess configurational entropy

in which 1) originates from lattice vibrations, 2) from local magnetic moments, 3) from the probabilistic occupation of electron states and 4) from displacing solvent atoms from their ideal lattice position by introducing differently sized solute atoms. Ma et al. investigated the influence of the first three contributions via *ab initio* simulations on an equiatomic CrMnFeCoNi alloy [30]. They came to the conclusion that by far the largest contribution was stemming from the vibrational entropy (at elevated temperatures). It has to be noted that when looking at the thermodynamic competition between different phases, only the relative difference of the thermodynamic parameters is of importance. In this regard Miracle et al. pointed out the difference in vibrational entropies between different phases is usually quite low [12]. On the other hand, electronic and magnetic contributions in the CrMnFeCoNi alloy can reach up to 50% of the configurational entropy and thus are sometimes non-negligible [30]. Additionally, the total entropies of binary liquid alloys were analyzed and it was concluded that the contribution of vibrational, magnetic and

electronic entropy terms can vary strongly, depending on the alloy, and can range from almost 0 % to approximately 70 % [12]. Regarding 4), excess configurational entropy, it is straightforward to assume that the contribution will get more significant when atom size differences and solute concentrations are increased [12]. However, no in-depth analysis of the importance of this term in regards to HEAs exists so far in the literature to the best of the author's knowledge.

Lastly, some publications excellently demonstrate that a high configurational entropy alone is insufficient to ensure phase stability. The first one is surprisingly the pioneering work, which introduced the HEA concept, by Cantor et al. [1]. Multicomponent alloys with 16 and 20 elements in equal composition were cast, melt-spun and analyzed. In all cases a multi-phase structure was the result. While one of these phases was the "work-horse" HEA, an equiatomic CrMnFeCoNi phase (hence, it is also often referred to as the "Cantor" alloy) it also demonstrates that arbitrarily mixing elements will not result in stable, single-phase HEAs. This was also demonstrated by utilizing the CALPHAD approach by Senkov et al. [31]. The main conclusion was that, in contradiction to the HEA concept, the number of microstructures solely consisting of solid solution phases strongly decreases with an increase in the number of alloying elements. Additionally, Otto et al. [16] concluded that, while entropic stabilization might work in a few selected systems, it is usually insufficient to counteract the driving forces that favor the formation of secondary phases. This conclusion was made after an in-depth study on the phase stability of the CrMnFeCoNi system by changing the composition with chemically similar elements one at a time.

2.2.2 Severe Lattice Distortion

If solute atoms are alloyed to a solvent metal, they will cause a displacement of their neighbors from their original lattice position. This results in an elastic distortion of the crystal lattice, which has profound impacts on a multitude of material properties, such as mechanical strength [32], electrical/thermal resistivity [33] and ultimately also the thermodynamic stability [34] of the alloy. In HEAs a complex situation arises: Firstly, there is a large number of principal elements, which can vary in their atomic sizes and elastic properties significantly. Secondly, given the often (near-) equiatomic chemical composition, no clear solvent exists. This should give rise to a lattice distortion more severe than in conventional alloys, a schematic of what such a lattice could look like is given in Figure 2. This was early on supported by experimental evidence such as XRD and mechanical data [25]. In XRD data it is thought that such a strong lattice distortion causes a peak decrease due to diffuse scattering, such as usually seen from thermal vibrations, while hardness data supports the hypothesis by claiming the increased hardness of some HEAs originates from an inherently strong solid solution strengthening [25,35] – however, this generalization of a high mechanical strength of HEAs is rather questionable, considering that the strength of many single-phase fcc HEAs is not higher than comparable structural materials, such as TWIP steels [36–39]. More recent, high-quality experiments to assess the lattice distortion in HEAs shed a more controversial light on the topic. A study by C. Lee investigated single-phase fcc alloys of increasing chemical complexity via XRD and could show a strong decrease of XRD peak intensity when approaching HEA compositions [40]. However, such a decrease can originate from many sources, both from inherent physical features of the material, such as crystallographic texture but also from instrumental effects [41]. Contrarily, a combined study of simulation linked with experiments on the equiatomic CrMnFeCoNi HEA showed that the lattice distortions are rather small when considering them on a more macroscopic scale [42]. Additionally, a study by Owen et al. utilizing neutron diffraction could show that, while there was evidence of a lattice distortion in the investigated HEA system, it is not more severe than in other highly alloyed materials, such as Ni-33Cr [41]. Complementary to such experimental

results, predictive studies using the density functional theory showed that the lattice distortion in a VNbMoTaW alloy is no larger than 5 % of the lattice parameter, which is a level of distortion also found in binary concentrated solid solutions [23,43].

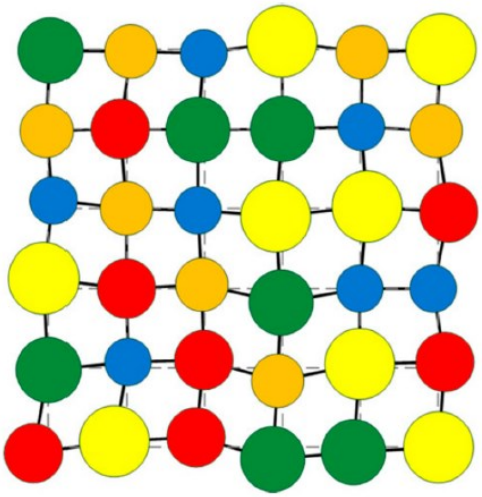

Figure 2: Schematic of a severely distorted lattice, taken from [22]

A rather convincing, qualitative argument, why the existence of severely distorted lattices is highly unlikely, was also brought forth by Pickering et al. [23]. Elastic strains of the crystal lattice inherently increase the Gibbs Free Energy, thus counteracting any stabilization gained by the increased (excess) configurational entropy. This makes the existence of severe lattice strains and the simultaneous thermodynamic stability of such a lattice questionable.

In conclusion, while early studies supported the existence of a severe lattice distortion in HEAs, new experiments indicate that the lattice distortion in HEAs is not significantly more pronounced than in conventional, highly alloyed materials.

2.2.3 Sluggish Diffusion

The diffusion kinetics in HEAs should be abnormally slow compared to conventional alloys due to their complex chemical composition. The fluctuations in the potential energy of lattice sites are supposed to give rise to especially deep diffusion traps, see Figure 3 [26]. This sluggish diffusion was proposed in early studies based on observations such as slow grain growth or precipitation kinetics [12,24,44]. Only few reports of directly measured diffusion data exist in the literature to date. Firstly, Tsai et al. measured diffusion coefficients in Co–Cr–Fe–Mn–Ni alloys and concluded that diffusion was indeed slower in the HEA than in the reference materials [45]. These results were challenged due to the fact that differences in diffusion coefficients of one order of magnitude are not significant given the difficulty of acquiring precise diffusion data [12]. A radio-tracer study of self-diffusion in the CrMnFeCoNi alloy was performed by Vaidya et al. [46], concluding that tracer diffusion in HEAs is only sluggish if the homologous temperature is considered and that diffusion in HEAs is not inevitably retarded. In a later publication, the grain boundary diffusion kinetics in HEAs were studied and it was demonstrated that the assumption of a decreasing diffusivity by increasing the number of elements is incorrect [47]. A recent study by Gaertner et al. [48] also used tracer diffusion to determine self-diffusion coefficients in the CrFeCoNi and CrMnFeCoNi alloy and came to the conclusion that diffusion in these HEAs is not retarded.

In summary, secondary observations, such as grain growth kinetics, are insufficient to make precise statements concerning the diffusion behavior of materials, since they are depending on a multitude of physical and microstructural parameters. Recent diffusion data point into the direction that sluggish diffusion should not be universally assumed for all HEAs.

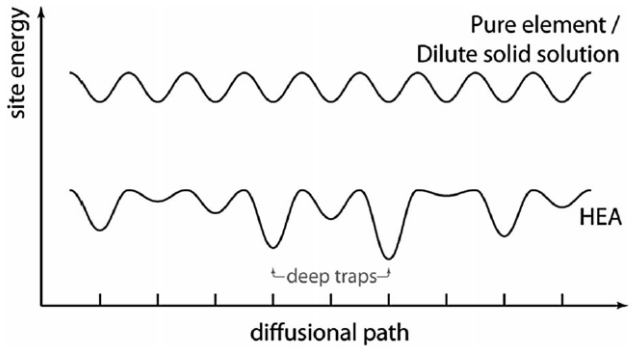

Figure 3: Schematic of how the strong variation in the potential energy of lattice sites gives rise to deep diffusion traps. Figure taken from [23].

2.2.4 Cocktail Effect

The cocktail effect was coined in the article "Alloyed Pleasures: Multimetallic Cocktail" [49] and was not attributed uniquely to HEAs, but used to discuss modern trends in metallurgy. To the best of the author's knowledge, the cocktail effect never has been exactly defined in the literature, at least not in regards to materials science. The term cocktail (party) effect was popularized in psychology, where it was used to describe the brains ability to focus on a single conversation in an otherwise noisy room, while ignoring other stimuli [50]. Focusing on material science, interpretations of the cocktail effect include that some properties cannot be approximated from linear interactions between the different elements and phases [42], but also that in synergistic mixtures the resulting properties can be greater than the sum of its parts [12,22]. However, none of these descriptions can exclusively be attributed to HEAs and therefore it was even suggested that the " Cocktail Effect" could be dismissed as a "core effect" [23]. Recently, Miracle et al. recommended that the cocktail effect should not be treated as a scientific hypothesis, but rather as an idea to "remain open to non-linear, unexpected results that can come from unusual combinations of elements in the vast composition space of multiple-principal elements alloys" [12].

2.2.5 Concluding remarks

To conclude, even though these four "core effects" are often found in the literature and praised to be fundamental for the understanding of HEAs, this critical discussion should have shown the connected discrepancies. In a strict view, the significance of the "core effects" is rather of historical than of scientific importance, which is the main reason to treat them in this thesis.

3.

Summary of the results

3.1 Investigated materials and processing

Two equiatomic fcc materials were investigated, the CrCoNi alloy as well as the CrMnFeCoNi alloy (in a prior study). Since the work on the CrMnFeCoNi alloy was not strictly a part of this thesis it is not included in the appended papers, some of the results and their impact will still be discussed. The corresponding publication can be found elsewhere [18].

The CrCoNi and the CrMnFeCoNi alloy have shown outstanding mechanical properties in the cryogenic temperature range. Especially the CrCoNi alloy, which has a fracture toughness at crack initiation K_{JIC} of more than 270 MPa*$m^{1/2}$ at 77 K, which makes it the toughest HEA known to date [3,51,52]. Both alloys show outstanding properties during tensile testing, featuring an excellent ductility, high work hardening rate and a yield strength that is comparable to commercially available materials such as TWIP steels [3,4,36,38,39]. Additionally, two equiatomic bcc RHEAs were also investigated, namely the AlTiVNb and the TiZrNbHfTa alloys. RHEAs are often suggested as potential candidate alloys for future structural application in the high temperature regime [21,53– 55]. The AlTiVNb alloy's main advantages are its low density and outstanding mechanical performance during high-temperature compression tests [55,56]. The most attractive property of the TiZrNbHfTa system is its substantial room temperature ductility compared to other bcc HEAs [57]. Therefore, it is already relatively well characterized in regards to its mechanical properties and deformation mechanism for coarse-grained microstructures [19,58–61]. Since the production of these alloys is very different, the reader is referred to the experimental details of the appended publications. The common denominator is that all alloys were produced from high-purity elements in an equiatomic composition and subsequently processed to achieve a NC microstructure. There is a number of techniques that can be employed in order to achieve a NC microstructure. They are divided into two groups, I) bottom-up and II) top-down techniques. I) includes processes such as electrodeposition or inert-gas-condensation [62], while II) features severe plastic deformation (SPD) techniques, where a bulk sample is subjected to enormous strains, which leads to an extraordinary grain refinement. Popular SPD techniques are high-pressure torsion (HPT), accumulative roll bonding and equal angular channel pressing [63– 65]. In all of the studies performed in this thesis, HPT was exclusively used in order to obtain NC microstructures.

During HPT processing a disk shaped specimen is placed between two anvils and is subjected to a high (quasi-) hydrostatic pressure as well as torsional deformation by rotating one of the anvils against the other. The applied shear strain γ can be estimated using Equation 3.

$$\gamma = \frac{2\pi r n}{t} \ (-) \qquad \textbf{Equation 3}$$

Here, r is the radius, t the sample thickness and n the number of rotations the specimen has undergone. Due to the nature of this process a strain gradient is imposed on every sample, however, by applying sufficiently high strains microstructural homogeneity still can be ensured. The main advantage of the process is that brittle materials can be deformed to high strains as well, even at room temperature. Moreover, the resulting NC bulk samples are dense and usually free of porosity or similar flaws, which is essential for the determination of correct mechanical properties during subsequent tests. One disadvantage is the limited sample size. For more details on the HPT process, as well as its advantages and limitations, the reader is referred to [66,67].

In the presented publications all samples were deformed at room temperature, with a pressure of 7.8 GPa and a rotational speed of 0.2 rotations/min. The specimens were deformed for 5 rotations to ensure microstructural homogeneity.

3.2 Deformation mechanisms during HPT processing

For all samples the NC steady-state microstructure for the corresponding material was used as a starting point to perform annealing experiments in order to investigate the thermodynamic stability of the single-phase HEAs. Hereinafter, the microstructural changes that the alloys underwent before reaching the NC grain size regime will be shortly summarized. Both the CrMnFeCoNi alloy as well as the CrCoNi alloy have a deformation behavior characteristic of low stacking fault energy (SFE), single-phase fcc materials and can be compared to austenitic steels [68]. The microstructural evolution is described in the following, however, it has to be noted that relative terms, such as “low” strains, is related to strains commonly imposed during HPT processing, which can be orders of magnitudes larger than typical strains usually associated with, for example, tensile testing.

At low applied shear strains dislocation glide is the dominant deformation mechanism. If the strain is increased profuse mechanical twinning as well as micro-shear banding occur. At even higher strains alternative twin systems are often activated and mechanical twins start to intersect each other, leading to a strong grain refinement. A representative example of this, showcasing the CrCoNi alloy, can be found in Figure 4 a), depicting a low deformation area near the sample center and Figure 4 b), where substantial strains already have been applied.

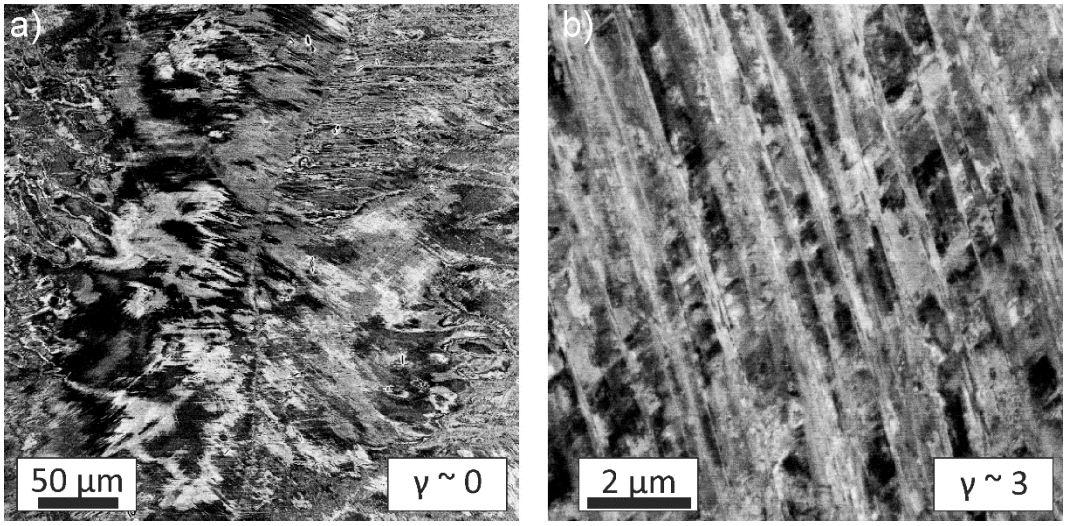

Figure 4: Back-scattered electrons (BSE) micrographs of the deformed CrCoNi alloy. a) shows the microstructure near the sample center (ideally $\gamma = 0$). b) features intersecting mechanical twins after substantial shear strains have been applied**.**

In both bcc HEAs deformation at low strains is prevailed by dislocation mediated slip, as can be seen by the formation of dislocations substructures in Figure 5 a), where the TiZrNbHfTa alloy is shown. An additional feature of the TiZrNbHfTa alloy is the formation of lenticular structures, as has been reported before [58]. Senkov et al. described these structures as a mixture of shear bands and mechanical twins, however, in the presented work no conclusive proof could be found that these structures are related to mechanical twins. Even at very low strains a strong localization of deformation in the form of band-like structures occurs. This leads to a rather inhomogeneous microstructure, where grain refinement is much stronger inside the bands than in the surrounding material, see Figure 5 b). In case of the TiZrNbHfTa alloy such a deformation localization is well reported [19,59,69].

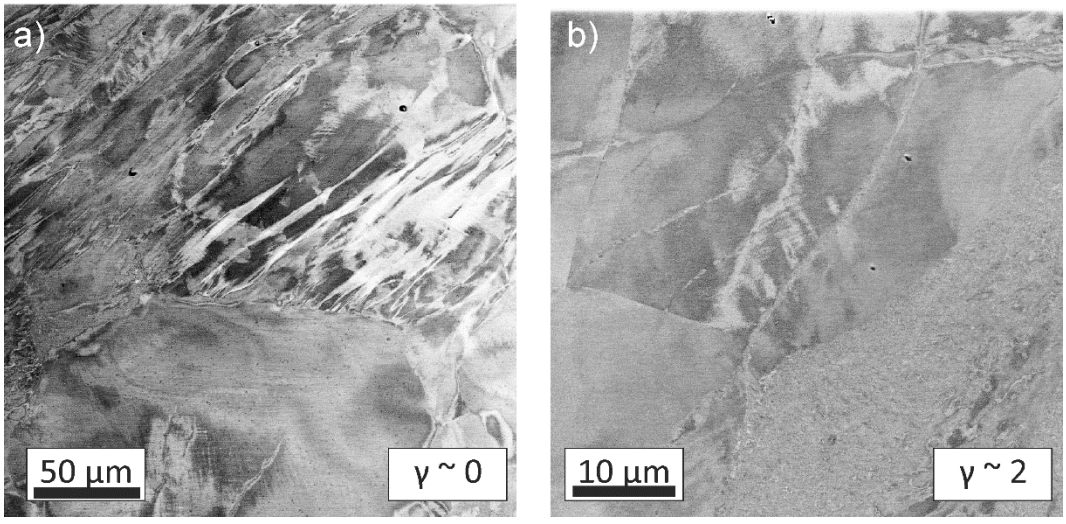

Figure 5: BSE micrographs of the TiZrNbHfTa alloy after deformation. a) shows the formation of dislocation substructures as well lenticular features near the disk center. In b) the localization of deformation into shear bands can be seen, where the microstructure inside the bands is much finer than in the surrounding material.

3.3 Steady-State microstructures

In single-phase metals a steady-state microstructure can be achieved via HPT processing, which means that after a certain strain has been applied, no essential changes to important microstructural features are occurring any more, even if the strain is increased further. This can be explained by the fact that an equilibrium between the grain refinement via HPT and dynamic recovery processes is reached. Furthermore, this also implies that only a certain minimum grain size can be achieved. This steady-state grain size is dependent on various physical and technological parameters. The most influential factors are the materials properties, its purity and the deformation temperature [70]. Other influences are the strain rate [71] and in some cases also the applied pressure [72]. In all appended publications an approximate steady state grain size of about 50 nm was achieved, which was determined via transmission electron microscopy dark-field (TEM-DF) imaging after shear strains of $\gamma > 50$ were applied. An example of such a steady-state microstructure for the CrCoNi alloy can be found in Figure 6 a). Generally, SPD processed materials often feature blurred and ill-defined structures, which is attributed to the existence of non-equilibrium grain boundaries [73]. The occurrence of a microstructural equilibrium is also very well reflected in the mechanical properties of the material. In Figure 6 b) the hardness is plotted as a function of the shear strain and it can be seen that at a shear strain of about 50 all curves level off into a plateau.

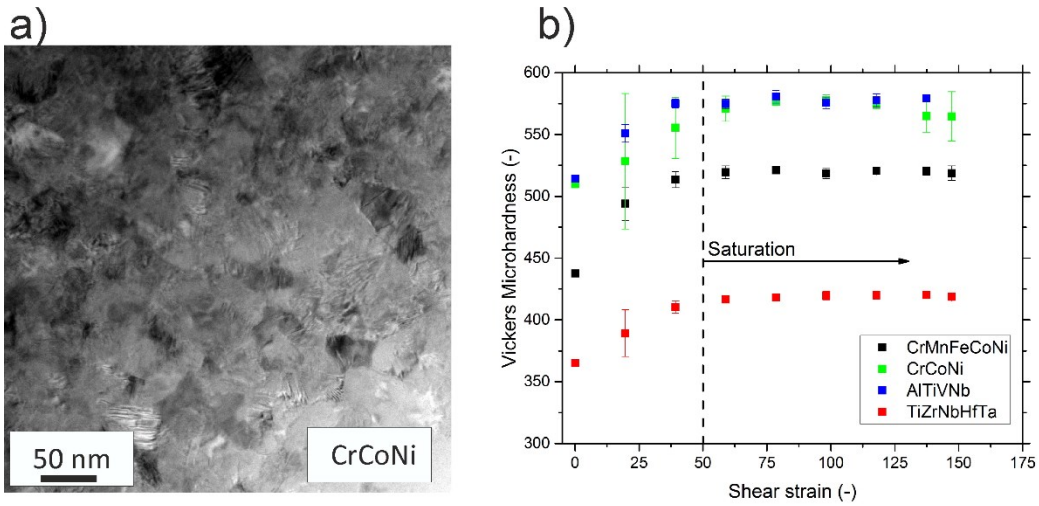

Figure 6: a) STEM image of the CrCoNi alloy in the steady-state regime after HPT processing. The grain size is approximately 50 nm. b) Hardness evolution as a function of the shear strain during HPT processing for all investigated HEA systems. The hardness of all alloys saturates at a shear strain of about 50.

3.4 Mechanical properties of nanocrystalline high-entropy alloys

Due to the extraordinary structural refinement achievable by HPT it commonly produces high-strength materials [65–67,70,73], as can be seen in Figure 7. The ultimate tensile strength is increased from approximately 460 MPa for a coarse-grained CrCoNi alloy (grain size > 100 μm) to roughly 2000 MPa for the NC microstructure after HPT processing. Similar tensile strengths can also be achieved with commercially available materials, for instance, an austenitic A220 steel from Böhler (equivalent to grade 316L steel). While impressive strengths can be reached, a common problem of a majority of NC materials is the limited ductility. Usually, fracture occurs after only little macroscopic plastic deformation, as can be seen in both materials shown in Figure 7 a). Two aspects have been identified as the main reasons for the ductility problem in NC materials [74]: I) poor sample quality can lead to a cracking instability/brittle failure and II) the low capacity for strain hardening in NC materials can lead to a strong localized deformation and plastic instabilities. While I) usually arises from processing, II) is caused by the poor dislocation storage capability in the small grains in NC structures and the readily available dislocation sinks in the form of grain boundaries.

In Figure 7 b) tensile results for the bcc TiZrNbHfTa alloy can be seen. The coarse-grained (CG) material already has a good yield strength, due to a strong solid solution strengthening. While the work hardening rate is quite limited, the tensile ductility is still high compared to other bcc HEAs [5,75]. HPT processing leads to a tensile strength of about 1.9 GPa and more impressively, the ductility is mostly retained, which as explained above is highly uncommon in NC materials. The reason for the good ductility of the NC TiZrNbHfTa alloy is not clear yet. Valiev et al. argued in case of NC Cu and Ti, where similar phenomena are occurring, that a change in the primary deformation mechanism might be the main cause. For instance, it could be caused by a shift from dislocation/twinning mediated plasticity to grain boundary based mechanisms [76,77].

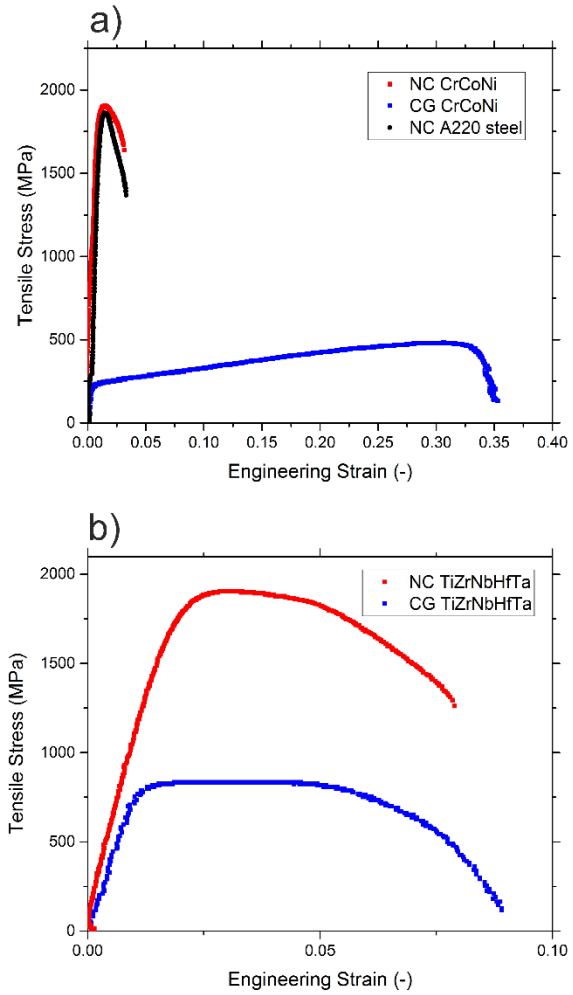

Figure 7: Representative stress-strain tensile curves of the CrCoNi alloy a) and the TiZrNbHfTa alloy b) for coarse-grained and NC microstructures. While the NC CrCoNi alloy suffers from the problem of low uniform elongation, commonly observed in NC metals, the TiZrNbHfTa alloy almost retains its ductility in the NC state.

Both materials show a ductile fracture with dimple formation after HPT processing, even the CrCoNi alloy that features a strongly reduced elongation to failure compared to the CG state, see Figure 8 a) and 8 b). In NC materials it is known that void formation is controlled by triple junctions and grain boundaries, which act as initiation points leading to shallow dimples in the range of the grain size or somewhat larger [78]. In none of the investigated NC samples a marked elongation of dimples was seen, which could point towards pronounced shear banding. In comparison, in coarse-grained structures the void initiation and formation occurs around inclusions and leads to deeper and more pronounced dimples.

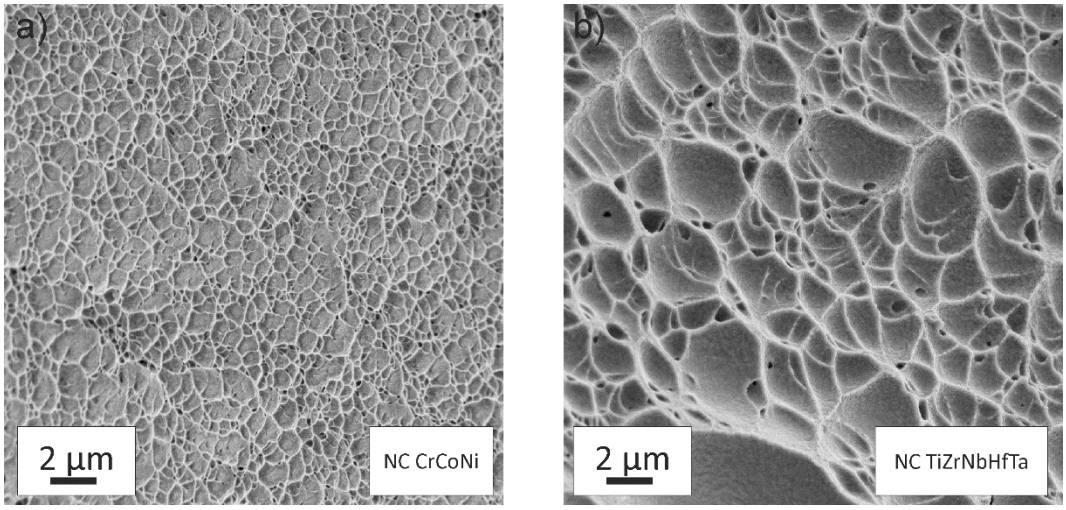

Figure 8: Fracture surfaces of the NC tensile samples of a) the CrCoNi and b) the TiZrNbHfTa alloy. Both materials feature shallow dimple fractures.

3.5 Annealing response of nanocrystalline high-entropy alloys

Upon isochronal (t = 1 h) annealing, the single-phase NC samples exhibit a peculiar hardness response, see Figure 9 a) and 9 b). For low annealing temperatures a hardness increase is observed in all of the samples, reaching a maximum hardness between 450 °C and 600 °C, depending on the alloy. The hardness increases are significant, reaching from 20 % to 45 % compared to the hardness of the HPT samples. The hardness increase has two major contributions: I) the "hardening by annealing" effect and II) phase decompositions and the precipitation of second phases. On the other hand, the subsequent drop in hardness for higher annealing temperatures can be explained by the onset of grain growth and by the fact that the single-phase character of the alloys is restored for very high annealing temperatures.

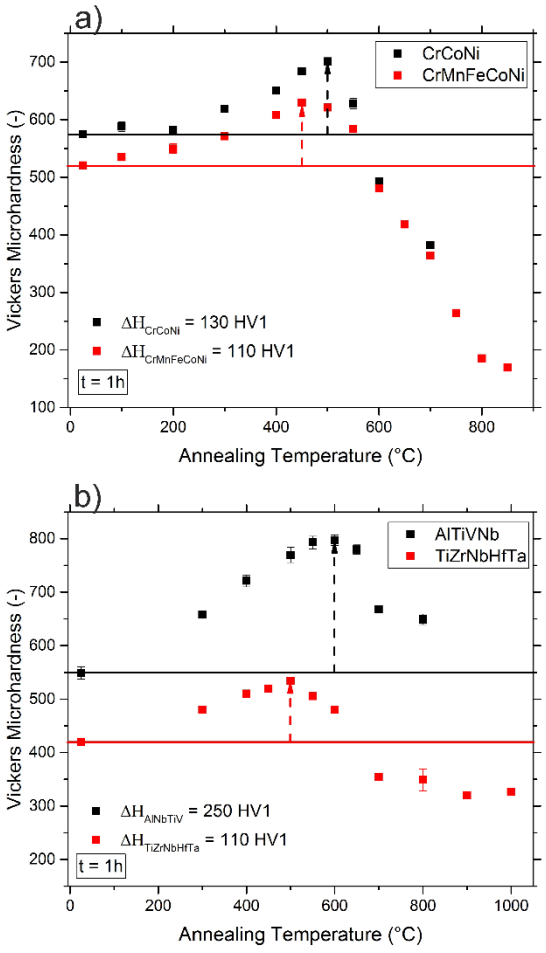

Figure 9: Evolution of the hardness versus temperature after post-HPT annealing treatments for 1 h. a) shows the hardness changes in the fcc HEAs, b) in the bcc HEAs. The straight line marks the hardness after HPT processing.

3.5.1 Hardening by annealing

Unlike in materials with conventional grain sizes, where heat treatments often lead to a reduced hardness and strength due to recovery and recrystallization, in NC materials below a certain threshold grain size [79], exactly the opposite can occur. This still rather controversially discussed topic was coined the "hardening by annealing" phenomenon by Huang et al. [80]. It was suggested that the phenomenon might originate from a rapid dislocation annihilation at the abundance of grain boundaries found in NC materials. This leaves the grain interior mostly starved of dislocation sources and therefore if a subsequent plastic deformation has to be realized, it is necessary that dislocations are emitted from grain boundaries. These are often in a relaxed state after annealing and dislocation emission might be more difficult, leading to the observed increase in the hardness [81–83]. Another popular explanation for this effect is the segregation of solutes to grain boundaries, which subsequently hampers the emission of dislocations due to solute-drag effects [84]. The common denominator of both explanations is that this phenomenon is caused by dislocation-grain boundary interactions. Due to the fact that, both, solute segregation and dislocation annihilation are occurring at the same time, it is already extremely difficult to discern the underlying mechanism. Additionally, in HEAs the situation is further complicated by the chemical complexity of the alloys and sometimes precipitation of second phases. However, one important clue, according to Renk et al. [81], are the rapid hardening kinetics. Substantial hardness increases are often reached after just a few minutes of annealing, which points towards a dislocation starvation/grain boundary relaxation driven process. The same quick hardening is also observed in the HEAs, see for instance the isothermal (T = 500 °C) annealing treatment of the TiZrNbHfTa alloy, where large changes in the hardness can be observed after just 5 min of annealing, Figure 10.

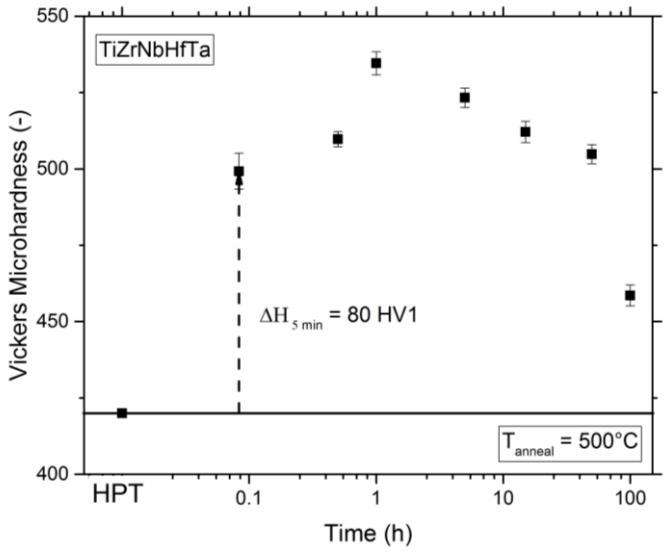

Figure 10: Hardness changes in the TiZrNbHfTa alloy after isothermal annealing at 500 °C. Even after short time anneals of just 5 minutes a substantial increase in the hardness occurs.

3.6 Microstructural changes and phase decompositions

One main goal of this thesis was to investigate the microstructural stability of various HEAs and the impact of a potential phase decomposition on the mechanical properties. Given the diverse nature of the investigated HEAs, each alloy will be discussed separately in the following. A brief summary of the observed phase decompositions and a comparison with recent literature data will be given at the end of this chapter.

3.6.1 CrCoNi

Like all alloys investigated in this thesis, the equiatomic CrCoNi HEA is commonly reported to be a single-phase alloy [3,51,85]. However, the presented data challenges these results. Even in the as-received state of the CrCoNi alloy an abundance of spherical, second phase precipitates, with a size of just a few nm, can be found via DF imaging, see Figure 11 a). In the corresponding electron diffraction image, inset of Figure 11 a), very faint rings related to this second phase can be seen, while the discrete reflexes belong to the coarse-grained fcc high-entropy phase. In Figure 11 b) synchrotron XRD data is seen, in which the presence of this second phase can be confirmed, both, in the NC state as well as for isochronal (t = 1 h) annealing states below 700 °C. Additionally, in Paper A corresponding electron diffraction data as well as DF images can be found for these microstructural states. In all of these annealing states the XRD data were insufficient to determine the crystal structure of this second phase. Only after long-term annealing at 500 °C, see Figure 11 c), the signal of the second phase particles was pronounced enough to determine that the phase has a hcp crystal structure with lattice constants very close to pure Co. A possible reason for the formation of this second phase was determined to be a favorable segregation of Co to stacking faults, which could lead to a reduction of the stacking fault energy, as was determined by Patriarca et al. for the CrMnFeCoNi HEA [86].

While the influence of these second phase particles on the mechanical properties could not be quantified so far, it seems that they are not very efficient obstacles for dislocations motion. Given the amount of precipitates in the coarse-grained, as-received material seen in Figure 11 a) and the fact that despite this the material only has a hardness of ~190 HV1, it seems sensible that precipitation hardening cannot be very significant in this alloy. For comparison, a A220 single-phase austenitic steel with a coarse-grained microstructure has a hardness of about 160 HV1 [68]. The slight difference in the hardness most likely originates from the higher solid solution strengthening in the CrCoNi alloy, due to the increased Cr content.

In conclusion, while the presence of the second phase certainly has some impact on the mechanical properties, the main reason for the observed hardness evolution as a function of the temperature seen in Figure 9, is mostly caused by an interplay of the hardening by annealing phenomenon and recrystallization/grain growth.

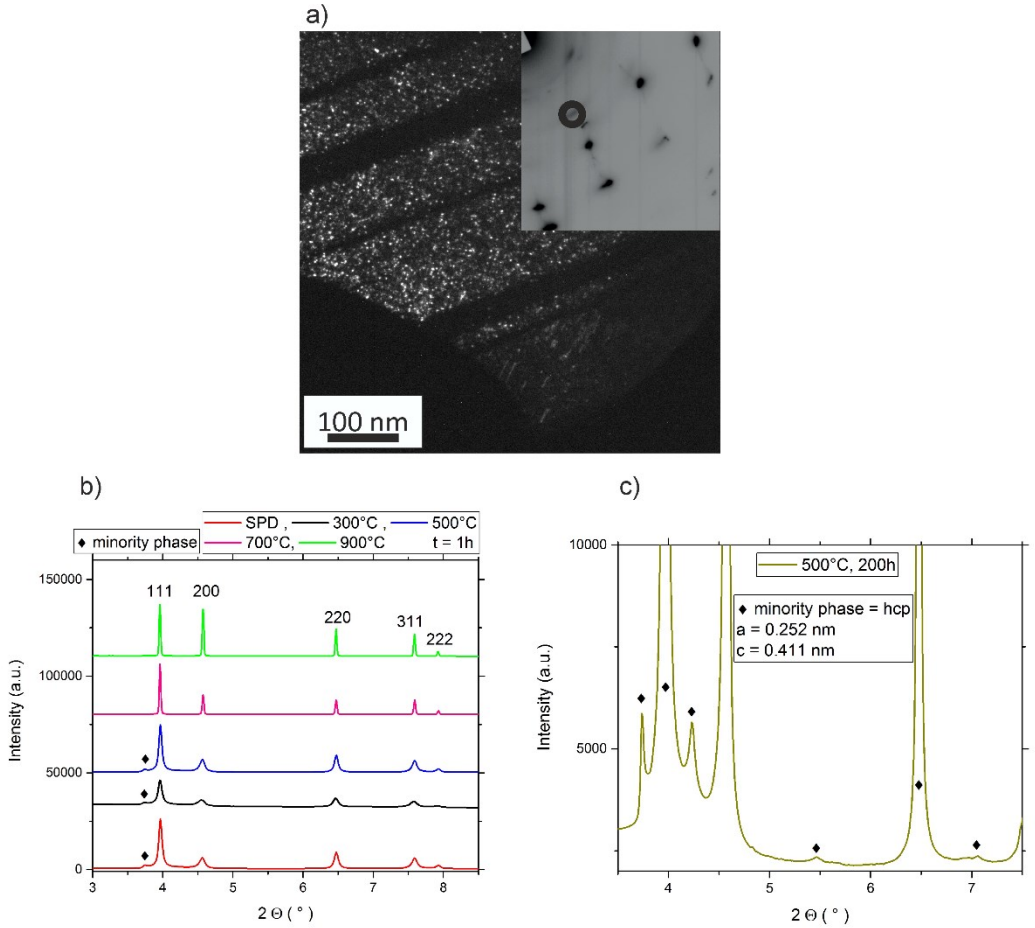

Figure 11: a) Dark-Field TEM image of the spherical precipitates occurring in the as-received state. The presence of the second phase precipitates can be observed in XRD data for annealing temperatures up to 500 °C, b). c), for long term (200 h) heat treatments at 500 °C the second phase peaks are sufficiently pronounced to determine that the second phase has a hcp crystal structure**.**

As mentioned in Chapter 3.4, a common problem in NC materials is the limited tensile ductility. Strategies to counteract this problem often revolve around restoring the low strain hardening rate, which would delay the onset of necking [87–89]. A straight-forward approach are heat treatments in order to achieve a slightly larger grain size. However, this usually results in a considerable loss of strength to gain ductility ("strength-ductility trade off"). A practical idea to achieve, both, high strength as well as ductility, would be to tailor a bimodal grain size distribution [87–89]. Annealing treatments at intermediate temperatures revealed that the CrCoNi alloy is prone to abnormal grain growth. Therefore bimodal grain size engineering to improve the tensile properties of the material can be attempted, see Figure 12 a) and b) for an example of such microstructures. In Figure 12 c) it can be seen that for one microstructural state the mechanical properties can be drastically improved, by more than doubling the elongation to failure (to about 10 %), while retaining ultra-high tensile strengths of approximately 1.5 GPa. However, it has to be noted that the work hardening rate of the material is still insufficient to allow for an extended uniform elongation. The increase in ductility originates from a much more pronounced non-uniform elongation after necking of the sample. This low work hardening rate could arise from an insufficient propensity for mechanical twinning, since even the coarse grains are comparatively small and twinning propensity is strongly dependent on grain size in low

SFE metals, such as the CrCoNi alloy [90]. Additionally, not all bimodal microstructures necessarily lead to improved tensile properties [91]. This is also observed in the presented work after annealing the NC samples at 550 °C for 10 minutes. There, large grains are already present, however, the samples still often fail in the elastic regime of the tensile test.

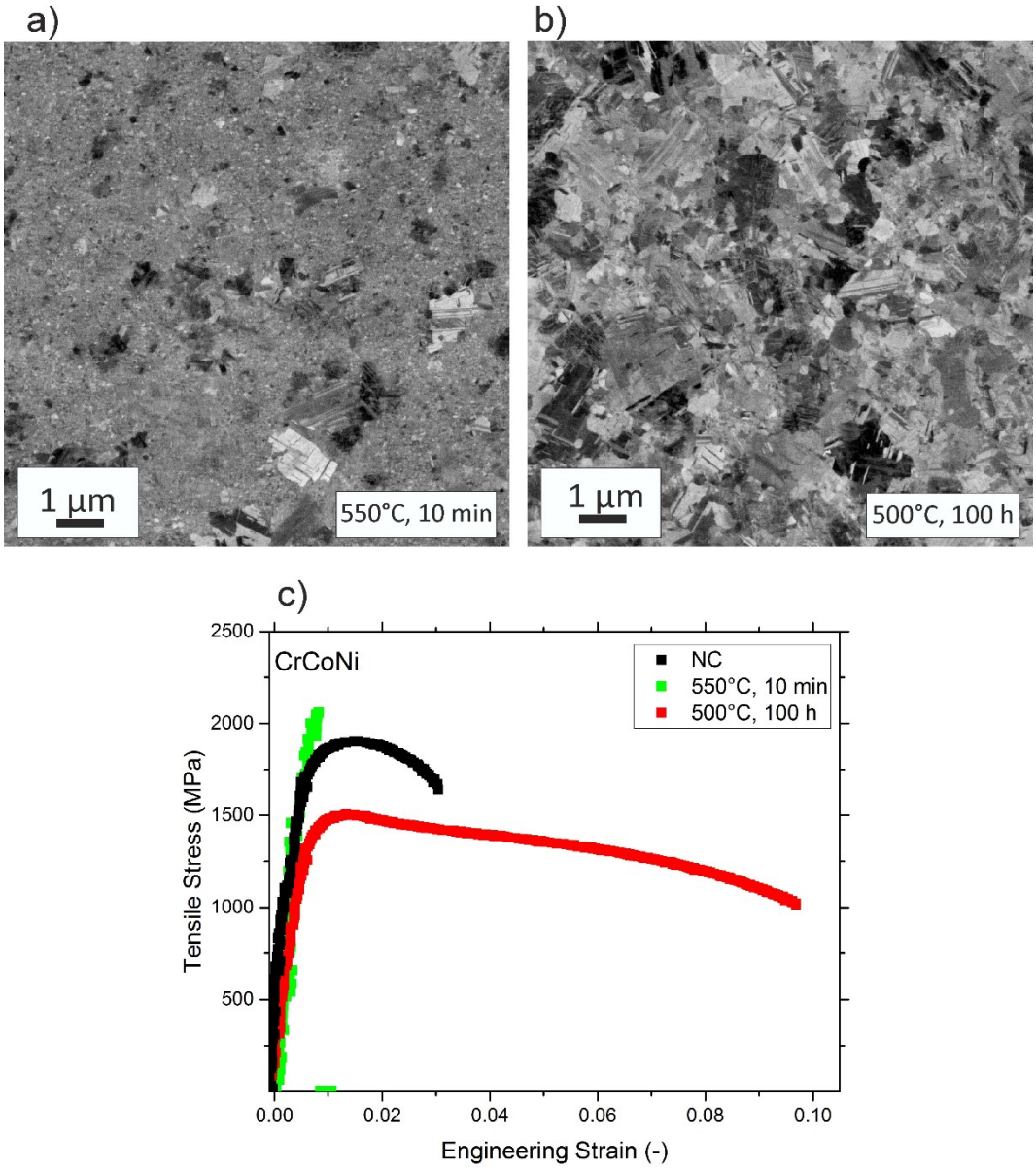

Figure 12: a) shows a BSE micrograph of a bimodal grain size structure in the CrCoNi alloy with a low fraction of coarse-grains, b) with a high fraction of coarse grains. c) depicts the corresponding mechanical properties, where the NC state has been added for comparison.

3.6.2 AlTiVNb

The mechanical response to the heat treatments of the AlTiVNb alloy was tracked via nanoindentation and by utilizing continuous stiffness measurements also the reduced modulus could be determined, Figure 13 a). The reason why the reduced modulus is measured and not the Young's modulus is due the lack of the information on the Poisson's Ratio, and its change with temperature for the AlTiVNb alloy. As can be seen in Figure 13 a) the reduced modulus of the NC state is decreased when compared to the as-cast material. In this case, the most likely explanation for the observed phenomenon is an anelastic behavior of the NC state in combination with a measurement method that evaluates the reduced modulus based on an unloading sequence [92]. Subsequent annealing changes the defect structure in the material, which could lead to a reduced anelastic behavior, which consequently results in a restoration of the modulus. For a heat treatment at 600 °C for 1 h the restoration of the reduced modulus is finished. Interestingly, while hardness slowly starts to decrease for temperatures higher than 700 °C, the reduced modulus increases further. This can be explained by the fact that at higher temperatures a precipitation of second phases occurs (Nb_2Al and also Ti_3Al).The hardness contribution of these intermetallic phases is counteracted by the onset of grain growth, see Figure 13 b) to 13 e). These second phases still can be observed when considering the reduced modulus of the alloy, since it is influenced by the presence of stiffer or more compliant second phases, but insensitive to grain growth. This has important implications, since it highlights the possibility of high-throughput analysis of possible phase decompositions in HEAs by tracking the elastic properties of the material, a strategy further explored in [93].

From XRD analysis it could be concluded that the new phases are Nb_2Al and Ti_3Al, Figure 14. While none of the data show a phase decomposition for temperatures below 700 °C it is sensible to conclude that at lower temperatures the decomposition is merely restricted by diffusion kinetics, rather than to assume that the high-entropy phase is stable at these temperatures. This is simply due to the fact that, when considering the Gibbs Free Energy which determines the thermodynamic stability, the influence of the entropy decreases with decreasing temperature. The consequence of this is that the high-entropy phase should be even less thermodynamic stable at lower temperatures. On the other hand, as can be seen in Figure 13 e), even subjecting the RHEA to high-temperature anneals of 1000 °C leads to a two phase microstructure. Since this was the maximum annealing temperature applied in this investigation it could not be exactly determined for which temperatures the bcc high-entropy phase can be considered thermodynamically stable. However, reports by Stepanov et al. show that if the material is subjected to homogenization treatments at 1200 °C the alloy remains in a single-phase state [55]. Therefore, it can be estimated that the minimum temperature for which the presence of the single high-entropy phase is the equilibrium state is between 1000 °C and 1200 °C.

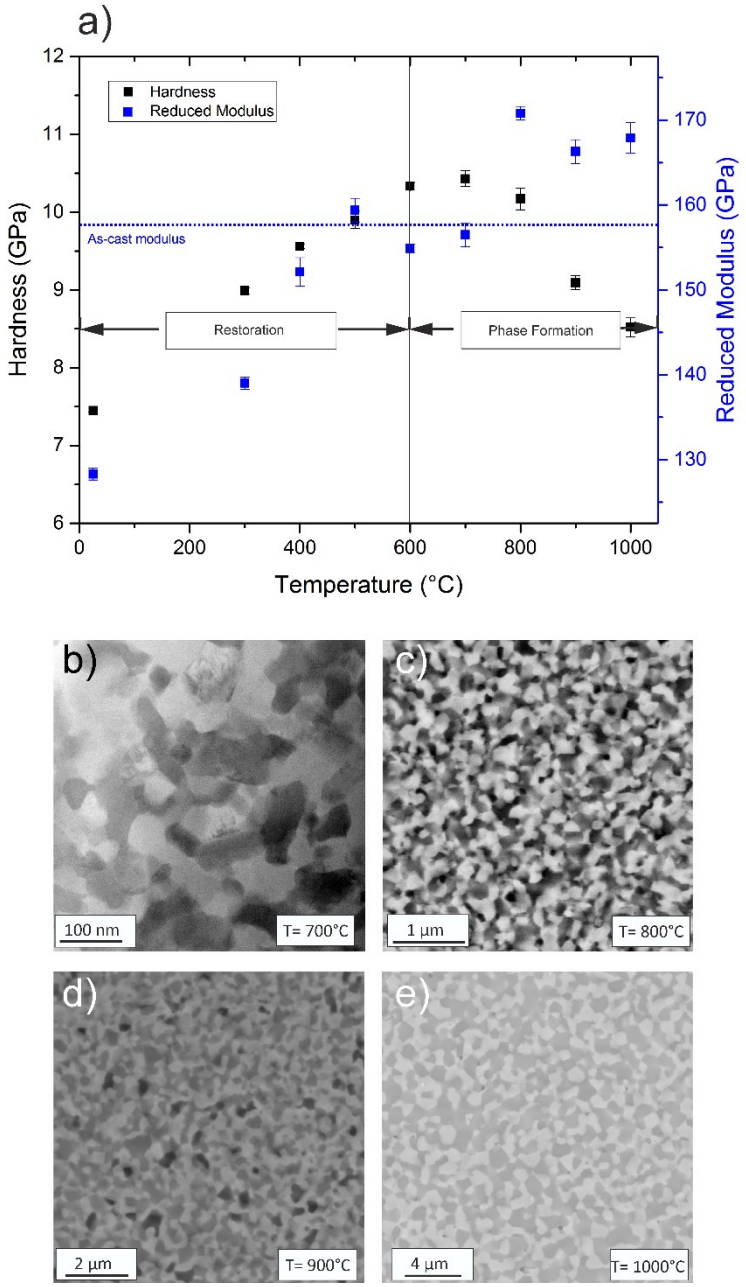

Figure 13: a) Reduced modulus and hardness evolution as a function of the annealing temperature. b) TEM and c)-e)BSE micrographs showing the microstructural changes after annealing. The brighter phase in the BSE images is Nb_2Al.

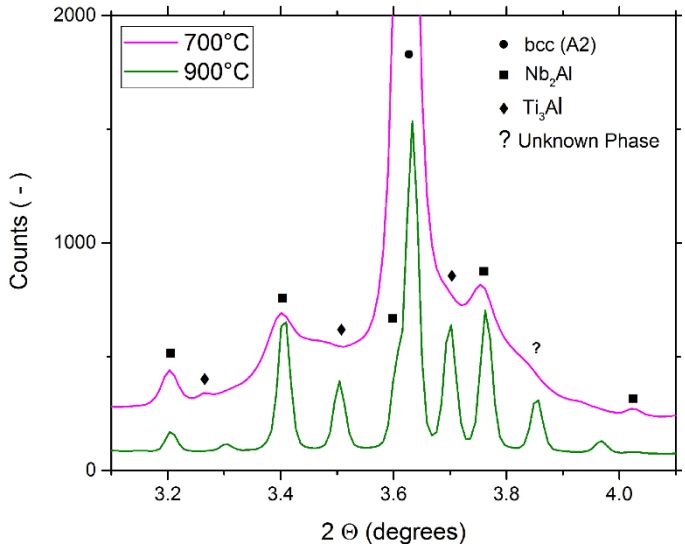

Figure 14: Detailed view of a small 2Θ-range of AlTiVNb samples after 1 h of annealing at 700 °C and 900 °C, showing the presence of a Nb_2Al-phase and Ti_3Al.

In summary, while for the AlTiVNb alloy some attractive properties, such as low density and high compressive strengths were reported, the alloy is also rather brittle at room temperature [55,56]. This problem gets more pronounced due to its microstructural instability and the resulting precipitation of intermetallic phases at temperatures below 1000 °C. However, the precipitation also leads to the hardness of the alloy exceeding 10 GPa, after a 600 °C heating treatment for 1 h, signifying a large strengthening potential. If this precipitation of second phases can be tailored to occur in a more favorable fashion, the AlTiVNb alloy might still qualify as a candidate alloy for high-temperature applications in the future. A good example of substantial changes in ductility due to microstructure engineering in RHEAs can be found in [94].

3.6.3 TiZrNbHfTa

The thermodynamic stability of this alloy was evaluated using a combined approach of the Calculation of Phase Diagrams method (CALPHAD, employing the TCHEA1 database [95]) and experimental microstructure investigations, see Figure 15. While Figure 15 a) shows the calculated phases, in Figure 15 b) to 15 e) a direct comparison with the microstructures obtained from the experiments can be found. According to CALPHAD calculations the equilibrium microstructure at low temperatures should be a ZrHf-rich hcp phase and a NbTa-rich bcc phase, which can be experimentally seen for long term anneals at 500 °C, Figure 15 b). For temperatures between 700 °C and 800 °C the microstructure should consist of a ZrHf-rich bcc phase in addition to the two previously mentioned phases. At this temperature the ZrHf-rich bcc phase can only be seen via synchrotron XRD measurements (not shown here, see Paper D). For higher temperatures the stable microstructure is the "high-entropy" bcc phase, enriched in Zr and Hf, and additionally present are NbTa-rich bcc precipitates. This can also be experimentally confirmed, see Figure 15 d). For very high annealing temperatures of 1100 °C the equilibrium microstructure should only consist of a single-phase, the bcc high-entropy phase, which is also true under experimental conditions, Figure 15 e). As can be seen, modelling and experimental results are in excellent agreement regarding which phases are forming and at what temperatures. Partial agreement also exists when comparing the chemistry of the phases, as can be seen in the appended Paper D. This is quite remarkable, since calculating phase diagrams of HEAs is more challenging than of traditional alloys, due to the limited data available in the center of the phase diagrams, which often leads to erroneous results. More about the challenges of CALPHAD modelling of HEAs can be found in [96].

The impact of annealing treatments on the mechanical properties can be seen in Figure 16. For a detailed discussion of the properties of the as-received and HPT processed material the reader is referred to chapter 3.4. Both 1 h annealing treatments at 500 °C and 800 °C lead to a deterioration of the mechanical properties. In case of the 500 °C, 1 h annealing treatment samples already fracture in the elastic regime of the tensile test without any prior macroscopic plastic deformation. After 800 °C, 1 h the specimens have both low strength and ductility. The low strength is caused by the phase decomposition and the rapid failure is caused by the immediate onset of necking after the elastic regime of the tensile test.

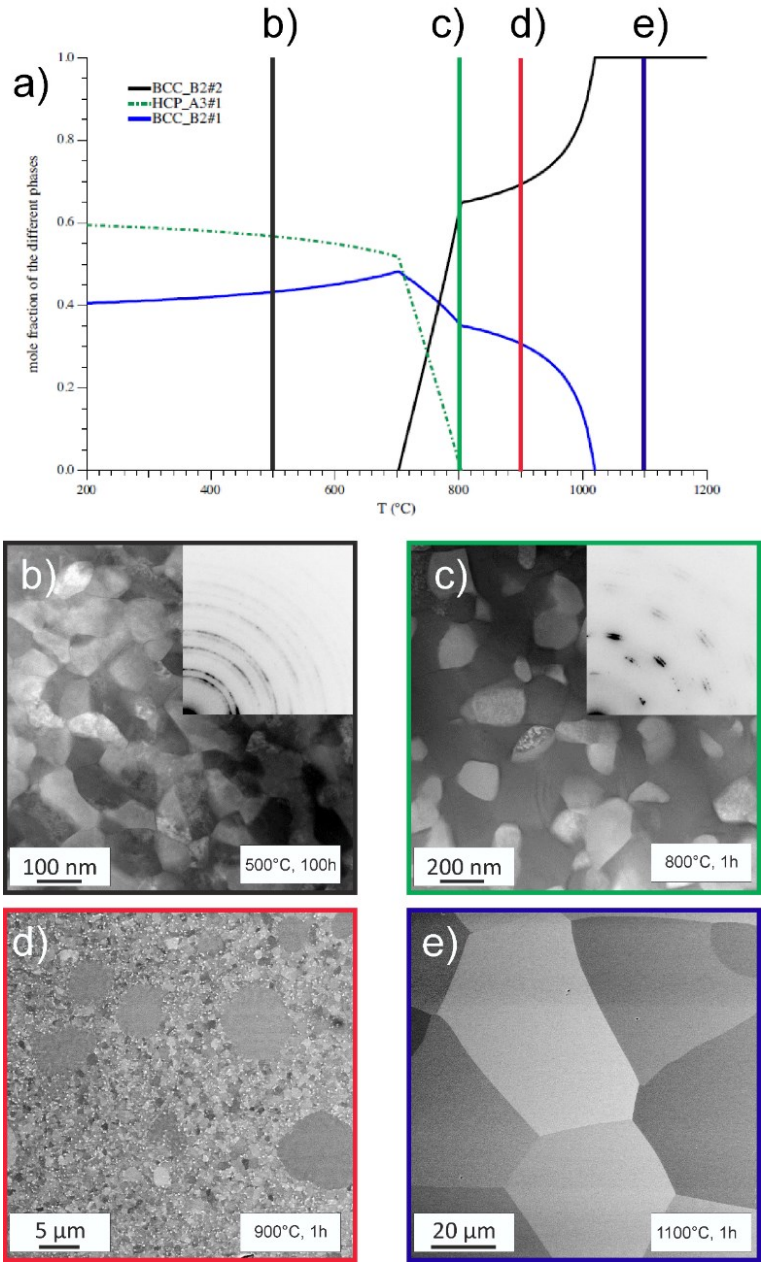

Figure 15: a) shows the predicted equilibrium phases as a function of temperature by employing the CALPHAD approach. For the annealing temperatures of b) 500 °C, c) 800 °C, d) 900 °C and e) 1100 °C experimental microstructure investigations were performed, which are in good agreement with the CALPHAD calculations.

Quantitative evidence for the softening due to the phase decomposition can be found in Paper D. It was obtained by reproducing the new phases and subjecting them to mechanical tests. It should be noted that this experimental result also has important implications for one of the HEA "core effects", namely the "Severe Lattice Distortion". One of the most striking, if only qualitative, arguments against the existence of severely strained crystal lattices is that such a lattice would also have a very high excess elastic strain energy, which would inherently threaten the thermodynamic stability of the alloy. Senkov et al. [32,57] estimated the contribution of solid solution strengthening in the

TiZrNbHfTa alloy, by assuming it was a pseudobinary solid solution of Ta-Nb-Ti and Zr-Hf. A majority of the solid solution strengthening due to atomic size misfit originates from misfits between those element-groups, while misfit within, for instance, Zr-Hf is negligible. The second contribution, elastic modulus misfit, is the largest around Ta atoms, while it is rather small for all other elements. What happens during the phase decomposition is that TiZrNbHfTa decomposes into Nb-Ta and Zr-Hf, thus into phases containing elements where the atomic size misfit is small and consequently the solid solution strengthening is quite weak. Thus it is sensible to assume that the phase decomposition is partially occurring due to excess elastic strain energy in the TiZrNbHfTa alloy, hence emphasizing the above made argument of the inherent instability of severely distorted lattices.

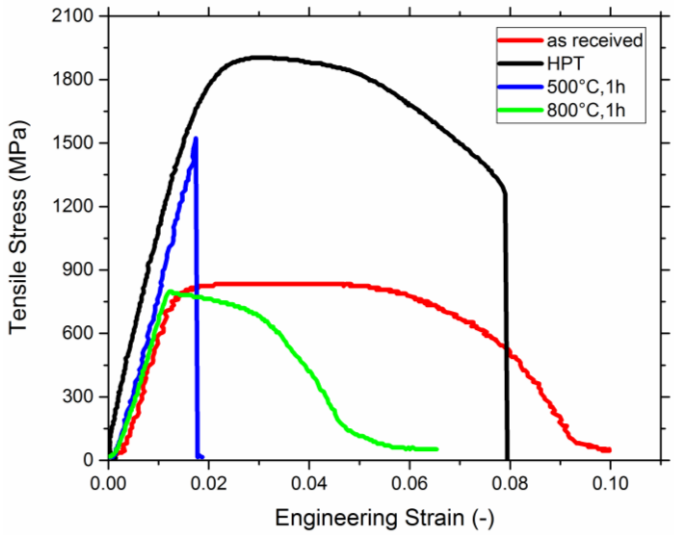

Figure 16: Tensile stress-strain curves of the coarse-grained and the HPT-processed TiZrNbHfTa alloys, as well as two annealing states.

In summary, the NC TiZrNbHfTa alloy should not be considered a stable, single-phase bcc alloy for temperatures below 1000 °C. The phase decomposition is heavily impacting the mechanical properties of the alloy and careful consideration needs to be given to the application temperature should this alloy be used as a structural material.

4.

Conclusion and impact of the results

The investigation of the NC CrMnFeCoNi alloy was the first study to show the thermodynamic instability of this alloy below temperatures of approximately 800 °C and its impact on the mechanical properties [18]. These findings were quickly verified by long-term anneals on coarser grained material. Pickering et al. first confirmed the precipitation of a Cr-rich phase after 700 °C anneals and clarified that it was a σ-phase [97]. This was followed up by another detailed investigation, performing heat treatments for up to 500 days for temperatures between 500 °C and 900 °C, again validating the initial findings and greatly improving our understanding of the forming phases by identifying the crystal structures of the low temperature phases at 500 °C ($L1_0$ for the NiMn-phase, B2 for the FeCo-phase and A2 for the Cr-phase [98]). Other publications substantiating the original results followed [99,100].

The idea of a phase stabilization by attaining a high configurational entropy was already challenged by other publications before, nonetheless, the work on the NC CrMnFeCoNi alloy has become a frequently cited example to demonstrate the insufficient contribution of configurational entropy to stabilize a single, disordered phase. This is largely due to the fact that the CrMnFeCoNi alloy was the first HEA ever reported and is considered a prototype HEA system.

Similarly, the publication on the CrCoNi alloy could demonstrate the presence of nanoscale, spherical precipitates embedded in the fcc HEA-matrix. While the possibility of the formation of such a phase was hinted at in one previous publication [101], the present work on the CrCoNi nonetheless is the first systematic investigation of this phase. However, it also has to be critically remarked that both the phase formation as well as its impact on the mechanical properties need to be studied further to establish a firm understanding. During the investigations of the CrCoNi alloy it was also discovered that it is unusually prone to abnormal grain growth and therefore it was attempted to improve the mechanical properties of the NC alloy by bimodal grain size engineering, a concept scarcely employed in the field of HEAs [102,103]. An excellent combination of a tensile strength of 1.5 GPa with an elongation to failure of 10 % was found for one annealing state. However, the comparatively low values of uniform elongation leave room for further improvement. For instance, by increasing the size of the coarse grains the propensity for mechanical twinning will also increase, which would lead to an increased work-hardening rate and further delay the onset of necking. However, this would likely also have the drawback that the yield strength of the material is decreased further.

As for the appended work on the AlTiVNb alloy, the formation of two intermetallic phases Nb_2Al and Ti_3Al was reported. While the formation of the σ-type Nb_2Al phase was observed previously once, the Ti_3Al has not been experimentally reported before, despite being predicted to be an equilibrium phase for all temperatures below approximately 750 °C by the CALPHAD method [56]. To the best of the author's knowledge, the presented work is also the only one to date to characterize the microstructural instability of the alloy at temperatures lower than 800 °C. As a critical remark, in recent publications it

is claimed that the HEA phase should have a B2 crystal structure, while in the presented and other previous works the crystal structure was identified to be A2 [104,105].

In case of the TiZrHfNbTa alloy, it already had been established that the alloy is thermodynamically unstable at 800 °C and the precipitation of a disordered NbTa bcc phase is occurring at this temperatures [58]. However, the work in Paper D is the first investigation to show the formation of a bcc ZrHf-phase (which at lower temperatures has a hcp crystal structure) both experimentally as well as with the CALPHAD approach. Additionally, the profound impact this phase decomposition has on the mechanical properties of the material was demonstrated. The formation of the hcp phase has also been acknowledged by publications following shortly after [106–108].

In conclusion, the work performed during this thesis on many supposedly single-phase HEAs has contributed to the understanding of the thermodynamic stability of HEA systems and the criticism of the concept of phase stabilization by increasing the configurational entropy. Additionally, the appended publications were among the first studies to investigate the HEAs in the NC grain size regime, not only with respect to the microstructural stability but also the mechanical properties.

5.

Outlook and future goals

The originally proposed special properties of HEAs, in the form of the four "core effects", are currently very controversially discussed and it appears such properties cannot be universally assumed for all HEAs. Nonetheless, the field of HEAs is prospering and it seems likely that the massive research activity will even increase further in the upcoming years. According to popular opinion the following goals are of paramount importance to the future of HEAs [12,23].

I) The most intriguing aspect of HEAs is the almost unlimited number of possible alloys. Therefore, one of the greatest challenges is to develop proper computational and experimental high-throughput techniques to quickly gauge the potential of a given alloy. Suggestions of how such procedures could look like were already given by Miracle et al. [10,11]. However, especially in regards to mechanical properties, proper high-throughput techniques are still required.

II) Prove the (in)validity of the core-effects. In general, the concept of the "core effects" seems questionable from currently available research. Convincing experimental results exist that show that a high configurational entropy is usually insufficient to stabilize a single, disordered phase. In regards to "Sluggish Diffusion" and "Severe Lattice Distortion" the available data so far suggest that these hypotheses are incorrect too. However, especially in consideration of the limited amount of existing HEA diffusion data, more experiments are still needed before these effects can be fully disregarded.

III) Find and implement promising candidate alloys into practical application. After almost 15 years of research, to the best of the author's knowledge, no HEA has yet been employed in practice. For the longevity of the field it would be crucial that application-driven research-efforts are made in order to prove their feasibility as structural materials. The most promising area for this seems in the high-temperature regime.

As a personal outlook, several topics still have to be expanded on in the future. Especially the possibility of bimodal grain size engineering in NC HEAs offers a unique opportunity to achieve materials with a supreme combination of strength and ductility. In Paper B the uniform elongation could not be restored, despite the presence of coarse-grains embedded in a matrix of NC grains. However, other alloys, such as the TiZrNbHfTa HEA, are also prone to abnormal grain growth, making it a good candidate for further grain size engineering, see Figure 17.

Also further investigations of the phase stability of the second phases occurring in the NC CrMnFeCoNi alloy and the possibility of re-dissolution of these phases is warranted. Recently, such a NC CrMnFeCoNi alloy was annealed to achieve a multi-phase microstructure and it was subsequently demonstrated that the second phases are prone to deformation-induced dissolution, leading to a pronounced strain-softening behavior during nanoindentation [109]. However, by means of nanoindentation only relatively low strains can be applied. It would be of great interest to see, if in such a multi-phase CrMnFeCoNi

alloy the original single-phase state could be restored by a complete mechanical re-dissolution of the second phases via HPT. First attempts can be seen in the hardness plot in Figure 18. The hardness significantly decreases after HPT deformation following the annealing treatments, which partially is caused by reversing the hardening by annealing effect, but to some degree likely also by a re-dissolution of second phase particles. If such a re-dissolution is possible, it would also be interesting if it could be applied in the TiZrHfNbTa alloy, given that the second phases and hardness differences between the occurring phases after annealing are vastly different in this alloy.

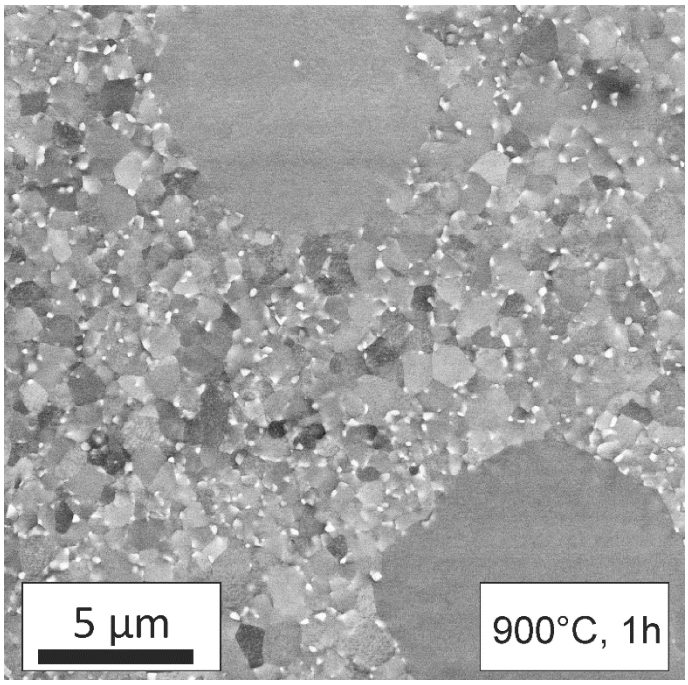

Figure 17: Example of bimodal grain size microstructures of the TiZrNbHfTa alloy. At this heat treatment temperature NbTa-rich precipitates are forming at the grain boundaries as well.

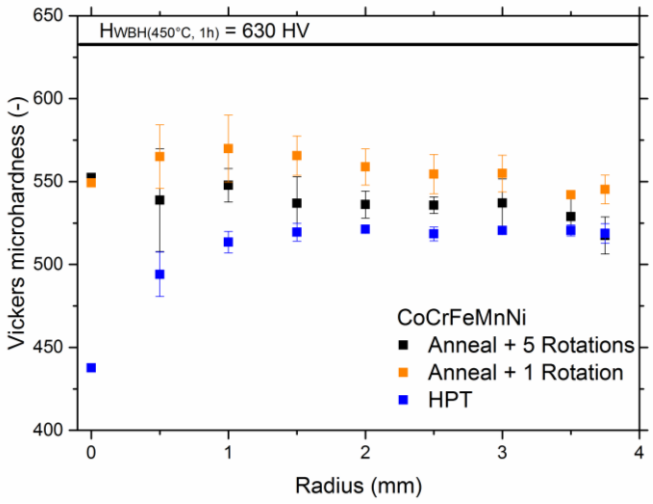

Figure 18: Hardness evolution of a heat-treated CrMnFeCoNi alloy that is subjected to HPT processing.

Furthermore, even for promising candidate alloys for structural applications, data on fracture toughness is almost completely absent in the literature. This is largely due to the fact that usually only very limited amounts of materials are produced. Nonetheless, fracture toughness is a critical property in many structural applications and gathering more data would greatly benefit the field of HEAs.

Lastly, in recent years an enhanced resistance to damage accumulation under irradiation was reported for HEAs [110–112]. Three general concepts exist to design irradiation resistant materials [113]: I) Obtaining high strength sinks, such as in nanostructured materials. II) Using materials, where point defects are immobile at the operational temperature, such as in SiC. III) Utilize materials with a high inherent resistance to irradiation, e.g. many bcc steels are superior to fcc steels. It is thought that HEAs might fall into the last category, but further experiments are needed to confirm this. Additionally, it would be of great interest to combine two of these approaches by nanostructuring of HEAs.

6. References

[1] B. Cantor, I.T.H. Chang, P. Knight, A.J.B. Vincent, Microstructural development in equiatomic multicomponent alloys, Mater. Sci. Eng. A. 375–377 (2004) 213–218. doi:10.1016/j.msea.2003.10.257.

[2] J.W. Yeh, S.K. Chen, S.J. Lin, J.Y. Gan, T.S. Chin, T.T. Shun, C.H. Tsau, S.Y. Chang, Nanostructured high-entropy alloys with multiple principal elements: Novel alloy design concepts and outcomes, Adv. Eng. Mater. 6 (2004) 299–303. doi:10.1002/adem.200300567.

[3] B. Gludovatz, A. Hohenwarter, K.V.S. Thurston, H. Bei, Z. Wu, E.P. George, R.O. Ritchie, Exceptional damage-tolerance of a medium-entropy alloy CrCoNi at cryogenic temperatures, Nat. Commun. 7 (2016) 10602 (1–8). doi:10.1038/ncomms10602.

[4] B. Gludovatz, A. Hohenwarter, D. Catoor, E.H. Chang, E.P. George, R.O. Ritchie, A fracture-resistant high-entropy alloy for cryogenic applications, Science 345 (2014) 1153–1158. doi:10.1126/science.1254581.

[5] O.N. Senkov, G.B. Wilks, J.M. Scott, D.B. Miracle, Mechanical properties of $Nb_{25}Mo_{25}Ta_{25}W_{25}$ and $V_{20}Nb_{20}Mo_{20}Ta_{20}W_{20}$ refractory high entropy alloys, Intermetallics 19 (2011) 698–706. doi:10.1016/j.intermet.2011.01.004.

[6] Y. Shi, B. Yang, P. Liaw, Corrosion-Resistant High-Entropy Alloys: A Review, Metals 7 (2017) 43 (1-18). doi:10.3390/met7020043.

[7] Y. Qiu, S. Thomas, M.A. Gibson, H.L. Fraser, N. Birbilis, Corrosion of high entropy alloys, Npj Mater. Degrad. 1 (2017) 1–15. doi:10.1038/s41529-017-0009-y.

[8] M.H. Chuang, M.H. Tsai, W.R. Wang, S.J. Lin, J.W. Yeh, Microstructure and wear behavior of AlxCo1.5CrFeNi1.5Tiy high-entropy alloys, Acta Mater. 59 (2011) 6308–6317. doi:10.1016/j.actamat.2011.06.041.

[9] B. Gorr, M. Azim, H.J. Christ, T. Mueller, D. Schliephake, M. Heilmaier, Phase equilibria, microstructure, and high temperature oxidation resistance of novel refractory high-entropy alloys, J. Alloys Compd. 624 (2015) 270–278. doi:10.1016/j.jallcom.2014.11.012.

[10] D.B. Miracle, J.D. Miller, O.N. Senkov, C. Woodward, M.D. Uchic, J. Tiley, Exploration and development of high entropy alloys for structural applications, Entropy 16 (2014) 494–525. doi:10.3390/e16010494.

[11] D.B. Miracle, High entropy alloys and their development as structural materials, Mater.Sci.Technol. 31 (2015) 1142–1147.doi:10.1179/1743284714Y.0000000749.

[12] D.B. Miracle, O.N. Senkov, A critical review of high entropy alloys and related concepts, Acta Mater. 122 (2017) 448–511. doi:10.1016/j.actamat.2016.08.081.

[13] www.scopus.com, Last Accessed October 2018.

[14] Y. Zhang, T.T. Zuo, Z. Tang, M.C. Gao, K.A. Dahmen, P.K. Liaw, Z.P. Lu,

Microstructures and properties of high-entropy alloys, Prog. Mater. Sci. 61 (2014) 1–93. doi:10.1016/j.pmatsci.2013.10.001.

[15] R. Kozak, A. Sologubenko, W. Steurer, Single-phase high-entropy alloys - An overview, Zeitschrift Fur Krist. 230 (2015) 55–68. doi:10.1515/zkri-2014-1739.

[16] F. Otto, Y. Yang, H. Bei, E.P. George, Relative effects of enthalpy and entropy on the phase stability of equiatomic high-entropy alloys, Acta Mater. 61 (2013) 2628–2638. doi:10.1016/j.actamat.2013.01.042.

[17] M. Laurent-Brocq, A. Akhatova, L. Perrière, S. Chebini, X. Sauvage, E. Leroy, Y. Champion, Insights into the phase diagram of the CrMnFeCoNi high entropy alloy, Acta Mater. 88 (2015) 355–365. doi:10.1016/j.actamat.2015.01.068.

[18] B. Schuh, F. Mendez-Martin, B. Völker, E.P. George, H. Clemens, R. Pippan, A. Hohenwarter, Mechanical properties, microstructure and thermal stability of a nanocrystalline CoCrFeMnNi high-entropy alloy after severe plastic deformation, Acta Mater. 96 (2015) 258–268. doi:10.1016/j.actamat.2015.06.025.

[19] G. Dirras, J. Gubicza, A. Heczel, L. Lilensten, J.-P. Couzinié, L. Perrière, I. Guillot, A. Hocini, Microstructural investigation of plastically deformed $Ti_{20}Zr_{20}Hf_{20}Nb_{20}Ta_{20}$ high entropy alloy by X-ray diffraction and transmission electron microscopy, Mater. Charact. 108 (2015) 1–7. doi:10.1016/j.matchar.2015.08.007.

[20] J.P. Couzinié, G. Dirras, L. Perrière, T. Chauveau, E. Leroy, Y. Champion, I. Guillot, Microstructure of a near-equimolar refractory high-entropy alloy, Mater. Lett. 126 (2014) 285–287. doi:10.1016/j.matlet.2014.04.062.

[21] O.N. Senkov, D.B. Miracle, K.J. Chaput, J.-P. Couzinie, Development and exploration of refractory high entropy alloys—A review, J. Mater. Res. (2018) 1–37. doi:10.1557/jmr.2018.153.

[22] J.W. Yeh, Alloy design strategies and future trends in high-entropy alloys, JOM 65 (2013) 1759–1771. doi:10.1007/s11837-013-0761-6.

[23] E.J. Pickering, N.G. Jones, High-entropy alloys: a critical assessment of their founding principles and future prospects, Int. Mater. Rev. 61 (2016) 184–202. doi:10.1080/09506608.2016.1180020.

[24] J.W. Yeh, S.K. Chen, J.Y. Gan, S.J. Lin, T.S. Chin, T.T. Shun, C.H. Tsau, S.Y. Chang, Formation of simple crystal structures in Cu-Co-Ni-Cr-Al-Fe-Ti-V alloys with multiprincipal metallic elements, Metall. Mater. Trans. A. 35 A (2004) 2533–2536. doi:10.1007/s11661-006-0234-4.

[25] J.W. Yeh, Recent progress in high-entropy alloys, Ann. Chim. Sci. Des Mater. 31 (2006) 633–648. doi:10.3166/acsm.31.633-648.

[26] J.W. Yeh, Physical Metallurgy of High-Entropy Alloys, JOM 67 (2015) 2254–2261. doi:10.1007/s11837-015-1583-5.

[27] M.H. Tsai, J.W. Yeh, High-Entropy Alloys: A Critical Review, Mater. Res. Lett. 2 (2014) 107–123. doi:10.1080/21663831.2014.912690.

[28] B.S. Murty, J.W. Yeh, S. Ranganathan, High-entropy Alloys, Butterworth-Heinemann, 2014. doi:https://doi.org/10.1016/C2013-0-14235-3.

[29] A. Takeuchi, A. Inoue, Mixing enthalpy of liquid phase calculated by miedema's scheme and approximated with sub-regular solution model for assessing forming ability of amorphous and glassy alloys, Intermetallics 18 (2010) 1779–1789. doi:10.1016/j.intermet.2010.06.003.

[30] D. Ma, B. Grabowski, F. Körmann, J. Neugebauer, D. Raabe, Ab initio thermodynamics of the CoCrFeMnNi high entropy alloy: Importance of entropy contributions beyond the configurational one, Acta Mater. 100 (2015) 90–97. doi:10.1016/j.actamat.2015.08.050.

[31] O.N. Senkov, J.D. Miller, D.B. Miracle, C. Woodward, Accelerated exploration of multi-principal element alloys for structural applications, Calphad Comput. Coupling Phase Diagrams Thermochem. 50 (2015) 32–48. doi:10.1016/j.calphad.2015.04.009.

[32] R.L. Fleischer, Substitutional solution hardening, Acta Metall. 11 (1963) 203–209. doi:10.1016/0001-6160(63)90213-X.

[33] K. Jin, H. Bei, Single-Phase Concentrated Solid-Solution Alloys: Bridging Intrinsic Transport Properties and Irradiation Resistance, Front. Mater. 5 (2018) 1–11. doi:10.3389/fmats.2018.00026.

[34] M. Fèvre, C. Varvenne, A. Finel, Y. Le Bouar, Influence of atomic size mismatch on binary alloy phase diagrams, Philos. Mag. 93 (2013) 1563–1581. doi:10.1080/14786435.2012.748223.

[35] J.W. Yeh, S.K. Chen, J.Y. Gan, S.J. Lin, T.S. Chin, T.T. Shun, C.H. Tsau, S.Y. Chang, J.Y. Gan, S.K. Chen, T.T. Shun, C.H. Tsau, S.Y. Chou, Formation of simple crystal structures in Cu-Co-Ni-Cr-Al-Fe-Ti-V alloys with multiprincipal metallic elements, Metall. Mater. Trans. A. 35 A (2004) 2533–2536. doi:10.1007/s11661-006-0234-4.

[36] F. Otto, A. Dlouhý, C. Somsen, H. Bei, G. Eggeler, E.P. George, The influences of temperature and microstructure on the tensile properties of a CoCrFeMnNi high-entropy alloy, Acta Mater. 61 (2013) 5743–5755. doi:10.1016/j.actamat.2013.06.018.

[37] B. Gludovatz, E.P. George, R.O. Ritchie, Processing, Microstructure and Mechanical Properties of the CrMnFeCoNi High-Entropy Alloy, JOM 67 (2015) 2262–2270. doi:10.1007/s11837-015-1589-z.

[38] B.C. De Cooman, Y. Estrin, S.K. Kim, Twinning-induced plasticity (TWIP) steels, Acta Mater. 142 (2018) 283–362. doi:10.1016/j.actamat.2017.06.046.

[39] O. Grässel, L. Krüger, G. Frommeyer, L.W. Meyer, High strength Fe-Mn-(Al, Si) TRIP/TWIP steels development - properties - application, Int. J. Plast. 16 (2000) 1391–1409. doi:10.1016/S0749-6419(00)00015-2.

[40] C. Lee, Master Thesis, National Tsing Hua University, 2013.

[41] L.R. Owen, E.J. Pickering, H.Y. Playford, H.J. Stone, M.G. Tucker, N.G. Jones, An assessment of the lattice strain in the CrMnFeCoNi high-entropy alloy, Acta Mater. 122 (2017) 11–18. doi:10.1016/j.actamat.2016.09.032.

[42] H.S. Oh, D. Ma, G.P. Leyson, B. Grabowski, E.S. Park, F. Kormann, D. Raabe, Lattice distortions in the FeCoNiCrMn high entropy alloy studied by theory and experiment, Entropy 18 (2016) 1–9. doi:10.3390/e18090321.

[43] I. Toda-Caraballo, J.S. Wróbel, S.L. Dudarev, D. Nguyen-Manh, P.E.J. Rivera-Díaz-Del-Castillo, Interatomic spacing distribution in multicomponent alloys, Acta Mater. 97 (2015) 156–169. doi:10.1016/j.actamat.2015.07.010.

[44] C.J. Tong, Y.L. Chen, J.W. Yeh, S.J. Lin, S.-K. Chen, T.T. Shun, C.H. Tsau, S.Y. Chang, Microstructure characterization of AlxCoCrCuFeNi high-entropy alloy system with multiprincipal elements, Metall. Mater. Trans. A. 36 (2005) 881–893. doi:10.1007/s11661-005-0283-0.

[45] K.Y. Tsai, M.H. Tsai, J.W. Yeh, Sluggish diffusion in Co-Cr-Fe-Mn-Ni high-entropy alloys, Acta Mater. 61 (2013) 4887–4897. doi:10.1016/j.actamat.2013.04.058.

[46] M. Vaidya, S. Trubel, B.S. Murty, G. Wilde, S. V. Divinski, Ni tracer diffusion in CoCrFeNi and CoCrFeMnNi high entropy alloys, J. Alloys Compd. 688 (2016) 994–1001. doi:10.1016/j.jallcom.2016.07.239.

[47] M. Vaidya, K.G. Pradeep, B.S. Murty, G. Wilde, S. V. Divinski, Radioactive isotopes reveal a non sluggish kinetics of grain boundary diffusion in high entropy alloys, Sci. Rep. 7 (2017) 12293 (1–11). doi:10.1038/s41598-017-12551-9.

[48] D. Gaertner, J. Kottke, G. Wilde, S. V. Divinski, Y. Chumlyakov, Tracer diffusion in single crystalline CoCrFeNi and CoCrFeMnNi high entropy alloys, J. Mater. Res. (2018) 1–8. doi:10.1557/jmr.2018.162.

[49] S. Ranganathan, Alloyed pleasures: Multimetallic cocktails, Curr. Sci. 85 (2003) 1404–1406.

[50] A.W. Bronkhorst, The cocktail-party problem revisited: early processing and selection of multi-talker speech, Attention, Perception, Psychophys. 77 (2015) 1465–1487. doi:10.3758/s13414-015-0882-9.

[51] G. Laplanche, A. Kostka, C. Reinhart, J. Hunfeld, G. Eggeler, E.P. George, Reasons for the superior mechanical properties of medium-entropy CrCoNi compared to high-entropy CrMnFeCoNi, Acta Mater. 128 (2017) 292–303. doi:10.1016/j.actamat.2017.02.036.

[52] Z. Zhang, H. Sheng, Z. Wang, B. Gludovatz, Z. Zhang, E.P. George, Q. Yu, S.X. Mao, R.O. Ritchie, Dislocation mechanisms and 3D twin architectures generate exceptional strength-ductility-toughness combination in CrCoNi medium-entropy alloy, Nat. Commun. 8 (2017) 14390 (1–8). doi:10.1038/ncomms14390.

[53] O.N. Senkov, G.B. Wilks, D.B. Miracle, C.P. Chuang, P.K. Liaw, Refractory high-entropy alloys, Intermetallics 18 (2010) 1758–1765. doi:10.1016/j.intermet.2010.05.014.

[54] O.N. Senkov, D. Isheim, D.N. Seidman, A.L. Pilchak, Development of a refractory high entropy superalloy, Entropy 18 (2016) 1–13. doi:10.3390/e18030102.

[55] N.D. Stepanov, D.G. Shaysultanov, G.A. Salishchev, M.A. Tikhonovsky, Structure and mechanical properties of a light-weight AlNbTiV high entropy alloy, Mater. Lett. 142 (2015) 153–155. doi:10.1016/j.matlet.2014.11.162.

[56] N.D. Stepanov, N.Y. Yurchenko, D.V. Skibin, M.A. Tikhonovsky, G.A. Salishchev, Structure and mechanical properties of the AlCrxNbTiV (x = 0, 0.5, 1, 1.5) high entropy alloys, J. Alloys Compd. 652 (2015) 266–280. doi:10.1016/j.jallcom.2015.08.224.

[57] O.N. Senkov, J.M. Scott, S. V. Senkova, D.B. Miracle, C.F. Woodward, Microstructure and room temperature properties of a high-entropy TaNbHfZrTi alloy, J. Alloys Compd. 509 (2011) 6043–6048. doi:10.1016/j.jallcom.2011.02.171.

[58] O.N. Senkov, J.M. Scott, S. V. Senkova, F. Meisenkothen, D.B. Miracle, C.F. Woodward, Microstructure and elevated temperature properties of a refractory TaNbHfZrTi alloy, J. Mater. Sci. 47 (2012) 4062–4074. doi:10.1007/s10853-012-6260-2.

[59] J.P. Couzinié, L. Lilensten, Y. Champion, G. Dirras, L. Perrière, I. Guillot, On the room temperature deformation mechanisms of a TiZrHfNbTa refractory high-entropy alloy, Mater. Sci. Eng. A. 645 (2015) 255–263. doi:10.1016/j.msea.2015.08.024.

[60] G. Dirras, L. Lilensten, P. Djemia, M. Laurent-Brocq, D. Tingaud, J.P. Couzinié, L. Perrière, T. Chauveau, I. Guillot, Elastic and plastic properties of as-cast equimolar TiHfZrTaNb high-entropy alloy, Mater. Sci. Eng. A. 654 (2016) 30–38. doi:10.1016/j.msea.2015.12.017.

[61] G. Dirras, H. Couque, L. Lilensten, A. Heczel, D. Tingaud, J.P. Couzinié, L. Perrière, J. Gubicza, I. Guillot, Mechanical behavior and microstructure of $Ti_{20}Hf_{20}Zr_{20}Ta_{20}Nb_{20}$ high-entropy alloy loaded under quasi-static and dynamic compression conditions, Mater. Charact. 111 (2016) 106–113. doi:10.1016/j.matchar.2015.11.018.

[62] P. Grammatikopoulos, S. Steinhauer, J. Vernieres, V. Singh, M. Sowwan, Nanoparticle design by gas-phase synthesis, Adv. Phys. X. 1 (2016) 81–100. doi:10.1080/23746149.2016.1142829.

[63] M. Furukawa, Z. Horita, M. Nemoto, T.G. Langdon, Review: Processing of metals by equal-channel angular pressing, J. Mater. Sci. 36 (2001) 2835–2843. doi:10.1023/a:1017932417043.

[64] N. Tsuji, Y. Saito, S.H. Lee, Y. Minamino, ARB (accumulative roll-bonding) and other new techniques to produce bulk ultrafine grained materials, Adv. Eng. Mater. 5 (2003) 338–344. doi:10.1002/adem.200310077.

[65] A.P. Zhilyaev, T.G. Langdon, Using high-pressure torsion for metal processing: Fundamentals and applications, Prog. Mater. Sci. 53 (2008) 893–979.

doi:10.1016/j.pmatsci.2008.03.002.

[66] R. Pippan, S. Scheriau, A. Hohenwarter, M. Hafok, Advantages and Limitations of HPT: A Review, Mater. Sci. Forum. 584–586 (2008) 16–21. doi:10.4028/www.scientific.net/MSF.584-586.16.

[67] R. Valiev, Nanostructuring of metals by severe plastic deformation for advanced properties, Nat. Mater. 3 (2004) 511–516. doi:10.1038/nmat1180.

[68] S. Scheriau, Z. Zhang, S. Kleber, R. Pippan, Deformation mechanisms of a modified 316L austenitic steel subjected to high pressure torsion, Mater. Sci. Eng. A. 528 (2011) 2776–2786. doi:10.1016/j.msea.2010.12.023.

[69] O.N. Senkov, S.L. Semiatin, Microstructure and properties of a refractory high-entropy alloy after cold working, J. Alloys Compd. 649 (2015) 1110–1123. doi:10.1016/j.jallcom.2015.07.209.

[70] R. Pippan, S. Scheriau, A. Taylor, M. Hafok, A. Hohenwarter, A. Bachmaier, Saturation of fragmentation during severe plastic deformation, Annu. Rev. Mater. Res. 40 (2010) 319–343. doi:10.1146/annurev-matsci-070909-104445.

[71] A. Bachmaier, M. Hafok, R. Pippan, Rate Independent and Rate Dependent Structural Evolution during Severe Plastic Deformation, Mater. Trans. 51 (2010) 8–13. doi:10.2320/matertrans.MB200912.

[72] M.J. Zehetbauer, H.P. Stüwe, A. Vorhauer, E. Schafler, J. Kohout, The role of hydrostatic pressure in severe plastic deformation, Adv. Eng. Mater. 5 (2003) 330–337. doi:10.1002/adem.200310090.

[73] R.Z. Valiev, R.K. Islamgaliev, I. V. Alexandrov, Bulk nanostructured materials from severe plastic deformation, Prog. Mater. Sci 45 (2000). doi:10.1016/S0079-6425(99)00007-9.

[74] E. Ma, Instabilities and ductility of nanocrystalline and ultrafine-grained metals, Scr. Mater. 49 (2003) 663–668. doi:10.1016/S1359-6462(03)00396-8.

[75] O.N. Senkov, C. Woodward, D.B. Miracle, Microstructure and Properties of Aluminum-Containing Refractory High-Entropy Alloys, JOM 66 (2014) 2030–2042. doi:10.1007/s11837-014-1066-0.

[76] R.Z. Valiev, Y. Zhu, Recent Findings in Superior Strength and Ductility of Ultrafine-Grained Materials, Trans. Mat. Res. Soc. Japan. 40 (2015) 309–318.

[77] R.Z. Valiev, I. V Alexandrov, Y.T. Zhu, T.C. Lowe, Paradox of strength and ductility in metals processed by severe plastic deformation, J. Mater. Res. 17 (2002) 5–8. doi:10.1557/JMR.2002.0002.

[78] A. Hohenwarter, R. Pippan, Fracture and fracture toughness of nanopolycrystalline metals produced by severe plastic deformation, Philos. Trans. R. Soc. A. 373 (2015) 20140366 (1–17). doi:10.1098/rsta.2014.0366.

[79] O. Renk, A. Hohenwarter, B. Schuh, J. Li, R. Pippan, Hardening by annealing: Insights from different alloys, IOP Conf. Ser. Mater. Sci. Eng. 89 (2015) 012043

(1–7). doi:10.1088/1757-899X/89/1/012043.

[80] X. Huang, N. Hansen, N. Tsuji, Hardening by Annealing and Softening by Deformation in Nanostructured Metals, Science. 312 (2006) 249–251. doi:10.1126/science.1124268.

[81] O. Renk, A. Hohenwarter, K. Eder, K.S. Kormout, J.M. Cairney, R. Pippan, Increasing the strength of nanocrystalline steels by annealing: Is segregation necessary?, Scr. Mater. 95 (2015) 27–30. doi:10.1016/j.scriptamat.2014.09.023.

[82] X. Tong, H. Zhang, D.Y. Li, Effect of Annealing Treatment on Mechanical Properties of Nanocrystalline α-iron: An Atomistic Study, Sci. Rep. 5 (2015) 8459 (1–7). doi:10.1038/srep08459.

[83] E. Ma, T.D. Shen, X.L. Wu, Nanostructured metals: less is more., Nat. Mater. 5 (2006) 515–516. doi:10.1038/nmat1671.

[84] R.Z. Valiev, N.A. Enikeev, M.Y. Murashkin, V.U. Kazykhanov, X. Sauvage, On the origin of the extremely high strength of ultrafine-grained Al alloys produced by severe plastic deformation, Scr. Mater. 63 (2010) 949–952. doi:10.1016/j.scriptamat.2010.07.014.

[85] Z. Wu, H. Bei, F. Otto, G.M. Pharr, E.P. George, Recovery, recrystallization, grain growth and phase stability of a family of FCC-structured multi-component equiatomic solid solution alloys, Intermetallics 46 (2014) 131–140. doi:10.1016/j.intermet.2013.10.024.

[86] L. Patriarca, A. Ojha, H. Sehitoglu, Y.I. Chumlyakov, Slip nucleation in single crystal FeNiCoCrMn high entropy alloy, Scr. Mater. 112 (2016) 54–57. doi:10.1016/j.scriptamat.2015.09.009.

[87] E. Ma, Eight routes to improve the tensile ductility of bulk nanostructured metals and alloys, JOM 58 (2006) 49–53. doi:10.1007/s11837-006-0215-5.

[88] Y. Zhao, Y. Zhu, E.J. Lavernia, Strategies for improving tensile ductility of bulk nanostructured materials, Adv. Eng. Mater. 12 (2010) 769–778. doi:10.1002/adem.200900335.

[89] Y.M. Wang, E. Ma, Three strategies to achieve uniform tensile deformation in a nanostructured metal, Acta Mater. 52 (2004) 1699–1709. doi:10.1016/j.actamat.2003.12.022.

[90] E. El-Danaf, S.R. Kalidindi, R. Doherty, Influence of grain size and stacking fault energy on deformation twinning in fcc metals., Metall. Mater. Trans. A. 30 (1999) 1223–1233.

[91] O. Renk, A. Hohenwarter, R. Pippan, Cyclic deformation behavior of a 316L austenitic stainless steel processed by high pressure torsion, Adv. Eng. Mater. 14 (2012) 948–954. doi:10.1002/adem.201200015.

[92] F. Mompiou, D. Caillard, M. Legros, H. Mughrabi, In situ TEM observations of reverse dislocation motion upon unloading in tensile-deformed UFG aluminium, Acta Mater. 60 (2012) 3402–3414. doi:10.1016/j.actamat.2012.02.049.

[93] V. Maier-Kiener, B. Schuh, E.P. George, H. Clemens, A. Hohenwarter, Nanoindentation testing as a powerful screening tool for assessing phase stability of nanocrystalline high-entropy alloys, Mater. Des. 115 (2016) 479–485. doi:10.1016/j.matdes.2016.11.055.

[94] V. Soni, O.N. Senkov, B. Gwalani, D.B. Miracle, R. Banerjee, Microstructural Design for Improving Ductility of An Initially Brittle Refractory High Entropy Alloy, Sci. Rep. 8 (2018) 1–10. doi:10.1038/s41598-018-27144-3.

[95] Thermo-Calc Software, http://www.thermocalc.com/media/35873/tchea10_extended_info_bh.pdf, [accessed 05 July 17], (2017).

[96] F. Zhang, C. Zhang, S.L. Chen, J. Zhu, W.S. Cao, U.R. Kattner, An understanding of high entropy alloys from phase diagram calculations, Calphad Comput. Coupling Phase Diagrams Thermochem. 45 (2014) 1–10. doi:10.1016/j.calphad.2013.10.006.

[97] E.J. Pickering, R. Muñoz-Moreno, H.J. Stone, N.G. Jones, Precipitation in the equiatomic high-entropy alloy CrMnFeCoNi, Scr. Mater. 113 (2016) 106–109. doi:10.1016/j.scriptamat.2015.10.025.

[98] F. Otto, A. Dlouhý, K.G. Pradeep, M. Kubênová, D. Raabe, G. Eggeler, E.P. George, Decomposition of the single-phase high-entropy alloy CrMnFeCoNi after prolonged anneals at intermediate temperatures, Acta Mater. 112 (2016) 40–52. doi:10.1016/j.actamat.2016.04.005.

[99] N.D. Stepanov, D.G. Shaysultanov, M.S. Ozerov, S.V. Zherebtsov, G.A. Salishchev, Second phase formation in the CoCrFeNiMn high entropy alloy after recrystallization annealing, Mater. Lett. 185 (2016) 1–4. doi:10.1016/j.matlet.2016.08.088.

[100] H. Shahmir, T. Mousavi, J. He, Z. Lu, M. Kawasaki, T.G. Langdon, Microstructure and properties of a CoCrFeNiMn high-entropy alloy processed by equal-channel angular pressing, Mater. Sci. Eng. A. 705 (2017) 411–419. doi:10.1016/j.msea.2017.08.083.

[101] F. Cao, P. Munroe, Z. Zhou, Z. Xie, Medium entropy alloy CoCrNi coatings: Enhancing hardness and damage-tolerance through a nanotwinned structuring, Surf. Coatings Technol. 335 (2018) 257–264. doi:10.1016/j.surfcoat.2017.12.021.

[102] R.S. Ganji, P. Sai Karthik, K. Bhanu Sankara Rao, K. V. Rajulapati, Strengthening mechanisms in equiatomic ultrafine grained AlCoCrCuFeNi high-entropy alloy studied by micro- and nanoindentation methods, Acta Mater. 125 (2017) 58–68. doi:10.1016/j.actamat.2016.11.046.

[103] Z. Fu, W. Chen, H. Wen, D. Zhang, Z. Chen, B. Zheng, Y. Zhou, E.J. Lavernia, Microstructure and strengthening mechanisms in an FCC structured single-phase nanocrystalline $Co_{25}Ni_{25}Fe_{25}Al_{7.5}Cu_{17.5}$ high-entropy alloy, Acta Mater. 107 (2016) 59–71. doi:10.1016/j.actamat.2016.01.050.

[104] N.D. Stepanov, N.Y. Yurchenko, A.O. Gridneva, S. V. Zherebtsov, Y. V. Ivanisenko, G.A. Salishchev, Structure and hardness of B2 ordered refractory

AlNbTiVZr0.5 high entropy alloy after high-pressure torsion, Mater. Sci. Eng. A. 716 (2018) 308–315. doi:10.1016/j.msea.2018.01.061.

[105] N.Y. Yurchenko, N.D. Stepanov, A.O. Gridneva, M. V. Mishunin, G.A. Salishchev, S. V. Zherebtsov, Effect of Cr and Zr on phase stability of refractory Al-Cr-Nb-Ti-V-Zr high-entropy alloys, J. Alloys Compd. 757 (2018) 403–414. doi:10.1016/j.jallcom.2018.05.099.

[106] N.D. Stepanov, N.Y. Yurchenko, S. V. Zherebtsov, M.A. Tikhonovsky, G.A. Salishchev, Aging behavior of the HfNbTaTiZr high entropy alloy, Mater. Lett. 211 (2018) 87–90. doi:10.1016/j.matlet.2017.09.094.

[107] O.N. Senkov, A.L. Pilchak, S.L. Semiatin, Effect of Cold Deformation and Annealing on the Microstructure and Tensile Properties of a HfNbTaTiZr Refractory High Entropy Alloy, Metall. Mater. Trans. A. 49 (2018) 2876–2892. doi:10.1007/s11661-018-4646-8.

[108] J. Čížek, P. Haušild, M. Cieslar, O. Melikhova, T. Vlasák, M. Janeček, R. Král, P. Harcuba, F. Lukáč, J. Zýka, J. Málek, J. Moon, H.S. Kim, Strength enhancement of high entropy alloy HfNbTaTiZr by severe plastic deformation, J. Alloys Compd. 768 (2018) 924–937. doi:10.1016/j.jallcom.2018.07.319.

[109] D.H. Lee, J.A. Lee, Y. Zhao, Z. Lu, J.Y. Suh, J.Y. Kim, U. Ramamurty, M. Kawasaki, T.G. Langdon, J. Il Jang, Annealing effect on plastic flow in nanocrystalline CoCrFeMnNi high-entropy alloy: A nanomechanical analysis, Acta Mater. 140 (2017) 443–451. doi:10.1016/j.actamat.2017.08.057.

[110] N.A.P. Kiran Kumar, C. Li, K.J. Leonard, H. Bei, S.J. Zinkle, Microstructural stability and mechanical behavior of FeNiMnCr high entropy alloy under ion irradiation, Acta Mater. 113 (2016) 230–244. doi:10.1016/j.actamat.2016.05.007.

[111] P.K. Liaw, T. Egami, C. Zhang, F. Zhang, Y. Zhang, Radiation Behavior of High-Entropy Alloys for Advanced Reactors, Final Report, (2015). DOE/NEUP--11-3196

[112] S. Qin Xia, Z. Wang, T. Fei Yang, Y. Zhang, Irradiation Behavior in High Entropy Alloys, J. Iron Steel Res. Int. 22 (2015) 879–884. doi:10.1016/S1006-706X(15)30084-4.

[113] S.J. Zinkle, L.L. Snead, Designing Radiation Resistance in Materials for Fusion Energy, Annu. Rev. Mater. Res. 44 (2014) 241–267. doi:10.1146/annurev-matsci-070813-113627.

List of appended papers

Paper A
B. Schuh, B. Völker, J. Todt, K.S. Kormout, N. Schell, A. Hohenwarter
Influence of annealing on microstructure and mechanical properties of a nanocrystalline CrCoNi medium-entropy alloy
Materials 11 (2018), 662 (Pg. 1-18)

Paper B
B. Schuh, R. Pippan, A. Hohenwarter
Tailoring bimodal grain size structures in nanocrystalline compositionally complex alloys to improve ductility
Submitted for publication in SCI-Journal

Paper C
B. Schuh, B. Völker, V. Maier-Kiener, J. Todt, J. Li, A. Hohenwarter
Phase Decomposition of a Single-Phase AlTiVNb High-Entropy Alloy after Severe Plastic Deformation and Annealing
Advanced Engineering Materials 19 (2017), 1600674 (Pg. 1-10)

Paper D
B. Schuh, B. Völker, J. Todt, N. Schell, L. Perriere, J.Li, J.P. Couzinié, A. Hohenwarter
Thermodynamic instability of a nanocrystalline, single-phase TiZrNbHfTa alloy and its impact on the mechanical properties
Acta Materialia 142 (2018), 201-212

Remarks

In the appended papers, I, Benjamin Schuh, performed all the experiments, the data analyses and the composition of the publications with the following exceptions:

In **Paper A**, B. Völker performed the TEM investigations, K.S. Kormout, J. Todt and N. Schell performed the XRD synchrotron measurements at DESY.

In **Paper C**, B. Völker performed TEM investigations, V. Maier-Kiener carried out the nanoindentation experiments, J. Li provided the material and J. Todt assisted with the XRD synchrotron measurements at DESY.

In **Paper D**, B. Völker performed the TEM investigations. L. Perriere and J.P. Couzinié provided the material and the corresponding THERMOCALC data. J.Li provided additional material. J. Todt assisted with the XRD synchrotron measurements at DESY.

A.

Influence of annealing on microstructure and mechanical properties of a nanocrystalline CrCoNi medium-entropy alloy

B. Schuh [a], B. Völker [a,d], J. Todt [b], K.S. Kormout [b], N. Schell [c], A. Hohenwarter [a]

[a] Department of Materials Physics, University of Leoben, Jahnstraße 12, 8700 Leoben, Austria

[b] Erich Schmid Institute of Materials Science, Austrian Academy of Sciences, Jahnstraße 12, 8700 Leoben, Austria

[c] Institute of Materials Research, Helmholtz-Zentrum Geesthacht, 21502 Geesthacht, Germany

[d] Now at : Materials Chemistry, RWTH Aachen University, Kopernikusstrasse 10, 52074 Aachen, Germany &Max-Planck-Institut für Eisenforschung GmbH , Max-Planck-Straße 1, 40237 Düsseldorf, Germany

Abstract

An equiatomic CrCoNi medium-entropy alloy was subjected to high-pressure torsion. This process lead to a refinement of the microstructure to a grain size of about 50 nm, combined with a strong increase in the materials hardness. Subsequently the thermodynamic stability of the medium entropy alloy was evaluated by isothermal and isochronal heat treatments. Annealed samples were investigated by scanning and transmission electron microscopy as well as X-ray diffraction and were subjected to tensile tests to establish microstructure-property relationships. Furthermore, a comparison of mechanical properties with a grade 316L stainless steel was performed in order to evaluate if the CrCoNi alloy is competitive with commercially available structural materials in the nanocrystalline state. A minority phase embedded in the face-cent red cubic matrix of the CrCoNi alloy could be observed in multiple annealed states, as well as the as-received and HPT-processed material. For 200 hours of annealing at 500 °C it was determined that the minority phase has a hexagonal-closed-packed crystal structure. A possible explanation for the formation of the phase is a preferential segregation of Co to stacking faults.

A.1 Introduction

High-entropy alloys (HEAs) are a new class of metallic materials, consisting of multiple principal elements, which ideally should form a single-phase microstructure with a simple crystal structure [1,2]. However, in recent years it was shown that only a small subset of systems remain a true single-phase alloy after homogenization. Additionally, in many cases second phases were intentionally introduced to improve material properties. Such materials, still based on the original idea of HEA, but with multi-phase microstructures are nowadays usually referred to as compositionally complex alloys (CCAs).

The so-called Cantor-alloy, which consists of CrMnFeCoNi in an equiatomic composition, has been intensively examined over the last years encompassing many significant mechanical [3–7] and various physical aspects [8–11]. Recently these investigations have been extended to the nanocrystalline (NC) grain-size regime accessible by means of severe plastic deformation (SPD) [12–17]. After transformation of the coarse-grained (CG) pre-material into a NC-structure the pure single-phase solid solution character was maintained combined with a substantial increase of strength. However, it was found that the alloy was not thermally stable below approximately 800 °C. For relatively low temperature anneals the structure decomposed into a NC multiphase microstructure, constituting of a MnNi phase, a Cr-rich phase, and a Fe–Co phase embedded in the HEA matrix [12]. The relatively fast transformation kinetics at low temperatures can be comprehended in terms of the large fraction of grain boundaries present in the NC-state serving as fast diffusion pathways and preferential nucleation sites. Since the same phase decomposition was also shown for coarse-grained microstructure [18–20], it was ascertained that the decomposition behavior is not a mere peculiarity of the NC-state. Therefore the accelerated kinetics of the NC-state offer a convenient outlook on the long-term stability of HEAs without having to rely on time-consuming annealing experiments and site-specific investigation methods.

Recently, a subvariant of the Cantor-alloy and so called “medium-entropy alloy” (MEA), which consists of CrCoNi in an equiatomic composition has gained the attention of the HEA community [21–27]. This alloy has already been proven to possess a single-phase fcc-crystal structure in the CG-state [28]. Since this subtype lacks Mn and Fe, the MnNi and FeCo phase and even the Cr-rich phase, which also contains a substantial amount of iron, found for the NC-Cantor alloy will not be able to form in this constitution upon annealing. However, the CrCoNi alloy has higher amounts of the remaining alloying elements, so the formation of different intermetallic phases upon annealing cannot be excluded beforehand. Recently, it has been also reported that this system exhibits even better mechanical properties than the quintanary base-alloy [21,24].

Based on these considerations the equiatomic ternary CrCoNi-alloy was subjected to high pressure torsion to obtain a NC-microstructure. Then, various annealing experiments were performed and samples were microstructurally and mechanically investigated. Firstly, similar as for the NC Cantor alloy, the long term phase stability can be explored. Secondly, if the single-phase character was maintained or new intermetallic phases were found, the comparison of the hardening response of the ternary with the quintinary system could give new insights into the necessity and significance of precipitates on hardening phenomena as a result of annealing treatments in NC-alloys. The sum of all collected results and their interpretation will extend the knowledge on the mechanical properties of the CG – high performance CrCoNi alloy into the NC grain size regime.

A.2 Materials and Methods

Cylindrical CrCoNi ingots (25.4 mm in diameter, 127 mm in length) were produced from high-purity elements (>99.99 wt%) using arc melting and drop casting under Ar atmosphere. Subsequently, the as-cast ingots were encapsulated in evacuated quartz ampules and heat treated at 1200 °C for 48 h, the procedure being similar to the one in Reference [3]. The homogenized material was processed by quasi-constrained HPT [29]. The HPT process was performed on samples with a diameter of 8 mm, a thickness of 0.8 mm, and at room temperature with a pressure of 7.8 GPa using a rotational speed of 0.2 rotations/min. During HPT the applied shear strain γ can be calculated from the sample radius r, the sample thickness t and the number of rotations n:

$$\gamma = \frac{2\pi rn}{t} \ (-) \qquad \textbf{Equation A.1}$$

At shear strains of $\gamma > 50$ a microstructural equilibrium is reached and some microstructure features, such as grain size, remain constant even if much higher strains are applied. A γ of 50 approximately equals a radial position of 1 mm after 5 rotations. Samples that have reached this equilibrium condition or so called "steady-state" regime were subsequently subjected to annealing treatments. Isochronal heat treatments were performed for 1 h between temperatures of 100 °C and 1000 °C. Additionally isothermal heat treatments at 500 °C were performed for up to 200 h.

For mechanical testing, hardness measurements as well as tensile tests were conducted. Hardness testing was done on a microhardness tester from Buehler (Micromet 5104 using a load of 1000 gf and a dwell time of 15 s). Tensile samples were prepared by a newly developed grinding tool to manufacture miniaturized, circular tensile samples. Two tensile samples were prepared per HPT disk that had undergone 5 rotations, with the gauge length of the tensile samples located at a radius of 2 mm and therefore already well within the microstructural steady-state regime. Tensile tests were performed at room temperature in a tensile testing machine from Kammrath and Weiss (Model 5000N) using a 2 kN load cell and a crosshead speed of 2.5 µm/s. 3 samples were tested per investigated microstructural state. All data were then evaluated by using automated digital image correlation utilizing the MatLab software package [30]. All further details on specimen production, tensile testing and data evaluation can be found in Reference [31].

Investigations of the microstructure were performed with both, a scanning electron microscope (SEM, Zeiss 1525) and transmission electron microscope (TEM, JEOL 2100F). Samples for the SEM were first mechanically ground and polished and finished by electrochemical polishing (A2 solution from Struers). TEM samples were initially ground to 100 µm thickness, subsequently mechanically dimpled to about 10 µm and then additionally thinned utilizing Ar ion-milling. X-ray diffraction (XRD) experiments were performed at the DESY photon science facility PETRA III High Energy Materials Science beamline P07 operated by Helmholtz Zentrum Geesthacht. A beam energy of 87.1 keV was employed and a NIST standard LaB_6 powder was used as a reference material to calibrate the detector geometry. Data analysis was performed using FIT2D [32] and Match! [33] utilizing the crystallography databases Crystallography Open Database, PDF-2 and the Inorganic Crystal Structure Database.

A.3 Results

A.3.1 As-received material and deformation

The as-received material was studied first utilizing a back-scattered electron (BSE) detector in the SEM, see Figure 1 a). In this microstructural state the CrCoNi alloy has grain sizes of several 100 µm and the equiatomic character of the alloy was confirmed by performing an energy-dispersive X-ray (EDX) line scan consisting of 100 individual points. The averaged results of this line-scan can be found in the inset of Figure 1 a). In-depth investigations via bright-field (BF) TEM imaging revealed an abundance of fine annealing twins in the as-received material, Figure 1 b). The corresponding selected area electron diffraction (SAED) pattern can be seen in the inset of Figure 1 b). Due to the large grain size of the as-received state with respect to the used aperture the diffraction pattern consists of a single face-centered-cubic (fcc) crystal. However, additional Debye-Scherrer rings are recognizable as well. Corresponding dark-field (DF) imaging shows that the additional rings originate from a minority phase with a size of only a few nanometers embedded in the fcc CrCoNi matrix (Figure 1 c)). The number of Debye-Scherrer rings was insufficient to accurately determine the crystal-structure of the minority phase.

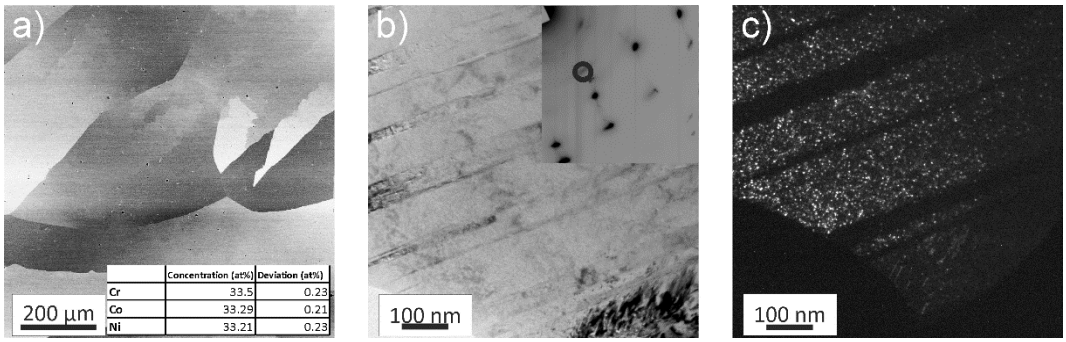

Figure 1: a) BSE image of the coarse-grained as-received microstructure. The inset shows the chemical composition as determined by SEM-EDX. High-magnification BF image in the TEM of the same microstructure state, b). The inset depicts an electron-diffraction pattern, showing the presence of a minority phase. The circle marks the selected diffracted beam used for the DF image shown in c), where the nanoscale minority phase can be seen.

A.3.2 Microstructural evolution during processing and steady-state microstructure

Hardness results in Figure 2 a) were obtained by averaging the value of four indents taken at the same radius (except for center indent). The undeformed specimen has a hardness of approximately 190 HV1. The hardness increases quickly with applied shear strain, due to the strong grain refinement caused by mechanical twinning. Even the sample deformed only for ¼ rotations has almost reached the hardness of the steady-state regime at edge regions. That the steady-state regime is reached for $\gamma > 50$ is also well reflected in the fact that the hardness levels off into a plateau. The hardness plateau occurs at an average Vickers microhardness of ~ 570 HV1, therefore processing of the coarse-grained as-received state down to a NC microstructure lead to an approximately threefold increase in

hardness. Compared to the five-component CrMnFeCoNi alloy the hardness of the NC state of CrCoNi is slightly increased [12].

In Figure 2 b) - e) changes in microstructure during HPT processing are documented using a BSE detector. Figure 2 b) shows the disk center region after n = ¼ rotations, which ideally is only deformed by compression. For very low applied strains in the vicinity of the disk center, the formation of dislocation cells and substructures can be observed. For slightly higher shear strains, Figure 2 c), a high density of deformation twins is seen. At higher strains additional twin variants start to occur and twins start to intersect each other, giving rise to a block-like structure, see Figure 2 d). At outer edge regions (r > 3 mm) after ¼ rotations ($\gamma \sim 6$) the formation of a NC-microstructure is already observed, Figure 2 e). At these relatively low shear strains however, the microstructure is not fully homogenous, as it would be expected if the steady-state regime had already been reached. A full homogenization of the structure is only reached for $\gamma > 50$.

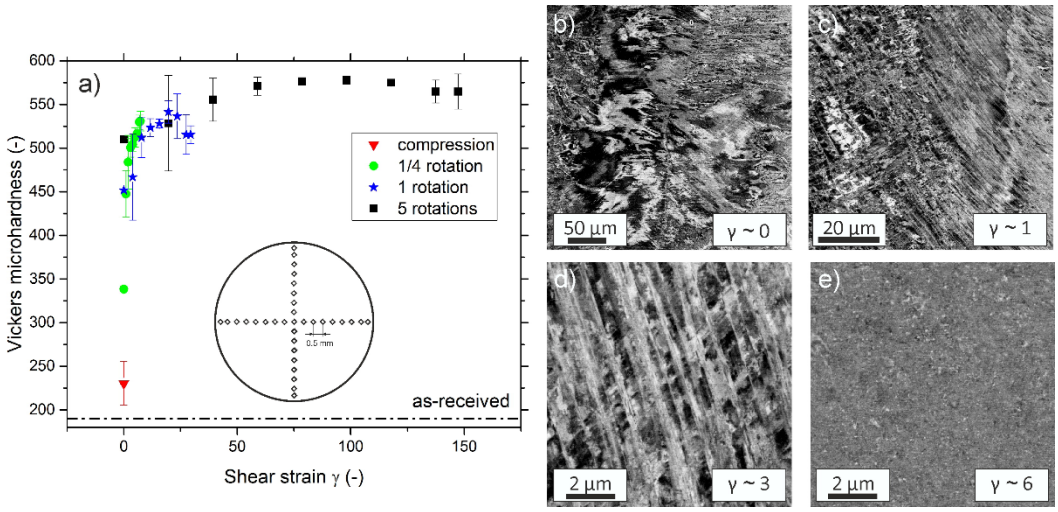

Figure 2: a) Evolution of hardness plotted versus the shear strain applied by HPT. A plateau is reached for shear strains larger than approximately 50. b) – e) depict changes in the microstructure during processing. For the low strain region near the center large contrast variations are visible, which suggest the formation of dislocation substructures as well the onset of twinning, b). Even for very low strains mechanical twinning is a dominant deformation mechanism, see c). For slightly higher strains, d), additional twin variants are forming and twins start to intersect each other. e), at $\gamma \sim 6$ some regions are already extremely refined, but the microstructure still is not completely homogeneous.

The steady-state microstructure was studied more thoroughly in the TEM. Figure 3 a) shows a scanning TEM (STEM) image of the NC state while Figure 3 b) depicts a high-angle annular DF (HAADF) image of the same position. The formation of non-equilibrium grain boundaries during HPT and their characteristic property of exhibiting high elastic stresses/strains [34,35] leads to often poorly discernible structures and boundaries, thus making an exact measurement of the saturation grain size difficult. However, based on the grains that are clearly visible in DF images it can be estimated that the saturation grain size of the CrCoNi-alloy is in the range of 50 nm, similar to the CrCoFeMnNi alloy [12]. In the SAED pattern (Inset of Figure 3 c)) the expected sequence of Debye-Scherrer rings corresponding to a fcc-phase with a lattice constant of approximately 3.6 Å can be seen. Additionally, an extra set of very faint rings is observable, similar to the as-received state

(Figure 1 b)). These, again, can be matched to nanoscale precipitates, embedded in the fcc-CrCoNi matrix, with a size of only a few nanometers via DF imaging, see Figure 3 c). However, during HAADF imaging these precipitates are not visible (Figure 3 b)). Figure 3 d) shows synchrotron XRD data in which the presence of a fcc phase with a lattice parameter of a = 0.3567 nm as well as a the minority phase could be confirmed. Due to the fact that the presence of this phase is only indicated by a single peak, the crystal structure of this phase could not be determined.

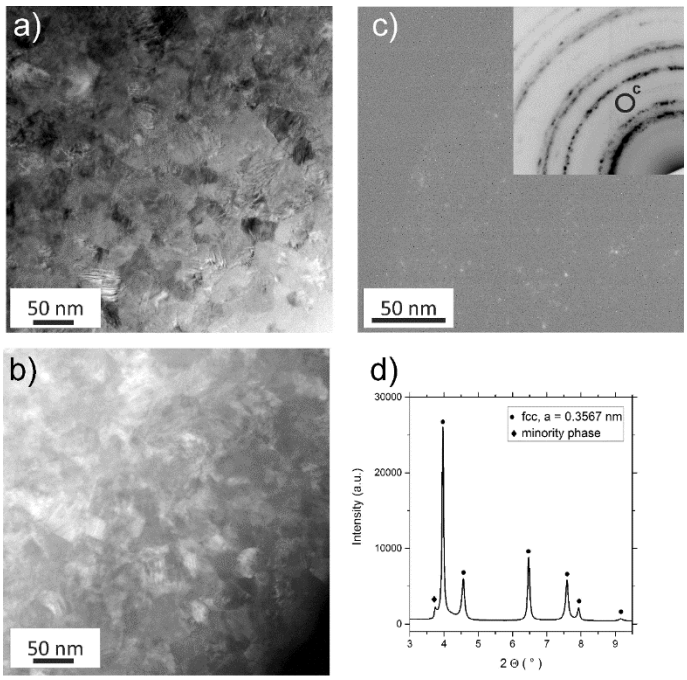

Figure 3: a) STEM BF image of the steady-state microstructure after HPT processing. b) A STEM HAADF image of the same position, the minority phase cannot be observed in this imaging mode. c) A DF image of the minority phase, with a corresponding SAED pattern in the inset. In d) the findings are confirmed via synchrotron XRD measurements. a) and c) do not depict the same sample position.

A.3.3 Annealing response of NC-CrCoNi

Hardness values for the annealed samples were obtained by averaging the results of seven indents, the error bars represent the standard deviation, see Figure 4 a) and b). Isochronal heat treatments performed for temperatures between 100 °C and 1000 °C (t = 1 h) show a significant increase in the material's hardness, reaching its maximum at 500 °C, where a hardness of ~ 700 HV1 is measured. In comparison to the HPT processed state with a hardness of 570 HV1 this means an increase of more than 20 %. For elevated annealing temperatures, the alloy's hardness decreases rapidly, eventually reaching values of the as-received material for an annealing temperature of 1000 °C.

The kinetics of the hardening process can be estimated from the isothermal heat treatments performed at 500 °C, Figure 4 b). Even for just 5 minutes of annealing a hardness increase of about 100 HV1 occurs. The maximum hardness for isothermal heat treatments is reached for 5 h of annealing, approximately 720 HV1. For longer annealing times at this temperature, the hardness decreases to about 530 HV1 for 200 h of annealing.

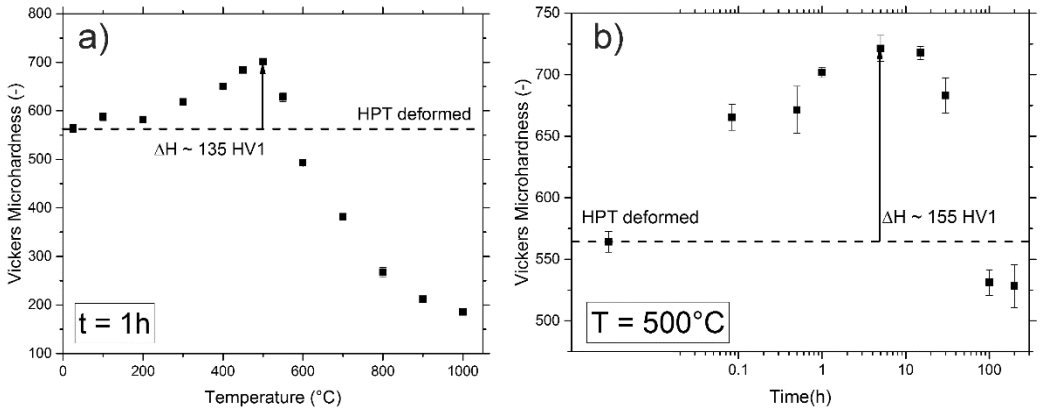

Figure 4: a) Hardness evolution during isochronal heat treatment (t = 1 h) for temperatures between 100 °C and 1000 °C. b) Changes in hardness during isothermal annealing at 500 °C for times ranging from 5 minutes to 200 h.

A.3.3.1 Annealed Microstructure

In Figure 5 a) the microstructure of a specimen annealed for 1 h at 500 °C is presented. In comparison to the HPT processed state the microstructure is clearer and boundaries are well-defined. A 1h anneal leads to slight grain coarsening and an abundance of recrystallization twins can be seen in the individual grains. The SAED pattern as seen in the inset of Figure 5 b) does not show significant changes compared to the HPT state. One set of Debye-Scherrer rings can still be attributed to the fcc CrCoNi-MEA phase and the other set of faint rings suggest that the minority phase is still present. The corresponding DF image reveals that the minority phase has not changed its morphology (Figure 5 b))

For the 100 h at 500 °C annealed state a majority of grains are already in the range of several micrometers, while a few areas still have grains in the NC grain size regime, indicating an abnormal grain growth, see Figure 5 c). Significantly prolonging the heat treatment has again only little influence on the particle morphology of the minority phase, Figure 5 d).

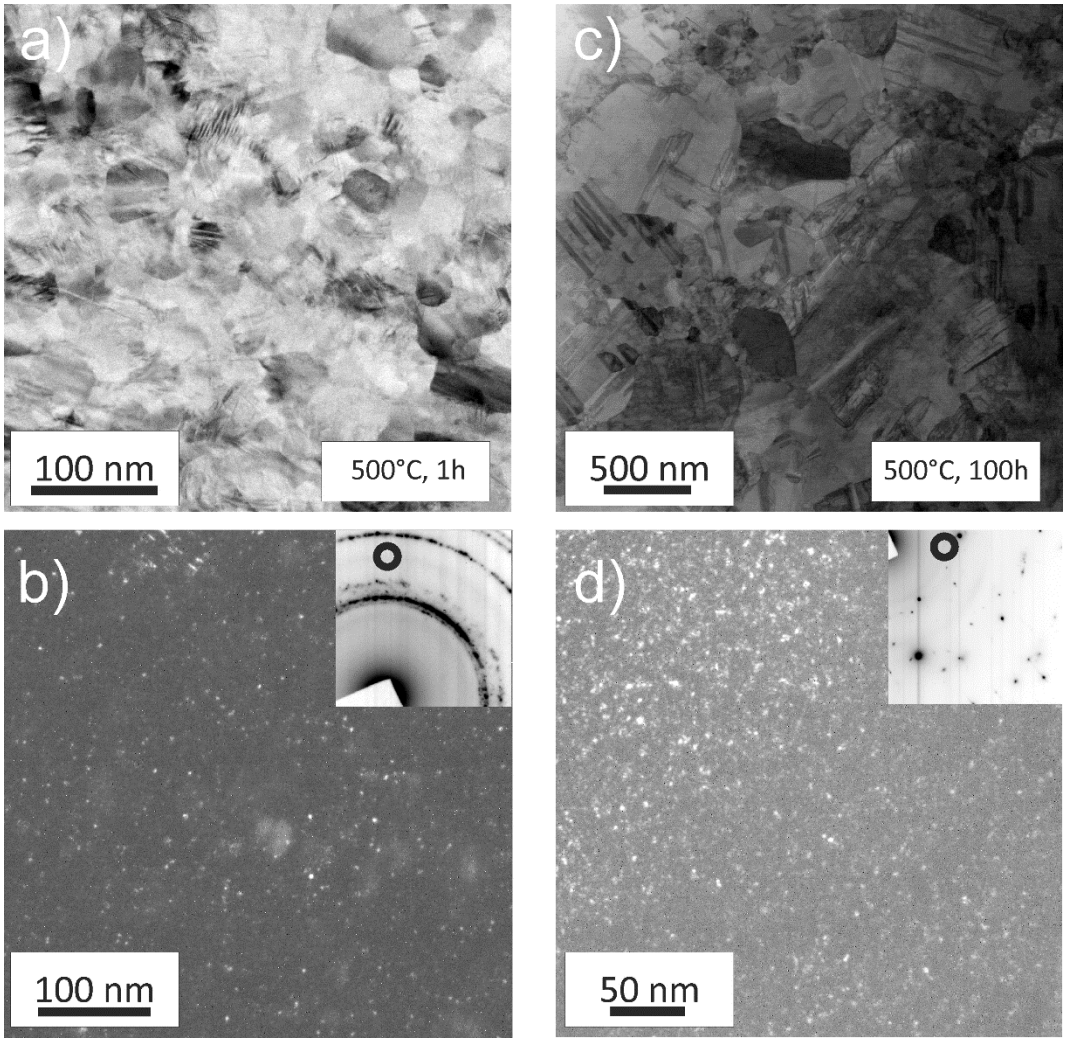

Figure 5: TEM micrographs of the samples annealed at 500 °C for 1h (a) and b)) as well as 100 h (c) and d)). a) A BF image depicting that little grain growth occurs after just 1h. b) A DF image of the minority phase with the corresponding SAED pattern in the inset. c) After 100 h abnormal grain growth set in and some grains have grown significantly. The presence of the minority phase can still be reported after prolonged annealing, d).

While annealing at 500 °C for longer times leads to abnormal grain growth, for higher annealing temperatures such as at 700 °C a homogenous microstructure can be achieved during 1 h of annealing, as is depicted in Figure 6 a). At this temperature the microstructure is fully recrystallized and grains have significantly grown compared to the initial HPT state. As expected for a low stacking fault energy material the annealing treatment leads to an abundance of recrystallization twins. Additional Debye-Scherrer rings can be spotted in the TEM, see inset 6 a). Figure 6 b) shows a corresponding DF image of the area. The minority phase remains similar in size and shape despite the annealing treatment at higher temperatures.

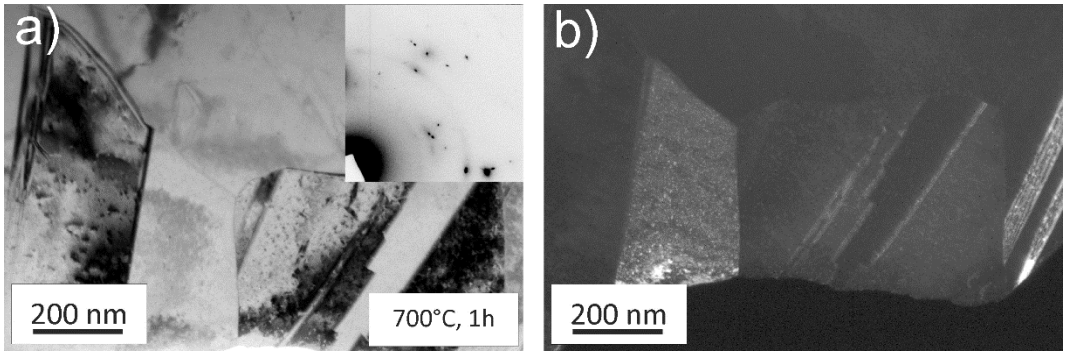

Figure 6: a) TEM image of the microstructure after a 700°C, 1h annealing treatment. Grains are no longer in the NC grain size regime and are featuring recrystallization twins. The minority phase can still be found, see b) and inset of a).

At 600 °C, Figure 7 a), the microstructure is already fully recrystallized and an abundance of annealing twins can be seen inside the grains. Between 700 °C and 1000 °C (Figure 7 b) - e)) the grain sizes gradually become larger, up to a size of about 20 µm measured for the 1000 °C, 1h annealing state, as determined by area-weighted electron back-scatter diffractions scans (EBSD, not shown in present manuscript). For none of the above mentioned annealing states any signs of second phase precipitation or the onset of a phase decomposition could be observed in the SEM.

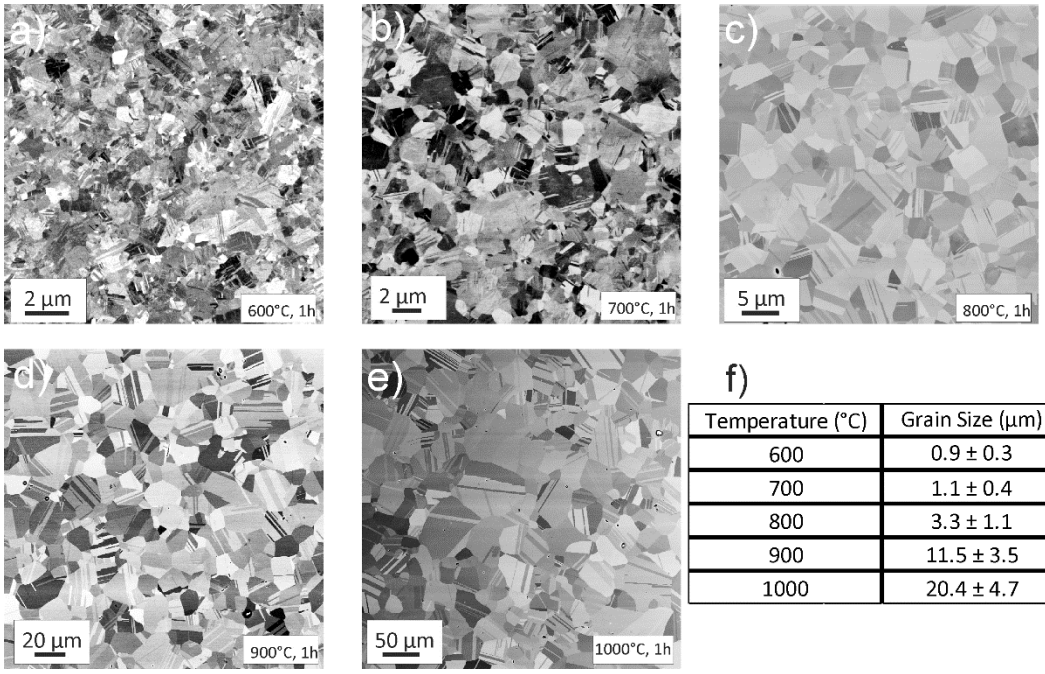

f)

Temperature (°C)	Grain Size (µm)
600	0.9 ± 0.3
700	1.1 ± 0.4
800	3.3 ± 1.1
900	11.5 ± 3.5
1000	20.4 ± 4.7

Figure 7: BSE-SEM images depicting the microstructure after 1h annealing treatments at, a) 600 °C, b) 700 °C, c) 800 °C, d) 900 °C and e) 1000 °C. In all cases the microstructure is fully recrystallized, homogenous and features an abundance of annealing twins. The average grain size as determined by area-weighted EBSD scans can be seen in f).

A.3.3.2 Phase identification via XRD

Annealed specimens were additionally investigated utilizing synchrotron XRD measurements, Figure 8 a) - c). In Figure 8 a) the results for isochronal heat treatments (t = 1 h) can be seen, b) shows samples annealed at 500 °C for different times and c) depicts a magnified version of the area marked with the dotted rectangle in b). As already presented in Section 3.2, the HPT deformed state features a single phase with fcc crystal structure (a = 0.3567 nm) as well as a single peak of the unknown minority phase. Due to the high defect density and small grain size in HPT processed materials all peaks are significantly broadened. For higher annealing temperatures, Figure 8 a), or longer annealing times, Figure 8 b), the onset of recovery and eventually recrystallization, leads to a strong decrease of the average peak width. As depicted in Figure 8 a) the single peak that indicates the presence of the minority phase can no longer be detected for annealing temperatures of 700 °C and higher. On the contrary, during isothermal annealing at 500 °C the peaks of the minority phase become more pronounced. These more pronounced peaks in combination with the narrower peak width caused by defect-annihilation leads to the revelation of further minority phase peaks (see detailed view, Figure 8 c)) and allowed an unambiguous identification of the phase. Its crystal structure can be determined to be of the hexagonal-close-packed (hcp) type. The corresponding lattice parameters are: a = 0.252 nm and c = 0.411 nm.

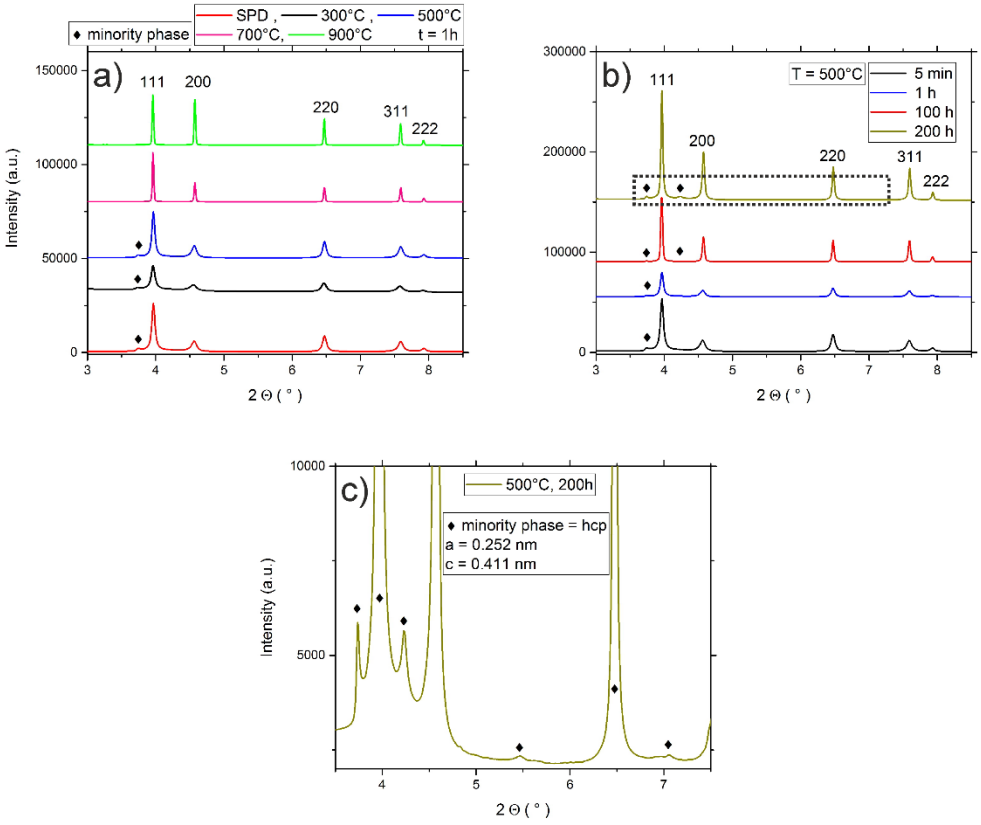

Figure 8: a) Synchrotron XRD measurements of isochronally (t = 1 h) annealed samples. For the HPT processed sample as well as for annealing temperatures up to 500 °C the minority phase can still be seen in addition to the fcc phase. For higher temperatures it can no longer be detected utilizing XRD. b) Isothermal, T = 500 °C, annealed samples – peak width gets continuously reduced due to a decrease in defect density. For the 200 h annealed samples the minority phase can be identified to be a hcp phase, see detailed view in c).

A.3.4 Tensile tests and comparison of mechanical properties

The results of the tensile tests for the CrCoNi alloy are presented in Figure 9 and the typical measures including area reduction are compiled in Table 1 (cf. Section 4.3). The coarse-grained, as-received state of the CrCoNi alloy has a yield-strength of approximately 216 MPa and features a good work-hardening rate, which enables uniform elongation to high strains. The ultimate tensile strength (UTS) of this microstructural state is about 461 MPa and the average elongation to failure is about 37 %. HPT processing and achieving a NC microstructure heavily impacts the mechanical properties in the CrCoNi alloy. The UTS increases to almost 2100 MPa, while the elongation to failure strongly decreases to only about 5 %. Annealing the NC samples at 500 °C for 1 h has negative effects on the tensile properties, since samples often fracture in the elastic regime of the tensile tests. However, the UTS of this microstructural state is still higher than in HPT processed samples. Achieving a homogenous grain size of about 3 µm, as for instance can be done by annealing the sample at 800 °C for 1 h (see Figure 7 c)), leads to very balanced mechanical properties. Yield strength (~ 512 MPa) and UTS (~ 836 MPa) are far superior to the as-received state, while still achieving a similarly high elongation to failure of over 30 %.

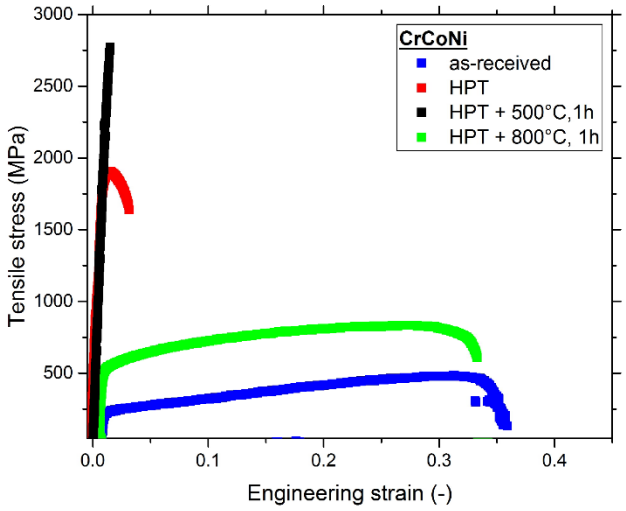

Figure 9: Tensile curves of the as-received state, the nanocrystalline HPT state and two annealed states of the CrCoNi alloy.

A.4 Discussion

A.4.1 As-received state and deformation behavior

The deformation behavior of the CrCoNi alloy during HPT processing is very similar compared to that of the CrMnFeCoNi alloy [12]. For both materials a strong tendency for mechanical twinning during deformation, at least at lower temperatures, is reported in literature [5,7,21,36] , but the onset of twinning for the CrCoNi alloy should happen at much lower strains compared to the CrMnFeCoNi alloy . This also is stated to be one of the reasons for the superior mechanical properties of the CrCoNi alloy, since it leads to an extended strain range with an increased work hardening capacity [24]. In general, during HPT processing of the CrCoNi alloy the deformation behavior is as expected of a single-phase fcc alloy with low to medium stacking fault energy: For low shear strains plastic

deformation is mostly mediated by dislocation glide and multiplication. For higher shear strains micro-shear banding but also mechanical twinning are activated. A further increase in strain usually leads to an activation of additional twin variants, which results in profuse intersection of twins with different orientations. For extremely high strains of several thousand percent an almost homogenous microstructure featuring NC grains is formed [37].

During interrupted tensile testing Miao et al. [38] could observe the formation of a hcp-phase with a lath-like morphology both at room temperature as well as 77 K. During HPT processing extremely high strains were applied and after long term annealing at 500 °C for 200 h (see Figure 8 c)), a hcp phase with similar lattice constant could clearly be identified in the CrCoNi alloy (literature values by Miao et al. [38], a ~ 2.55 Å and c ~ 4.1 Å). However, the morphologies of the phases are vastly different. While the deformation induced hcp-phase observed by Miao et al. [38] has a lath-like morphology, the minority phase observed in this publication consists of nanoscale, spherical precipitates. The possibility that the minority phase in the present case is deformation induced can be excluded from the fact that it can, for instance, also be observed in the as-received samples, which were long-term annealed at 1200°C.

A.4.2 Hardness changes during annealing treatments

The CrCoNi alloy is experiencing a large increase in hardness during low-temperature annealing for temperatures up to 550 °C. Such “hardening by annealing” phenomena are frequently observed in NC material, even without precipitation of second phases or similar hardening mechanisms [39–41] and seems to be linked to a material specific threshold grain size [42]. The exact reasons for the hardening are still controversially discussed in the literature, the common denominator is that it is linked to dislocation-grain boundary interactions. An often suggested explanation is that the hardening by annealing phenomena are caused by segregation of solutes to grain boundaries, as for instance described by Valiev et al. in Al alloys [43]. The elevated solute concentration should hinder the emission of dislocation due to solute-drag effects. Additionally, if there is a non-uniform distribution of solutes at the grain boundaries, the effectiveness of the pinning effect is varying as well, which should result in some dislocation segments not being emitted from the grain boundary [43]. Another possibility is that annealing of NC samples leads to abundant dislocation annihilation at the large amount of grain boundaries available. Since this leaves the grain interior mostly starved of possible sources of dislocation nucleation, the majority of mobile dislocations has to be emitted from grain boundaries in order to accommodate a subsequent plastic deformation. However, the annealed grain boundaries should be in a relaxed state compared to grain boundaries after HPT deformation, making an emission of dislocations less likely [41]. Tong et al. come to a similar conclusion after molecular dynamics studies on NC alpha-iron, where they could demonstrate that the strengthening effect caused by moderate annealing temperatures is caused by the reduced amount of dislocation sources and the equilibration of grain boundaries [44]. These findings are supported by experimental studies from Renk et al. [39] where mechanical data and analysis of grain boundary chemistry via atom probe tomography were combined. It was concluded that while grain boundary segregation is occurring in the investigated 316L steel, the changes in mechanical properties are independent of solute content present at the boundaries and the hardening can be attributed to dislocation annihilation and grain boundary relaxation [39].

In the present study isothermal anneals at 500 °C were performed in order to determine the kinetics of the hardening process occurring in the CrCoNi alloy, see Figure 4 b). It could be shown that a major hardness difference is already occurring after just 5 minutes

of annealing, similar to what was observed in Reference [39] in the case of the single-phase austenitic 316L steel. Renk et al. concluded that the short time frame in which the hardening sets in is one indication for a dislocation driven process, since segregation to boundaries after just 5 minutes should be rather limited given the low annealing temperatures. In the present study two additional factors are further complicating insights into the hardening mechanism – Firstly, the unexpected presence of an additional nanoscaled phase with a currently unquantified influence on the mechanical properties. Secondly, unlike in the 316L steel, where segregation of solutes to grain boundaries is occurring after long-time annealing and stabilizing the microstructure against grain growth, the CrCoNi alloy is very prone to grain growth even at low annealing temperatures, as can be seen in Figure 5 c). The highly stable microstructure in the case of the 316L steel results in the fact that the hardness levels off into a plateau. Therefore the theory that segregation of solutes to the grain boundaries lead to a further hardening can be ruled out.

In the present case, hardness during isothermal annealing at 500 °C is increased in relation to the hardness of HPT samples until annealing times of about 100 h. This is most likely caused by two major reasons – The onset of substantial grain growth in the CrCoNi alloy at this temperature cannot be observed for relatively short annealing times (see Figure 5 a), for 1h of annealing). Additionally, a further precipitation of the minority phase is likely occurring at this annealing temperature, as can be seen in the XRD plot in Figure 8 b) and c), since peaks of the minority phase are getting more pronounced. The observed hardness evolution over time at 500 °C therefore can be explained by the fact that in combination with the "hardening by annealing" phenomena, there likely is an additional contribution by the precipitation of the minority phase, which eventually gets counteracted by the onset of grain growth. As for the cause of the hardening by annealing phenomena – Given that both processes, dislocation annihilation and a possible solute segregation are occurring simultaneously, it is not yet possible to discern which factor is the dominant one.

A.4.3 Comparison of mechanical properties

In order to determine if the CrCoNi alloy can compete with commercial materials currently used in structural applications the mechanical properties are compared to a single-phase, austenitic steel, Böhler A220 (which is equivalent to Grade 316L). 4 different microstructural states were tested with 4 samples each - The material as-received from the producer, after HPT processing for 5 rotations at room temperature with 0.2 rotations/minute, and then the HPT processed materials after 1 h annealing treatments at 500 °C and 800 °C. The results can be found in Figure 10. The as-received state of the A220 material is very coarse grained, with grains usually being larger than 100 µm. Similar to the CrCoNi alloy it features a relatively low yield (~ 250 MPa) and UTS (~ 400 MPa) but a high elongation to failure of approximately 40 %, the main cause of which is also a high work hardening rate which allows the material to sustain uniform elongation to high strains by delaying the onset of damage localization. The HPT processed samples face similar issues as the CrCoNi alloy – While having a high UTS comparable to the CrCoNi, the ductility is extremely limited due to an early onset of necking and subsequent ductile failure. Despite remaining in a single-phase state the A220 material suffers a further decrease in ductility after low temperature annealing at 500 °C for 1h. The fracture surfaces, see Figure 11 c) show a dimple fracture, yet the failure occurs basically in the elastic regime of the tensile test. However, like for the CrCoNi alloy, this low-temperature annealing leads to a further increase in UTS by about almost 20% to approximately 2170 MPa. At 800 °C for 1 h a good strength-ductility balance is reached – The UTS is reasonably high, 730 MPa, and the elongation to failure is over 25%. The grain size after annealing at 800 °C is slightly lower than for the CrCoNi alloy (~ 2 µm, area-weighted EBSD scan, not shown). The main reason for this is that at 800 °C a σ-phase precipitates to the grain

boundaries (see fracture image, Figure 11 d) which hinders grain boundary movement and subsequently grain growth. Despite the formation of this second phase the tensile properties remain excellent. A comprehensive study of the influence of HPT processing and subsequent annealing treatments for the A220 alloy can additionally be found in reference [39].

Mechanical properties are summarized in Table 1 – Overall the mechanical properties of the CrCoNi MEA and the A220 alloy are comparable.

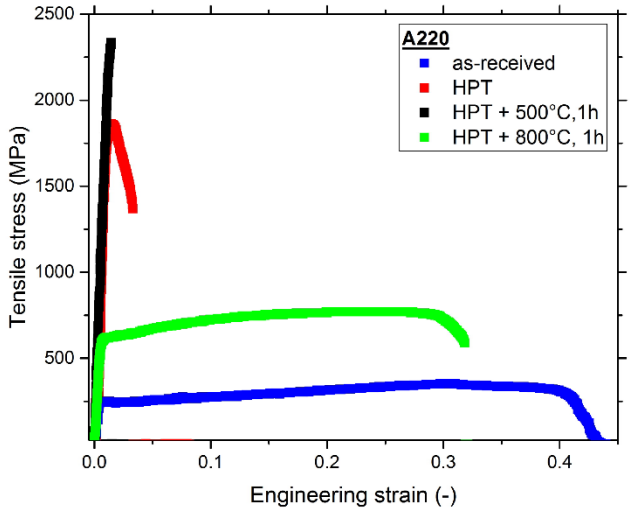

Figure 10: Tensile curves of the as-received state, the nanocrystalline HPT state and two annealed states of the A220 stainless steel.

Microstructural State		Tensile strength (MPa)	Elongation to failure (%)	Yield Strength $\sigma_{0.2}$ (MPa)	Area Reduction (%)
CrCoNi	as-received	461 ± 38	37 ± 2	216 ± 10	73 ± 2
	HPT	2095 ± 168	4.7 ± 1.3	1901 ± 67	15 ± 5
	500 °C, 1h	2760 ± 33	1.5 ± 0.02	/	1.0 ± 1.8
	800 °C, 1h	836 ± 61	37 ± 5	512 ± 53	70 ± 4
A220	as-received	398 ± 58	43 ± 10	247 ± 26	91 ± 12
	HPT	1836 ± 127	4.3 ± 2.3	1729 ± 48	46 ± 3
	500 °C, 1h	2172 ± 215	1.7 ± 0.3	~ 1900 *	14 ± 12
	800 °C, 1h	733 ± 48	26 ± 9	580 ± 45	68 ± 2

* Not all specimens yield before fracture

Table 1: Mechanical properties of the CrCoNi MEA and the A220 alloy as determined by tensile tests.

In Figure 11 a) direct comparison of fracture surfaces between the two alloys for all tested microstructural states can be seen. Both as-received states (Figure 11 a) and e)) are very coarse-grained and both of them display a high elongation to failure and a very ductile fracture surface. After HPT processing both alloys, Figure 11 b) and f), show significant dimple-formation during fracture. The strongly reduced ductility during tensile testing after annealing at 500 °C for 1 h is also reflected in the fracture surfaces of both alloys – Figure 11 c) and g). Especially in the A220 alloy, Figure 11 c), the amount of dimples is strongly reduced, however their formation can still be observed. Fracture occurs with only little macroscopic plastic deformation and concentrates in a shear band leading to the elongated dimple shape. For the 800 °C, 1 h annealing state the CrCoNi alloy experiences significant grain growth, which also can be seen in Figure 11 h) due to dimples becoming gradually larger compared to the NC-states. During annealing a σ-phase is forming in the A220 alloy, which can be frequently observed in the corresponding fracture image in Figure 11 d) [45]. The fracture nonetheless occurs in a ductile fashion.

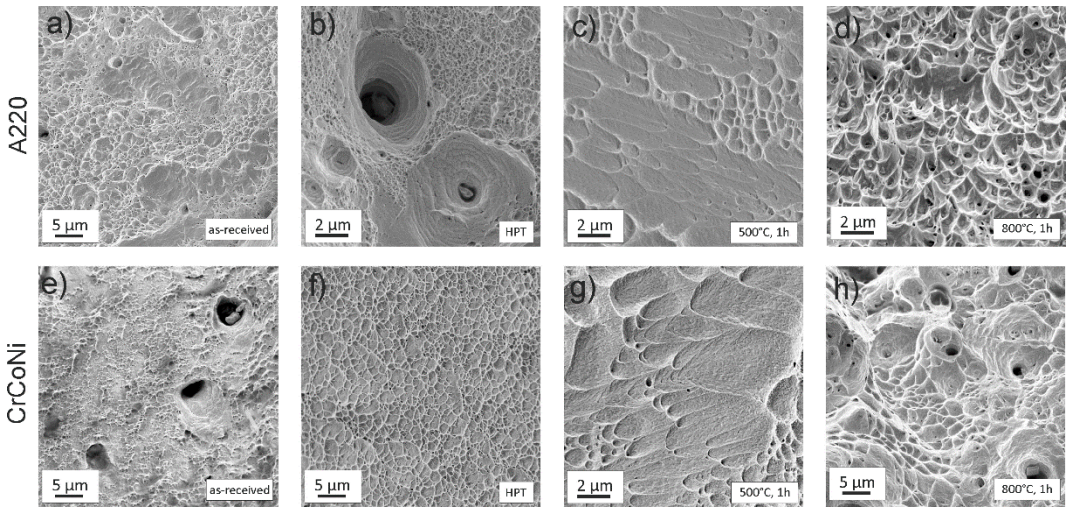

Figure 11: Fracture images of tensile tested samples, a)-d) of the A220 alloy. The as-received, a), and the HPT state, b), show highly ductile fracture features. After annealing at 500 °C, 1 h some dimples can still be found, however overall plasticity is quite limited. Despite the formation of σ-phase during 800 °C, 1 h annealing the fracture still occurs in a ductile fashion, with voids and dimples usually forming around this second phase. e)-h) Fractured samples of CrCoNi. The as-received state shows a highly ductile fracture surface, see e). f) Due to the high purity of the sample the overall fracture surface contains fewer voids, but is overall still dominated by dimple formation characteristic for a ductile fracture. The fracture mode remains a ductile one, even during annealing at 500 °C, 1 h, g) and 800 °C, 1 h, h).

A.4.4 Minority phase

Second phases in the CrCoNi alloy have been found in two further publications [26,46]. Moravcik et al. reported the formation of a second bcc phase almost entirely consisting of Cr at grain boundaries after compaction via spark plasma sintering and concluded this was a peculiarity of the processing route [26]. Another very recent study on a CrCoNi coating identified a second hcp-phase in the fcc matrix and surmised it was hcp Co due to a Co excess during deposition [46]. However, Co content in the alloy as measured by TEM-EDS was only off by approximately 3 at % from the equiatomic composition. It seems unlikely that the solubility limit of Co in the fcc-MEA matrix lies that close to the equiatomic composition and any excess of Co would lead to segregation of pure Co. Given the limited information on the minority phase an important clue on its nature can be found in Reference [47]]. Patriarca et al. reported for the CrMnFeCoNi alloy that the presence of Co atoms near stacking faults considerably decreased the energy of intrinsic stacking faults by over 50%. Overall, this could favour the segregation of Co to stacking faults and explain the minority phase in the CrCoNi alloy. A slight enrichment in Co could also explain the hcp nature of the minority phase, considering the fact that Co-rich phases tend to have a hcp character at lower temperatures.

The observation of the minority hcp phase in the present study is in strong contrast to what has been reported in other microstructural studies on the CrCoNi MEA so far [21,28,48]. The following discussion should point out several difficulties occurring in the identification of the phase, to highlight why the nature of the minority phase could not be entirely explained in this publication and to highlight its general elusiveness.

The presence of the phase could be seen in two different as-received material batches that had undergone long-term homogenization treatment and one batch of the same material that had additionally undergone cold-rolling and subsequent heat-treatment at 800 °C for 1h via TEM. In the last sample however no indication of the phase could be found via synchrotron XRD measurement, likely due to a lower volume fraction of this minority phase. This is pointing towards the fact that the occurrence of the phase might be strongly tied to processing conditions, especially the cooling rate during production and hence explain why it might not have been present in previous publications on materials with the same nominal composition.

The possibility that the occurrence of the minority phase in TEM is an artefact from TEM sample preparation can be excluded from two facts. First, it is retrievable in the present synchrotron-XRD data sampling a bulk specimen, second, because the TEM samples were produced with two different techniques (ion-polishing as well as electrochemical polishing) and the minority phase could be seen in both preparation techniques. Additionally, the phase is also not only present in surface/surface-near areas, which could be excluded from defocus series on TEM samples.

Identification of the phase via TEM bears difficulties given the faint nature of the Debye-Scherrer rings of the minority phase. Samples were investigated in two different TEMs (Philipps CM12 and JEOL 2100F) and only in the latter the minority phase could be seen in the diffraction images. The reason for that lies most likely in the difference in the sensitivity of the camera in both systems.

A.5 Conclusions

The equiatomic CrCoNi MEA was brought to a NC grain size regime and subsequently annealed in order to investigate its thermodynamic stability and the impact of heat treatments on the mechanical properties. Therefore, comprehensive investigations utilizing electron microscopy and synchrotron XRD measurements were performed. Additional mechanical tests in the form of tensile tests were performed to obtain insights into the microstructure-property relationships of the CrCoNi alloy. The results can be summarized as follows:

1. HPT-processing of the coarse-grained CrCoNi alloy results in a significant grain refinement down to a minimum grain size of approximately 50 nm and leads to a threefold increase in hardness.
2. The presence of a minority phase was found – For the 500°C, 200h annealing state it was determined to be a hcp phase. A possible reason for the formation of this phase is the favorable segregation of Co to stacking faults, leading to a decrease in stacking fault energy.
3. A direct comparison of 4 different microstructural states between the CrCoNi alloy and a commercial austenitic steel showed that the tensile properties of this medium-entropy alloy are competitive with currently used structural materials.

In summary, the presented results shed new light on the influence of grain refinement and subsequent annealing treatments on the microstructural stability and mechanical properties of the CrCoNi alloy. Especially the possibility of tailoring bi-modal grain size distribution as seen for some microstructural states (for instance 500 °C, 100 h) offers an excellent opportunity to further optimize the mechanical properties in future.

Acknowledgments: This work was supported by the Austrian Science Fund FWF in the framework of Research Project P26729-N19. The authors would like to thank Prof. Easo P. George for providing the material necessary to perform this study. Finally, the authors thank Christoph Gammer and Inas Issa for their help and the fruitful discussions.

Author Contributions: B. Schuh and A. Hohenwarter conceived and designed the experiments; B. Schuh, B. Völker, K.S. Kormout and N. Schell performed the experiments and analyzed the data; B. Schuh wrote the paper. All authors contributed substantially to the work reported.

Conflicts of Interest: The authors declare no conflict of interest.

A.6 References

[1] B. Cantor, I.T.H. Chang, P. Knight, A.J.B. Vincent, Microstructural development in equiatomic multicomponent alloys, Mater. Sci. Eng. A. 375–377 (2004) 213–218. doi:10.1016/j.msea.2003.10.257.

[2] J.W. Yeh, S.K. Chen, S.J. Lin, J.Y. Gan, T.S. Chin, T.T. Shun, C.H. Tsau, S.Y. Chang, Nanostructured high-entropy alloys with multiple principal elements: Novel alloy design concepts and outcomes, Adv. Eng. Mater. 6 (2004) 299–303. doi:10.1002/adem.200300567.

[3] F. Otto, A. Dlouhý, C. Somsen, H. Bei, G. Eggeler, E.P. George, The influences of temperature and microstructure on the tensile properties of a CoCrFeMnNi high-entropy alloy, Acta Mater. 61 (2013) 5743–5755. doi:10.1016/j.actamat.2013.06.018.

[4] G. Laplanche, O. Horst, F. Otto, G. Eggeler, E.P. George, Microstructural evolution of a CoCrFeMnNi high-entropy alloy after swaging and annealing, J. Alloys Compd. 647 (2015) 548–557. doi:10.1016/j.jallcom.2015.05.129.

[5] B. Gludovatz, E.P. George, R.O. Ritchie, Processing, Microstructure and Mechanical Properties of the CrMnFeCoNi High-Entropy Alloy, JOM 67 (2015) 2262–2270. doi:10.1007/s11837-015-1589-z.

[6] B. Gludovatz, A. Hohenwarter, D. Catoor, E.H. Chang, E.P. George, R.O. Ritchie, A fracture-resistant high-entropy alloy for cryogenic applications, Science 345 (2014) 1153–1158. doi:10.1126/science.1254581.

[7] N. Stepanov, M. Tikhonovsky, N. Yurchenko, D. Zyabkin, M. Klimova, S. Zherebtsov, A. Efimov, G. Salishchev, Effect of cryo-deformation on structure and properties of CoCrFeNiMn high-entropy alloy, Intermetallics 59 (2015) 8–17. doi:10.1016/j.intermet.2014.12.004.

[8] F. Zhang, Y. Wu, H. Lou, Z. Zeng, V.B. Prakapenka, E. Greenberg, Y. Ren, J. Yan, J.S. Okasinski, X. Liu, Y. Liu, Q. Zeng, Z. Lu, Polymorphism in a high-entropy alloy, Nat. Commun. 8 (2017) 1–7. doi:10.1038/ncomms15687.

[9] O. Schneeweiss, M. Friák, M. Dudová, D. Holec, M. Šob, D. Kriegner, V. Holý, P. Beran, E.P. George, J. Neugebauer, A. Dlouhý, Magnetic properties of the CrMnFeCoNi high-entropy alloy, Phys. Rev. B. 96 (2017) 1–13. doi:10.1103/PhysRevB.96.014437.

[10] S. Huang, W. Li, S. Lu, F. Tian, J. Shen, E. Holmström, L. Vitos, Temperature dependent stacking fault energy of FeCrCoNiMn high entropy alloy, Scr. Mater. 108 (2015) 44–47. doi:10.1016/j.scriptamat.2015.05.041.

[11] Z. Wu, M.C. Troparevsky, Y.F. Gao, J.R. Morris, G.M. Stocks, H. Bei, Phase stability, physical properties and strengthening mechanisms of concentrated solid solution alloys, Curr. Opin. Solid State Mater. Sci. 21 (2017) 267–284. doi:10.1016/j.cossms.2017.07.001.

[12] B. Schuh, F. Mendez-Martin, B. Völker, E.P. George, H. Clemens, R. Pippan, A. Hohenwarter, Mechanical properties, microstructure and thermal stability of a

nanocrystalline CoCrFeMnNi high-entropy alloy after severe plastic deformation, Acta Mater. 96 (2015) 258–268. doi:10.1016/j.actamat.2015.06.025.

[13] D.H. Lee, J.A. Lee, Y. Zhao, Z. Lu, J.Y. Suh, J.Y. Kim, U. Ramamurty, M. Kawasaki, T.G. Langdon, J. Il Jang, Annealing effect on plastic flow in nanocrystalline CoCrFeMnNi high-entropy alloy: A nanomechanical analysis, Acta Mater. 140 (2017) 443–451. doi:10.1016/j.actamat.2017.08.057.

[14] B. Schuh, B. Völker, J. Todt, N. Schell, L. Perrière, J. Li, J.P. Couzinié, A. Hohenwarter, Thermodynamic instability of a nanocrystalline, single-phase TiZrNbHfTa alloy and its impact on the mechanical properties, Acta Mater. 142 (2018) 201–212. doi:10.1016/j.actamat.2017.09.035.

[15] H. Shahmir, T. Mousavi, J. He, Z. Lu, M. Kawasaki, T.G. Langdon, Microstructure and properties of a CoCrFeNiMn high-entropy alloy processed by equal-channel angular pressing, Mater. Sci. Eng. A. 705 (2017) 411–419. doi:10.1016/j.msea.2017.08.083.

[16] V. Maier-Kiener, B. Schuh, E.P. George, H. Clemens, A. Hohenwarter, Insights into the deformation behavior of the CrMnFeCoNi high-entropy alloy revealed by elevated temperature nanoindentation, J. Mater. Res. 32 (2017) 2658–2667. doi:10.1557/jmr.2017.260.

[17] C.C. Koch, Nanocrystalline high-entropy alloys, J. Mater. Res. 32 (2017) 3435–3444. doi:10.1557/jmr.2017.341.

[18] E.J. Pickering, R. Muñoz-Moreno, H.J. Stone, N.G. Jones, Precipitation in the equiatomic high-entropy alloy CrMnFeCoNi, Scr. Mater. 113 (2016) 106–109. doi:10.1016/j.scriptamat.2015.10.025.

[19] F. Otto, A. Dlouhý, K.G. Pradeep, M. Kubênová, D. Raabe, G. Eggeler, E.P. George, Decomposition of the single-phase high-entropy alloy CrMnFeCoNi after prolonged anneals at intermediate temperatures, Acta Mater. 112 (2016) 40–52. doi:10.1016/j.actamat.2016.04.005.

[20] N.D. Stepanov, D.G. Shaysultanov, M.S. Ozerov, S.V. Zherebtsov, G.A. Salishchev, Second phase formation in the CoCrFeNiMn high entropy alloy after recrystallization annealing, Mater. Lett. 185 (2016) 1–4. doi:10.1016/j.matlet.2016.08.088.

[21] B. Gludovatz, A. Hohenwarter, K.V.S. Thurston, H. Bei, Z. Wu, E.P. George, R.O. Ritchie, Exceptional damage-tolerance of a medium-entropy alloy CrCoNi at cryogenic temperatures, Nat. Commun. 7 (2016) 1–8. doi:10.1038/ncomms10602.

[22] S. Yoshida, T. Bhattacharjee, Y. Bai, N. Tsuji, Friction stress and Hall-Petch relationship in CoCrNi equi-atomic medium entropy alloy processed by severe plastic deformation and subsequent annealing, Scr. Mater. 134 (2017) 33–36. doi:10.1016/j.scriptamat.2017.02.042.

[23] Y.L. Zhao, T. Yang, Y. Tong, J. Wang, J.H. Luan, Z.B. Jiao, D. Chen, Y. Yang, A. Hu, C.T. Liu, J.J. Kai, Heterogeneous precipitation behavior and stacking-fault-mediated deformation in a CoCrNi-based medium-entropy alloy, Acta Mater. 138 (2017) 72–82. doi:10.1016/j.actamat.2017.07.029.

[24] G. Laplanche, A. Kostka, C. Reinhart, J. Hunfeld, G. Eggeler, E.P. George, Reasons for the superior mechanical properties of medium-entropy CrCoNi compared to high-entropy CrMnFeCoNi, Acta Mater. 128 (2017) 292–303. doi:10.1016/j.actamat.2017.02.036.

[25] F.X. Zhang, S. Zhao, K. Jin, H. Xue, G. Velisa, H. Bei, R. Huang, J.Y.P. Ko, D.C. Pagan, J.C. Neuefeind, W.J. Weber, Y. Zhang, Local Structure and Short-Range Order in a NiCoCr Solid Solution Alloy, Phys. Rev. Lett. 118 (2017) 1–6. doi:10.1103/PhysRevLett.118.205501.

[26] I. Moravcik, J. Cizek, Z. Kovacova, J. Nejezchlebova, M. Kitzmantel, E. Neubauer, I. Kubena, V. Hornik, I. Dlouhy, Mechanical and microstructural characterization of powder metallurgy CoCrNi medium entropy alloy, Mater. Sci. Eng. A. 701 (2017) 370–380. doi:10.1016/j.msea.2017.06.086.

[27] Z. Zhang, H. Sheng, Z. Wang, B. Gludovatz, Z. Zhang, E.P. George, Q. Yu, S.X. Mao, R.O. Ritchie, Dislocation mechanisms and 3D twin architectures generate exceptional strength-ductility-toughness combination in CrCoNi medium-entropy alloy, Nat. Commun. 8 (2017) 1–8. doi:10.1038/ncomms14390.

[28] Z. Wu, H. Bei, F. Otto, G.M. Pharr, E.P. George, Recovery, recrystallization, grain growth and phase stability of a family of FCC-structured multi-component equiatomic solid solution alloys, Intermetallics 46 (2014) 131–140. doi:10.1016/j.intermet.2013.10.024.

[29] R. Pippan, S. Scheriau, A. Taylor, M. Hafok, A. Hohenwarter, A. Bachmaier, Saturation of fragmentation during severe plastic deformation, Annu. Rev. Mater. Res. 40 (2010) 319–343. doi:10.1146/annurev-matsci-070909-104445.

[30] MathWorks, MatLab, (2017). https://de.mathworks.com/.

[31] G.B. Rathmayr, A. Bachmaier, R. Pippan, Development of a new testing procedure for performing tensile tests on specimens with sub-millimetre dimensions, J. Test. Eval. 41 (2013) 1–12. doi:10.1520/JTE20120175.

[32] A.P. Hammersley, S.O. Svensson, M. Hanfland, A.N. Fitch, D. Hausermann, Two-dimensional detector software: From real detector to idealised image or two-theta scan, High Press. Res. 14 (1996) 235–248. doi:10.1080/08957959608201408.

[33] CrystalImpact ; http://www.crystalimpact.com/, Match! Phase Identification from Powder Diffraction, (2016). http://www.crystalimpact.com/.

[34] X. Sauvage, G. Wilde, S. V. Divinski, Z. Horita, R.Z. Valiev, Grain boundaries in ultrafine grained materials processed by severe plastic deformation and related phenomena, Mater. Sci. Eng. A. 540 (2012) 1–12. doi:10.1016/j.msea.2012.01.080.

[35] R.Z. Valiev, R.K. Islamgaliev, I. V. Alexandrov, Bulk nanostructured materials from severe plastic deformation, Prog Mater Sci. 45 (2000) 103-189. doi:10.1016/S0079-6425(99)00007-9.

[36] Z.J. Zhang, M.M. Mao, J. Wang, B. Gludovatz, Z. Zhang, S.X. Mao, E.P. George, Q. Yu, R.O. Ritchie, Nanoscale origins of the damage tolerance of the high-entropy alloy CrMnFeCoNi, Nat. Commun. 6 (2015) 1–6. doi:10.1038/ncomms10143.

[37] S. Scheriau, Z. Zhang, S. Kleber, R. Pippan, Deformation mechanisms of a modified 316L austenitic steel subjected to high pressure torsion, Mater. Sci. Eng. A. 528 (2011) 2776–2786. doi:10.1016/j.msea.2010.12.023.

[38] J. Miao, C.E. Slone, T.M. Smith, C. Niu, H. Bei, M. Ghazisaeidi, G.M.M. Pharr, M.J. Mills, The evolution of the deformation substructure in a Ni-Co-Cr equiatomic solid solution alloy, Acta Mater. 132 (2017) 35–48. doi:10.1016/j.actamat.2017.04.033.

[39] O. Renk, A. Hohenwarter, K. Eder, K.S. Kormout, J.M. Cairney, R. Pippan, Increasing the strength of nanocrystalline steels by annealing: Is segregation necessary?, Scr. Mater. 95 (2015) 27–30. doi:10.1016/j.scriptamat.2014.09.023.

[40] X. Huang, N. Hansen, N. Tsuji, Hardening by Annealing and Softening by Deformation in Nanostructured Metals, Science 312 (2006) 249–251. doi:10.1126/science.1124268.

[41] E. Ma, T.D. Shen, X.L. Wu, Nanostructured metals: less is more., Nat. Mater. 5 (2006) 515–516. doi:10.1038/nmat1671.

[42] O. Renk, A. Hohenwarter, B. Schuh, J.H. Li, R. Pippan, Hardening by annealing: Insights from different alloys, IOP Conf. Ser. Mater. Sci. Eng. 89 (2015) 1–7. doi:10.1088/1757-899X/89/1/012043.

[43] R.Z. Valiev, N.A. Enikeev, M.Y. Murashkin, V.U. Kazykhanov, X. Sauvage, On the origin of the extremely high strength of ultrafine-grained Al alloys produced by severe plastic deformation, Scr. Mater. 63 (2010) 949–952. doi:10.1016/j.scriptamat.2010.07.014.

[44] X. Tong, H. Zhang, D.Y. Li, Effect of Annealing Treatment on Mechanical Properties of Nanocrystalline α-iron: An Atomistic Study, Sci. Rep. 5 (2015) 8459 (1–7). doi:10.1038/srep08459.

[45] C.-C. Hsieh, W. Wu, Overview of Intermetallic Sigma Phase Precipitation in Stainless Steels, ISRN Metall. 2012 (2012) 1–16. doi:10.5402/2012/732471.

[46] F. Cao, P. Munroe, Z. Zhou, Z. Xie, Medium entropy alloy CoCrNi coatings: Enhancing hardness and damage-tolerance through a nanotwinned structuring, Surf. Coatings Technol. 335 (2018) 257–264. doi:10.1016/j.surfcoat.2017.12.021.

[47] L. Patriarca, A. Ojha, H. Sehitoglu, Y.I. Chumlyakov, Slip nucleation in single crystal FeNiCoCrMn high entropy alloy, Scr. Mater. 112 (2016) 54–57. doi:10.1016/j.scriptamat.2015.09.009.

[48] Z. Wu, H. Bei, G.M. Pharr, E.P. George, Temperature dependence of the mechanical properties of equiatomic solid solution alloys with face-centered cubic crystal structures, Acta Mater. 81 (2014) 428–441. doi:10.1016/j.actamat.2014.08.026.

B.

Tailoring bimodal grain size structures in nanocrystalline compositionally complex alloys to improve ductility

B. Schuh [a,b], R. Pippan [a], A. Hohenwarter [b]

[a] Erich-Schmid-Institute of Materials Science, Austrian Academy of Sciences, Jahnstraße 12, 8700 Leoben, Austria

[b] Department of Materials Physics, University of Leoben, Jahnstraße 12, 8700 Leoben, Austria

Abstract

The feasibility of engineering bimodal grain size distributions to achieve superior mechanical properties was explored in two face-centered cubic compositionally complex alloys, namely CrMnFeCoNi and its high-performance subvariant CrCoNi. Therefore, both alloys were processed down to the nanocrystalline grain size regime by utilizing high-pressure torsion and subsequently annealed at intermediate temperatures. Especially the CrCoNi alloy is prone to formation of bimodal microstructures and for an annealing treatment at 500 °C for 100 h an excellent combination of ultra-high tensile strength, exceeding 1500 MPa, and decent ductility with elongations to failure of 10 % could be achieved.

B.1 Introduction

High-entropy alloys (HEAs) and compositionally complex alloys are a new class of multi-component metallic materials that have shown outstanding properties, sometimes surpassing conventional alloys and therefore sparking huge interest in the research community [1–6]. Among the most promising candidates are two face-centered-cubic (fcc) alloys with equiatomic compositions, CrMnFeCoNi and CrCoNi. Both alloys exhibit excellent mechanical properties [1,2,7–9], especially at cryogenic temperatures showing high ductility and fracture toughness, as well as yield strengths comparable to many TWIP steels [10,11]. In recent years extensive research has gone into further improving the mechanical strength of these fcc HEAs [12–15]. One feasible approach is granted by extensive grain-refinement, for example achieved by high-pressure torsion (HPT) which commonly produces high-strength materials [16–20]. However, a majority of nanocrystalline (NC) materials, irrespective of the used synthesis process, suffer from a fundamental problem – limited ductility. According to Ma et al. ductility in NC materials is heavily influenced by two aspects [21]: I) A tendency towards a cracking instability/brittle failure, often influenced by sample quality. II) Excessive localized deformation and plastic instabilities due to a low capacity for strain hardening leading to low uniform elongations in uniaxial tensile tests.

Several strategies have been proposed to counteract the problem of low uniform elongation during tensile testing in NC materials, which otherwise could hinder the practical application of such materials in future. The common denominator of these strategies is to raise the low strain hardening rate and therefore delay the onset of necking [22–24]. One straight-forward approach are heat treatments in order to achieve a slightly larger grain size – However, this often results in a considerable loss of strength to gain ductility ("strength-ductility trade off"). Another idea, to achieve better ductility and high strength at the same time, is to tailor a bimodal grain size distribution [22–25]. An example of this can be found in Reference [26]. Wang et al. could impressively increase the strength of coarse-grained copper specimens while retaining elongations to failure of more than 60 %, by combining ultrafine grains with a volume fraction of about 25 % of larger grains. These results could partly be attributed to the fact that larger grains preferentially accommodate strain. Another aspect is that the confined grains are under a complex stress state, which is beneficial for dislocation storage and hence strain hardening. Since the CrCoNi alloy is prone to abnormal grain growth the tailoring of such bi- or multi-modal microstructures can be achieved by annealing treatments after HPT processing [27]. In order to explore if the bimodal grain size distribution approach for ductility enhancement in NC compositionally complex alloys is a feasible approach, the present study was initiated. In the center of interest was the aforementioned ternary equiatomic CrCoNi alloy as well as the CrMnFeCoNi alloy for comparative purposes.

B.2 Material and Methods

Both materials were produced from high-purity elements using arc melting and drop casting into copper molds and afterwards subjected to a 24 h to 48 h homogenization treatment at 1200 °C. The ingots were then cold forged and cross rolled with a thickness reduction of approximately 60 % at room temperature and subsequently subjected to an annealing treatment at 800 °C for 1 h – for processing details see [1,2,8]. Disks of 8 mm in diameter and 0.8 mm in thickness were machined out of the ingots and deformed via quasi-constrained HPT. 5 rotations were applied for each disk at room-temperature with a pressure of 7.8 GPa. This led to a saturation in grain size within large parts of the disk with

a steady state grain size of about 50 nm in both materials [27,28]. Subsequently, both alloys underwent heat treatments at intermediate temperatures in order to achieve bimodal grain size distributions. Microstructural as well as fractographic investigations were performed utilizing a scanning electron microscope (SEM, Zeiss 1525) equipped with an Electron Back Scatter Diffraction (EBSD) system form EDAX. In the bimodal structures the grain size of the coarse-grains (CGs) was determined by EBSD-measurements. For analysis, only data points with a confidence index higher than 0.1 were considered. High angle grain boundaries were defined as having a minimum misorientation of 15° and Σ3 recrystallization twins were excluded from the analysis.

In order to evaluate the tensile properties at least 3 samples per microstructural state were tested. Two samples were prepared from each HPT disk with the gauge length of the tensile sample located at a radius of 2 mm and therefore well within the microstructural homogenous saturation area of the HPT disk. Tests then were performed utilizing a tensile testing machine from Kammrath and Weiss, at room temperature with a 2 kN load cell and a cross head speed of 2.5 µm/s. For data analysis a MatLab [29] software package was used for automated digital image correlation. All further details on specimen production, testing and data evaluation can be found elsewhere [30].

B.3 Results and discussion

B.3.1 Investigated microstructures

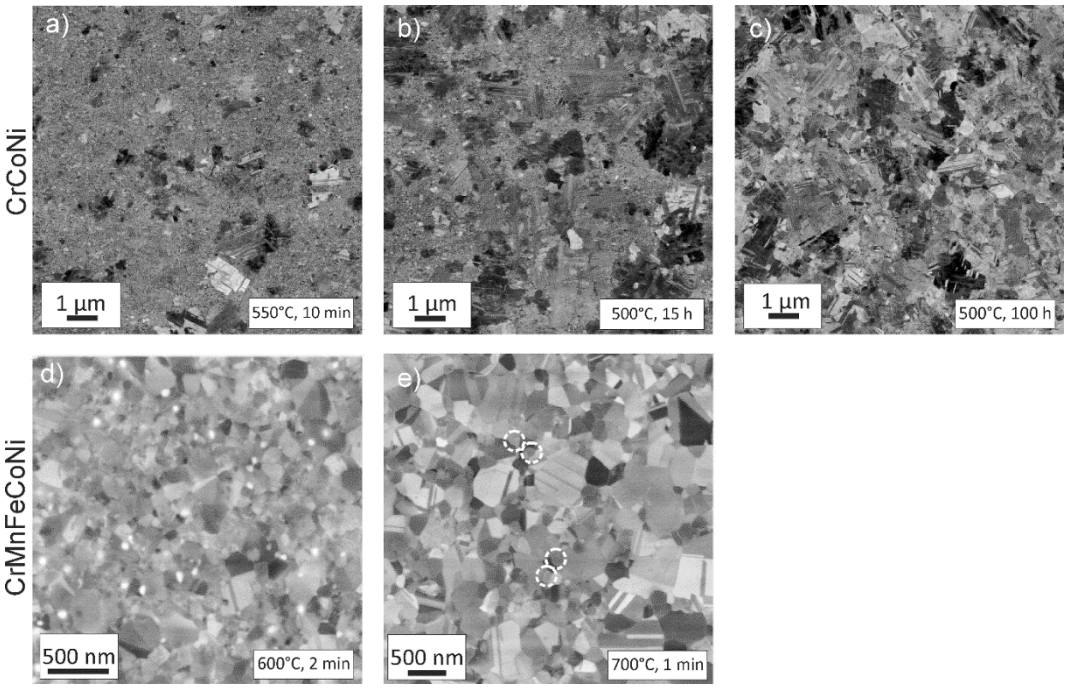

Figure 1: Back-scattered electron images of the microstructures after annealing treatments of the CrCoNi alloy, a) to c), and the CrMnFeCoNi alloy, d) and e). a) An annealing treatment at 550 °C for 10 min leads to a small fraction of coarse grains (CGs) embedded in a NC grain matrix. b) 15 h of annealing at 500 °C increases the fraction of CGs and CG regions start to coalesce. c) At 500 °C, 100 h only small islands of NC grains remain. For both microstructural states of the CrMnFeCoNi alloy d) and e) the formation of second phases can be observed, in e) they are marked by white

circles due to their poor visibility. While a 600 °C, 2 min heat treatment leads to a pronounced bimodal grain size distribution, at 700 °C for 1 min the microstructure is already quite homogenous.

In the CrCoNi alloy 3 different bimodal grain size distribution were achieved via annealing treatments, see Figure 1 a)-c). In Figure 1 a) it can be seen that an annealing treatment at 550 °C for 10 min resulted in a microstructure consisting of a volume fraction of coarse grains (CGs) of 10-20 %, which are relatively homogenously embedded in the NC- matrix. Heat treatments at 500 °C for 15 h on the other hand produced a microstructure that consisted of about 70-80 % of CGs, see Figure 1 b). Lastly, at 500 °C for 100 h a microstructure consisting predominantly of CGs with small islands of NC grains in between was achieved, Figure 1 c). Obtaining bi- or multimodal grain size distributions via annealing in the CrMnFeCoNi alloy on the other hand is experimentally more challenging due to its phase instability at intermediate annealing temperatures [28,31–33]. The CrMnFeCoNi alloy only remains a single-phase alloy for annealing temperatures of approximately higher than 800 °C, however pre-experiments showed that at such elevated temperatures even short time anneals (in the range of minutes) led to fully recrystallized, homogenous microstructures. Thus, tailoring bimodal grain size distributions can only be attempted in the temperature range where second phases are formed upon annealing as well. In Figure 1d) it can be seen that an annealing treatment at 600 °C for 2 min resulted in a very low fraction of CG as well as precipitation of second phases. At 700 °C it is already difficult to achieve bimodal grain size distributions, the fcc-matrix is homogenous and the bimodality is only caused by the precipitation of smaller second phase particles at the grain boundaries. According to the literature the second phases that are formed both at 600 °C and 700 °C should be a Cr-rich tetragonal σ-phase, while additionally at 600 °C a Cr-rich bcc phase can sometimes be found as well [31,33,34]. In Table 1 a brief summary of the volume fraction of the CG portion ($f_{V,CG}$) and the approximate size of the NC grains as well as of the CGs is given.

	Sample	$f_{V,CG\ (\%)}$	CG	NC
CrCoNi	550°C, 10min	10 - 20	1.2 ± 0.4 µm	< 100 nm
	500°C, 15h	70 - 80	1.8 ± 0.6 µm	< 100 nm
	500°C, 100h	90 - 100	2.0 ± 0.5 µm	< 100 nm
CrMnFeCoNi	600°C, 2min	< 5	< 300 nm	< 100 nm
	700°C, 1min	No bimodality - Grain size of ~400 nm		

Table 1: Summary of microstructural parameters, $f_{V,CG}$ is the volume fraction of CGs.

B.3.2 Correlation between microstructure and mechanical response

Representative stress-strain curves obtained from tensile testing can be found in Figure 2 for the CrCoNi alloy and in Figure 3 for the CrMnFeCoNi alloy. All mechanical properties are summarized in Table 2, where also the reduction of area as an additional measure of ductility was added. In Figure 2 and 3 as well as Table 2 the mechanical properties of the HPT deformed states as well as a CG states, with an average grain size of 5-6 µm for both alloys, were added. More information on the mechanical properties as well as the microstructure of these samples can be found in References [1,2,27,28].

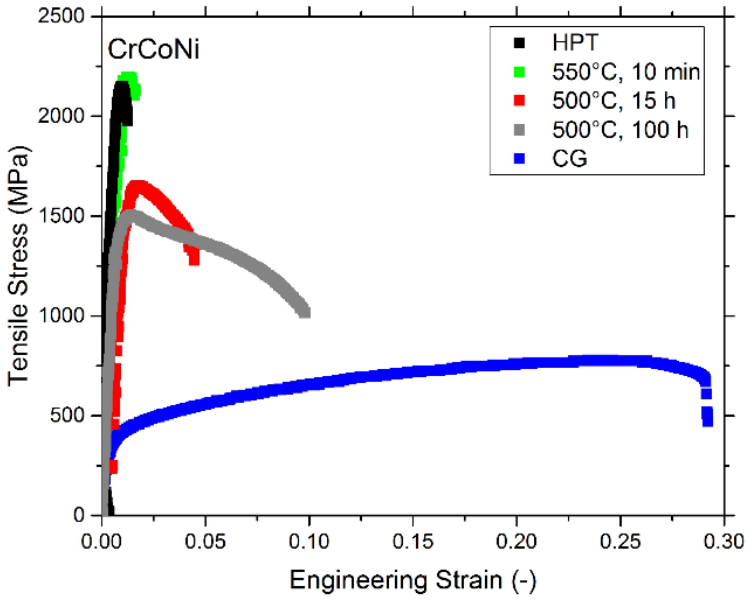

Figure 2: Representative tensile stress-strain curves of different microstructural states of the CrCoNi alloy.

In the 550 °C, 10 min sample the increase in ultimate tensile strength (UTS) from approximately 2070 MPa for the HPT processed state to about 2170 MPa for the heat treated state is also accompanied by a decrease in tensile ductility. The total elongation to failure is already low for the HPT processed samples, about 4 %, and after the heat treatment the total elongation to failure is only 1.4 %, with some samples even fracturing in the elastic regime of the test. The fraction of CGs to NC grains is much higher in the 500 °C, 15 h state, as can be seen in Figure 1 b), leading to significantly different mechanical behavior. The UTS is reduced to approximately 1616 MPa, the elongation to failure is increased, about 5.2 %. A further increase in the fraction of CG, as seen for an annealing treatment at 500 °C for 100 h (Figure 1 c)) leads to a small decrease in UTS, however, the tensile ductility almost doubles and reaches values of 10 %. In brief, two microstructural states show an improved ductility compared to the HPT processed state. However, this increase in tensile ductility is mostly owed to a much more pronounced non-uniform elongation, since in all bimodal samples necking still occurs at considerably low values of uniform elongation in direct comparison with the full NC-state (HPT-deformed).

While plenty of reports of the beneficial nature of bi- or multi-modal microstructures regarding the mechanical properties exist in the literature, the influence of

many microstructural parameters, such as ratio of large to small grains, grain shape and distribution is still controversially discussed [26,35–37]. An in-depth study on bimodal Cu revealed that both yield strength and uniform elongation follow the rule-of-mixtures [36], which can be supported by simulation and modelling approaches [38,39]. However, Zhao et al. also noted that both, positive and negative deviations from the rule-of-mixtures, are frequently reported, which may be attributed to size-ratio differences between small and large grains but also the spatial distribution [36]. For instance, Wang et al. [26] reported a strength-ductility combination much superior to what is suggested by the rule-of-mixtures at a volume fraction of CG of about 25%. Another study on bimodal aluminum alloys on the other hand shows diminishing returns when increasing the fraction of CG beyond a certain point – This was explained by the fact that when a certain threshold volume fraction of CG areas is reached, where they start to coalesce, their ability to act as crack arrestors saturates [40].

Ideally, in bimodal structures the largest grains are constrained by the surrounding finer grains and yield first during loading. As the load further rises, the stress concentration caused by dislocation pile-ups in the CGs increases as well, until a critical value is reached and slip systems in the NC grains are activated, causing a load transfer between the CG/NC interface and plastic deformation in the NC grains [41]. Hence, while the mechanical behavior of bimodal structures is often only discussed with respect to the significance of the CG volume fraction, it is clear that grain size has an equally important impact. In consideration how bimodal structures are deforming, the further decrease in yield strength observed between the CrCoNi systems for the annealing states of 500 °C for 15 h and 100 h should therefore primarily be caused by the difference in their CG sizes and not the difference in their volume fractions. This is substantiated by the findings of Magee et al. who reported a saturation effect of the CG volume fraction in the yield strength dependency once the CG areas start to coalesce. Transferred to the current case, this means that the further increase in CG volume fraction between the 500 °C for 15 h and 100 h annealing state would no longer lead to a significant change in strength, since even in the 15 h state CG regions are already strongly interconnected [40].

The reason for the observed phenomena in the 550 °C, 10 min, where higher mechanical strengths are achieved despite the presence of CG cannot yet be fully explained and future investigations are needed. The main cause most likely lies in the strong intersection of CG by recrystallization twins, leading to significantly smaller substructures than the overall grain size suggests and additional strengthening could be provided by a "hardening by annealing" phenomena frequently observed in NC metals [42,43] including the CrCoNi and the CrMnFeCoNi alloy [27,28]. The cause of such "hardening by annealing" phenomena are still controversially discussed in the literature, but they seem to be linked to a certain threshold grain size [43]. A popular explanation is that annealing treatment of NC structures lead to a rapid dislocation annihilation at the readily available grain boundaries, which results in a depletion of mobile dislocations in the grain interior. If subsequently plastic deformation is to be realized, dislocation emission from grain boundary sources is necessary. However, according to Ma et al. such an annealing treatment should also cause a relaxation of the grain boundaries, which makes dislocation emission more difficult [44]. Another explanation for the phenomena might be related to grain boundary segregation and a more difficult dislocation emission caused by solute-drag effects [45].

Besides distinctive changes in the strength levels of the differently heat-treated CrCoNi samples, the ductility is clearly affected as well. Focusing only on the uniform elongation, the samples with bimodal microstructures show relatively low values compared to the CG reference state with grain sizes around 6 μm. This is a result of a low strain

hardening rate which leads to a quick damage localization. This low strain hardening rate despite the presence of CG likely originates from the fact that mechanical twinning is not be very pronounced in the CG regions of the bimodal structures with grain sizes around 1 µm (see Table 1). In low stacking fault energy (SFE) metals, such as both, the CrCoNi and CrMnFeCoNi alloy, the twinning propensity is strongly dependent on the grain size [46]. This is well exemplified by a study on a MP35N (35 % Co 35 % Ni 20 % Cr 10 % Mo) alloy, where a high twin density was observed in microstructures with a grain size of about 40 µm but no twinning at all for an average grain size of 1 µm [46]. Another example proving that bimodal microstructures do not necessarily lead to beneficial properties is given by another low SFE alloy, 316L steel [47]. Given the average grain size of the CG in the CrCoNi alloy in this investigation (in the range of 1 micron), it is reasonable to assume that the propensity for mechanical twinning and hence the strain hardening rate is strongly reduced in comparison to studies performed on coarser-grained CrCoNi samples (grain-size ~ 6µm) [2]. While the strain hardening rate is too low to sustain uniform elongation, the larger substructures in the CG still provide better capabilities for dislocation storage compared to the NC state, which is one factor leading to an improved non-uniform elongation and area reduction especially observed in the 500 °C, 100 h annealing state. In addition, the damage accumulation is postponed by the CG-fraction as it can be partly inferred from fractographic investigation (see later).

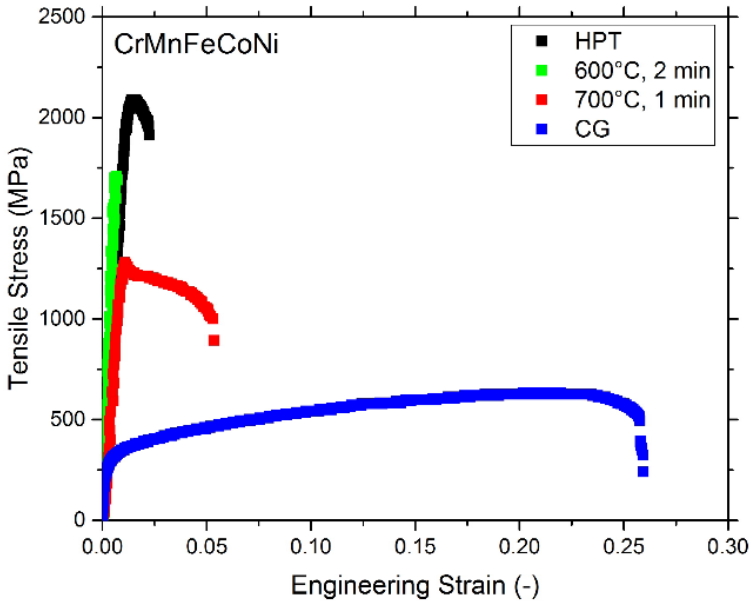

Figure 3: Representative tensile stress-strain curves of different microstructural states of the CrMnFeCoNi alloy.

The results of the annealing treatments of the CrMnFeCoNi alloy are presented in Figure 3. After annealing, samples at 600 °C for 2 min usually fail prematurely in the elastic regime of the tensile test, similarly to what has been reported in the literature for 1 h annealed samples [28]. However, for the 700 °C, 1 min heat treatment, some ductility is restored at the cost of a considerable loss of strength. Due to the thermodynamic instability of the alloy, the formation of additional phases during heat-treatments is unavoidable. Therefore, the results for the 600 °C state shows a deterioration of the deformation behavior compared to the HPT-state. Only for the 700 °C an improvement in ductility was found, as the presence of second phase particles is strongly reduced, Figure 1 e). The negative effect

of additional phases could be possibly circumvented by using other processing routes which could have the potential to achieve bimodal microstructures without the formation of the second phases, for instance via consolidation of both CG and NC powder blends [41,48,49]. Additionally, another way to achieve excellent strength-ductility combinations in homogenous single-phase materials was demonstrated recently. Tian et al. [50] subjected HPT-processed Cu to post annealing treatments and while for grain sizes of approximately 300 nm a yield drop phenomena and a quick damage localization and subsequent failure was observed, for slightly larger grains of about 500 nm excellent mechanical properties were reported. The main difference is that while the 500 nm microstructural state also showed a yield drop phenomenon, the strain hardening capability is high enough, so that the Lüders band can propagate throughout the material, leading to a very large Lüders strain. Similarly, the 700 °C, 1 min CrCoFeMnNi alloy also shows a yield drop phenomenon, see Figure 3. Hence, it would be interesting to attempt if such an extensive Lüders strain could be reached in the CrCoFeMnNi alloy by tailoring slightly larger grain sizes as well.

Microstructural State		Ultimate Tensile Strength (MPa)	Elongation to Failure (%)	Yield Strength $\sigma_{0.2}$ (MPa)	Area Reduction (%)
CrCoNi	CG	784 ± 42	30 ± 2	402 ± 21	84 ± 11
	HPT	2067 ± 153	3.9 ± 1.5	1901 ± 114	22 ± 8
	550°C, 10 min	2170 ± 98	1.4 ± 0.3	*	*
	500°C, 15 h	1616 ± 38	5.2 ± 0.2	1530 ± 83	46 ± 13
	500°C, 100 h	1520 ± 15	10 ± 0.2	1452 ± 35	58 ± 2
CrMnFeCoNi	CG	641 ± 10	25 ± 2	329 ± 30	76 ± 6
	HPT	1924 ± 124	3.2 ± 1.3	1787 ± 200	30 ± 13
	600°C, 2 min	1669 ± 266	1.5 ± 0.3	*	*
	700 °C, 1 min	1216 ± 148	5.4 ± 1.5	1207 ± 151	53 ± 5

*Not all specimens yielded before fracture

Table 2: Summarized mechanical properties of the tested microstructural states of the CrCoNi and CrMnFeCoNi alloy.

B.3.3 Fractography

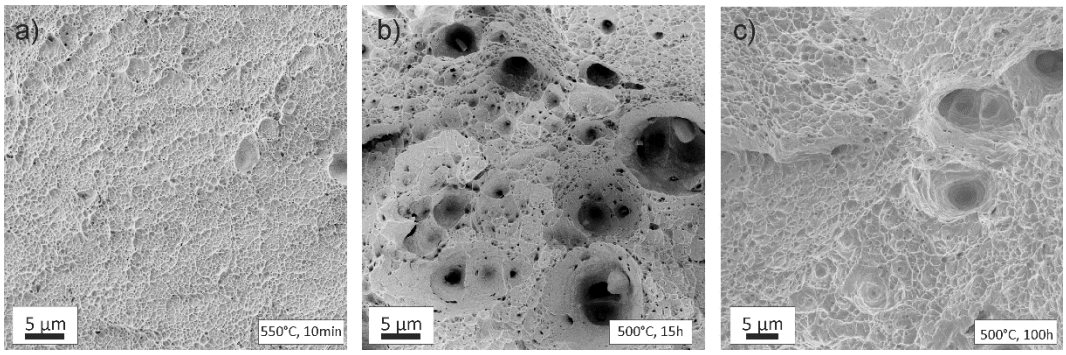

Figure 4: In a) to c) the fracture images of CrCoNi tensile samples annealed at 550 °C for 10 min and at 500 °C for 15 h and 100 h can be seen. All of them feature a ductile fracture surface with dimple formation.

In Figure 4 a) to c) representative fracture images of the CrCoNi alloy annealed at 550 °C for 10 min and at 500 °C for 15 h and 100 h, respectively, can be seen. Despite the fact that all microstructural states show ductile fractures with dimple formation the amount of ductility is very different. In detail, especially in b) and c) large and deep dimples formed around intermetallic inclusions can be observed. From microstructurally uniform samples it is known that the failure mechanism typical for CG-structures involves the void initiation and formation from inclusions leading to these pronounced deep dimples during failure as presented in Figure 4 b) (macrodimples). In NC-materials void formation is controlled by triple junctions and grain boundaries acting as initiation points leading to shallow dimples in the range of the grain size or somewhat larger (micro- or nano-dimples) [51]. As especially Figure 4 b) shows, the final fracture of the sample is controlled by the coalescence of the macrovoids forming large and deep dimples stemming from the CG-fraction. This requires more plastic deformation than the formation of the micro/nanovoids and delays final failure of the sample. As a result, while the as processed and 550 °C, 10 min sample fractures with little macroscopic plasticity, the 500 °C, 15 h and 100 h sample with high CG-fractions show much higher values for the elongation to fracture. On the macroscopic level for the brittle case (550 °C, 10 min) shear fracture is typical, whereas in the more ductile case (500 °C, 15 h and 100 h) a cup-and-cone fracture prevails, see Figure 5.

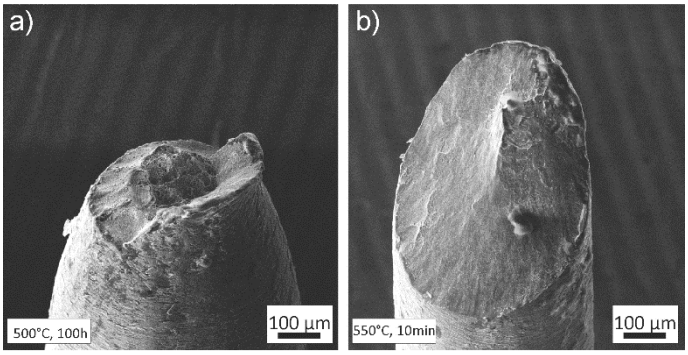

Figure 5: Macroscopic fracture images of the CrCoNi alloy. a) shows the ductile 500 °C, 100 h annealing state with a cup-and-cone fracture, a). b) Flat shear fracture of the 500 °C, 10 min annealed samples.

Figure 6 is depicting SEM fractographs of the CrMnFeCoNi alloy that underwent annealing treatments at 600 °C for 2 min, a), and 700 °C for 1 min, b). Despite the precipitation of brittle second phases mainly on the grain boundaries, both materials fail at first sight again in a ductile fracture mode with dimple formation. In Figure 6 a) the dimples are small and shallow, whereas in Figure 6 b) it can be clearly observed that dimples form around the second phase precipitates that are larger and therefore consume considerably more plastic deformation, which is also well reflected when comparing the maximum elongation before failure between the two annealing states. Since the number of the precipitates is very large compared to the CoCrNi-alloy after 100 h heat-treatments, they coalesce earlier and lead to a lower total elongation before failure. The macroscopic behavior is the same as in the CrCoNi alloy: In the brittle case (600 °C, 2min), shear fracture occurs whereas in the more ductile specimen (700 °C, 1min) a cup and cone fracture was found.

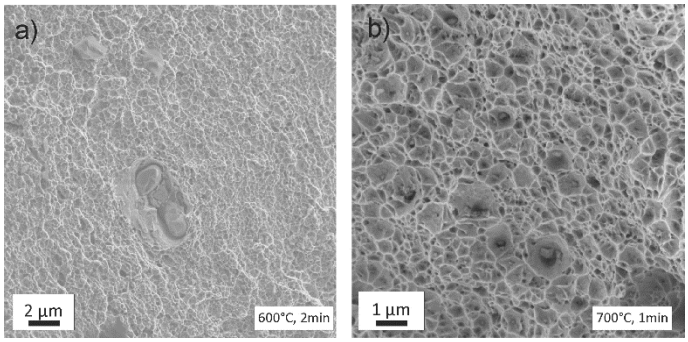

Figure 6: Despite the formation of second phases during annealing (600 °C, 2 min in a) and 700 °C, 1 min in b)) of the CrMnFeCoNi alloy the fracture mode remains ductile. In b) the dimple formation around these second phases can be observed.

B.4 Conclusions

In this study bimodal grain size distributions were induced via heat-treatments in two nanocrystalline compositionally complex alloys, CrMnFeCoNi and CrCoNi, with the aim to enhance their ductility. In case of the CrMnFeCoNi alloy, it was found that the bimodal grain size distribution is experimentally very challenging to achieve due to the thermodynamic instability of the alloy, leading to multiphase structures with embrittling phases in a large temperature window. Therefore, the combination of SPD-processing and annealing does not seem to be a feasible way to achieve supreme tensile properties in this alloy.

In contrast, in the CrCoNi alloy a twofold increase in ductility was achieved via grain size engineering. Further optimization of the heat treatment might yield microstructural states with both high tensile strength and a high strain hardening rate so that uniform elongation can be sustained for large strains during deformation. A feasible way to achieve this might be by increasing the size of the CG grains. While this could provoke somewhat lower yield strengths, larger grains should promote a better strain hardening rate through a higher mechanical twinning propensity.

This work was supported by the Austrian Science Fund FWF in the framework of Research Project P26729-N19. Funding of this work has also been provided by the European Research Council under ERC Grant Agreement No. 340185 USMS. The authors would like to thank Prof. Easo P. George for providing the material necessary to perform this study.

B.5 References

[1] B. Gludovatz, A. Hohenwarter, D. Catoor, E.H. Chang, E.P. George, R.O. Ritchie, A fracture-resistant high-entropy alloy for cryogenic applications, Science 345 (2014) 1153–1158. doi:10.1126/science.1254581.

[2] B. Gludovatz, A. Hohenwarter, K.V.S. Thurston, H. Bei, Z. Wu, E.P. George, R.O. Ritchie, Exceptional damage-tolerance of a medium-entropy alloy CrCoNi at cryogenic temperatures, Nat. Commun. 7 (2016) 10602. doi:10.1038/ncomms10602.

[3] D.B. Miracle, O.N. Senkov, A critical review of high entropy alloys and related concepts, Acta Mater. 122 (2017) 448–511. doi:10.1016/j.actamat.2016.08.081.

[4] Y. Zhang, T.T. Zuo, Z. Tang, M.C. Gao, K.A. Dahmen, P.K. Liaw, Z.P. Lu, Microstructures and properties of high-entropy alloys, Prog. Mater. Sci. 61 (2014) 1–93. doi:10.1016/j.pmatsci.2013.10.001.

[5] O.N. Senkov, G.B. Wilks, D.B. Miracle, C.P. Chuang, P.K. Liaw, Refractory high-entropy alloys, Intermetallics 18 (2010) 1758–1765. doi:10.1016/j.intermet.2010.05.014.

[6] J.P. Couzinié, G. Dirras, Body-centered cubic high-entropy alloys: From processing to underlying deformation mechanisms, Mater. Charact. (2018) In Press. doi:10.1016/J.MATCHAR.2018.07.015.

[7] B. Gludovatz, E.P. George, R.O. Ritchie, Processing, Microstructure and Mechanical Properties of the CrMnFeCoNi High-Entropy Alloy, JOM 67 (2015) 2262–2270. doi:10.1007/s11837-015-1589-z.

[8] F. Otto, A. Dlouhý, C. Somsen, H. Bei, G. Eggeler, E.P. George, The influences of temperature and microstructure on the tensile properties of a CoCrFeMnNi high-entropy alloy, Acta Mater. 61 (2013) 5743–5755. doi:10.1016/j.actamat.2013.06.018.

[9] G. Laplanche, A. Kostka, C. Reinhart, J. Hunfeld, G. Eggeler, E.P. George, Reasons for the superior mechanical properties of medium-entropy CrCoNi compared to high-entropy CrMnFeCoNi, Acta Mater. 128 (2017) 292–303. doi:10.1016/j.actamat.2017.02.036.

[10] B.C. De Cooman, Y. Estrin, S.K. Kim, Twinning-induced plasticity (TWIP) steels, Acta Mater. 142 (2018) 283–362. doi:10.1016/j.actamat.2017.06.046.

[11] O. Grässel, L. Krüger, G. Frommeyer, L.W. Meyer, High strength Fe-Mn-(Al, Si) TRIP/TWIP steels development - properties - application, Int. J. Plast. 16 (2000) 1391–1409. doi:10.1016/S0749-6419(00)00015-2.

[12] N.D. Stepanov, D.G. Shaysultanov, R.S. Chernichenko, N.Y. Yurchenko, S. V. Zherebtsov, M.A. Tikhonovsky, G.A. Salishchev, Effect of thermomechanical processing on microstructure and mechanical properties of the carbon-containing CoCrFeNiMn high entropy alloy, J. Alloys Compd. 693 (2017) 394–405. doi:10.1016/j.jallcom.2016.09.208.

[13] N.D. Stepanov, D.G. Shaysultanov, R.S. Chernichenko, D.M. Ikornikov, V.N. Sanin, S.V. Zherebtsov, Mechanical properties of a new high entropy alloy with a duplex

ultra-fine grained structure, Mater. Sci. Eng. A. 728 (2018) 54–62. doi:10.1016/j.msea.2018.04.118.

[14] J.B. Seol, J.W. Bae, Z. Li, J. Chan Han, J.G. Kim, D. Raabe, H.S. Kim, Boron doped ultrastrong and ductile high-entropy alloys, Acta Mater. 151 (2018) 366–376. doi:10.1016/j.actamat.2018.04.004.

[15] Z. Li, C.C. Tasan, K.G. Pradeep, D. Raabe, A TRIP-assisted dual-phase high-entropy alloy: Grain size and phase fraction effects on deformation behavior, Acta Mater. 131 (2017) 323–335. doi:10.1016/j.actamat.2017.03.069.

[16] R. Pippan, S. Scheriau, A. Hohenwarter, M. Hafok, Advantages and Limitations of HPT: A Review, Mater. Sci. Forum. 584–586 (2008) 16–21. doi:10.4028/www.scientific.net/MSF.584-586.16.

[17] R. Pippan, S. Scheriau, A. Taylor, M. Hafok, A. Hohenwarter, A. Bachmaier, Saturation of fragmentation during severe plastic deformation, Annu. Rev. Mater. Res. 40 (2010) 319–343. doi:10.1146/annurev-matsci-070909-104445.

[18] R. Valiev, Nanostructuring of metals by severe plastic deformation for advanced properties, Nat. Mater. 3 (2004) 511–516. doi:10.1038/nmat1180.

[19] R.Z. Valiev, R.K. Islamgaliev, I. V. Alexandrov, Bulk nanostructured materials from severe plastic deformation, Prog. Mater. Sci. 45 (2000)103-189. doi:10.1016/S0079-6425(99)00007-9.

[20] A.P. Zhilyaev, T.G. Langdon, Using high-pressure torsion for metal processing: Fundamentals and applications, Prog. Mater. Sci. 53 (2008) 893–979. doi:10.1016/j.pmatsci.2008.03.002.

[21] E. Ma, Instabilities and ductility of nanocrystalline and ultrafine-grained metals, Scr. Mater. 49 (2003) 663–668. doi:10.1016/S1359-6462(03)00396-8.

[22] E. Ma, Eight routes to improve the tensile ductility of bulk nanostructured metals and alloys, JOM 58 (2006) 49–53. doi:10.1007/s11837-006-0215-5.

[23] Y. Zhao, Y. Zhu, E.J. Lavernia, Strategies for improving tensile ductility of bulk nanostructured materials, Adv. Eng. Mater. 12 (2010) 769–778. doi:10.1002/adem.200900335.

[24] Y.M. Wang, E. Ma, Three strategies to achieve uniform tensile deformation in a nanostructured metal, Acta Mater. 52 (2004) 1699–1709. doi:10.1016/j.actamat.2003.12.022.

[25] Y.M. Wang, E. Ma, M.W. Chen, Enhanced tensile ductility and toughness in nanostructured Cu, Appl. Phys. Lett. 80 (2002) 2395–2397. doi:10.1063/1.1465528.

[26] Y. Wang, M. Chen, F. Zhou, E. Ma, High tensile ductility in a nanostructured metal., Nature. 419 (2002) 912–915. doi:10.1038/nature01133.

[27] B. Schuh, B. Völker, J. Todt, K.S. Kormout, N. Schell, A. Hohenwarter, Influence of Annealing on Microstructure and Mechanical Properties of a Nanocrystalline CrCoNi Medium-Entropy Alloy, Materials 11 (2018). doi:10.3390/ma11050662.

[28] B. Schuh, F. Mendez-Martin, B. Völker, E.P. George, H. Clemens, R. Pippan, A. Hohenwarter, Mechanical properties, microstructure and thermal stability of a nanocrystalline CoCrFeMnNi high-entropy alloy after severe plastic deformation, Acta Mater. 96 (2015) 258–268. doi:10.1016/j.actamat.2015.06.025.

[29] MathWorks, MatLab, https://de.mathworks.com/; Last accessed : 08/2018.

[30] G.B. Rathmayr, A. Bachmaier, R. Pippan, Development of a new testing procedure for performing tensile tests on specimens with sub-millimetre dimensions, J. Test. Eval. 41 (2013) 1–12. doi:10.1520/JTE20120175.

[31] F. Otto, A. Dlouhý, K.G. Pradeep, M. Kubênová, D. Raabe, G. Eggeler, E.P. George, Decomposition of the single-phase high-entropy alloy CrMnFeCoNi after prolonged anneals at intermediate temperatures, Acta Mater. 112 (2016) 40–52. doi:10.1016/j.actamat.2016.04.005.

[32] E.J. Pickering, R. Muñoz-Moreno, H.J. Stone, N.G. Jones, Precipitation in the equiatomic high-entropy alloy CrMnFeCoNi, Scr. Mater. 113 (2016) 106–109. doi:10.1016/j.scriptamat.2015.10.025.

[33] N.D. Stepanov, D.G. Shaysultanov, M.S. Ozerov, S.V. Zherebtsov, G.A. Salishchev, Second phase formation in the CoCrFeNiMn high entropy alloy after recrystallization annealing, Mater. Lett. 185 (2016) 1–4. doi:10.1016/j.matlet.2016.08.088.

[34] H. Shahmir, T. Mousavi, J. He, Z. Lu, M. Kawasaki, T.G. Langdon, Microstructure and properties of a CoCrFeNiMn high-entropy alloy processed by equal-channel angular pressing, Mater. Sci. Eng. A. 705 (2017) 411–419. doi:10.1016/j.msea.2017.08.083.

[35] V.L. Tellkamp, E.J. Lavernia, A. Melmed, Mechanical behavior and microstructure of a thermally stable bulk nanostructured Al alloy, Metall. Mater. Trans. A. 32 (2001) 2335–2343. doi:10.1007/s11661-001-0207-6.

[36] Y. Zhao, T. Topping, Y. Li, E.J. Lavernia, Strength and ductility of bi-modal Cu, Adv. Eng. Mater. 13 (2011) 865–871. doi:10.1002/adem.201100019.

[37] Y. Zhao, T. Topping, J.F. Bingert, J.J. Thornton, A.M. Dangelewicz, Y. Li, W. Liu, Y. Zhu, Y. Zhou, E.J. Lavernia, High tensile ductility and strength in bulk nanostructured nickel, Adv. Mater. 20 (2008) 3028–3033. doi:10.1002/adma.200800214.

[38] S.P. Joshi, K.T. Ramesh, B.Q. Han, E.J. Lavernia, Modeling the constitutive response of bimodal metals, Metall. Mater. Trans. A. 37 (2006) 2397–2399. doi:https://doi.org/10.1007/BF02586214.

[39] B. Raeisinia, C.W. Sinclair, W.J. Poole, C.N. Tomé, On the impact of grain size distribution on the plastic behaviour of polycrystalline metals, Model. Simul. Mater. Sci. Eng. 16 (2008) 025001. doi:10.1088/0965-0393/16/2/025001.

[40] A. Magee, L. Ladani, T.D. Topping, E.J. Lavernia, Effects of tensile test parameters on the mechanical properties of a bimodal Al-Mg alloy, Acta Mater. 60 (2012) 5838–5849. doi:10.1016/j.actamat.2012.07.024.

[41] Y. Li, Z. Zhang, R. Vogt, J.M. Schoenung, E.J. Lavernia, Boundaries and interfaces in ultrafine grain composites, Acta Mater. 59 (2011) 7206–7218. doi:10.1016/j.actamat.2011.08.005.

[42] X. Huang, N. Hansen, N. Tsuji, Hardening by Annealing and Softening by Deformation in Nanostructured Metals, Science 312 (2006) 249–251. doi:10.1126/science.1124268.

[43] O. Renk, A. Hohenwarter, B. Schuh, J.H. Li, R. Pippan, Hardening by annealing: Insights from different alloys, IOP Conf. Ser. Mater. Sci. Eng. 89 (2015) 012043. doi:10.1088/1757-899X/89/1/012043.

[44] E. Ma, T.D. Shen, X.L. Wu, Nanostructured metals: less is more., Nat. Mater. 5 (2006) 515–516. doi:10.1038/nmat1671.

[45] R.Z. Valiev, N.A. Enikeev, M.Y. Murashkin, V.U. Kazykhanov, X. Sauvage, On the origin of the extremely high strength of ultrafine-grained Al alloys produced by severe plastic deformation, Scr. Mater. 63 (2010) 949–952. doi:10.1016/j.scriptamat.2010.07.014.

[46] E. El-Danaf, S.R. Kalidindi, R. Doherty, Influence of grain size and stacking fault energy on deformation twinning in fcc metals., Metall. Mater. Trans. A. 30A (1999) 1223–1233.

[47] O. Renk, A. Hohenwarter, R. Pippan, Cyclic deformation behavior of a 316L austenitic stainless steel processed by high pressure torsion, Adv. Eng. Mater. 14 (2012) 948–954. doi:10.1002/adem.201200015.

[48] G.J. Fan, H. Choo, P.K. Liaw, E.J. Lavernia, Plastic deformation and fracture of ultrafine-grained Al-Mg alloys with a bimodal grain size distribution, Acta Mater. 54 (2006) 1759–1766. doi:10.1016/j.actamat.2005.11.044.

[49] Y. Zhang, S. Sabbaghianrad, H. Yang, T.D. Topping, T.G. Langdon, E.J. Lavernia, J.M. Schoenung, S.R. Nutt, Two-Step SPD Processing of a Trimodal Al-Based Nano-Composite, Metall. Mater. Trans. A. 46 (2015) 5877–5886. doi:10.1007/s11661-015-3151-6.

[50] Y.Z. Tian, S. Gao, L.J. Zhao, S. Lu, R. Pippan, Z.F. Zhang, N. Tsuji, Remarkable transitions of yield behavior and Lüders deformation in pure Cu by changing grain sizes, Scr. Mater. 142 (2018) 88–91. doi:10.1016/j.scriptamat.2017.08.034.

[51] A. Hohenwarter, R. Pippan, Fracture and fracture toughness of nanopolycrystalline metals produced by severe plastic deformation, Philos. Trans. R. Soc. A. 373 (2015) 1-17. doi:10.1098/rsta.2014.0366.

C.

Phase Decomposition of a Single-Phase AlTiVNb High-Entropy Alloy after Severe Plastic Deformation and Annealing

B. Schuh [a], B.Völker [a], V. Maier-Kiener [b], J. Todt [a], J. Li [c], A. Hohenwarter [a]

[a] Department of Materials Physics; Montanuniversität Leoben and Erich Schmid Institute of Materials Science, Austrian Academy of Sciences, Jahnstraße 12, 8700 Leoben, Austria

[b] Department of Physical Metallurgy and Materials Testing, Montanuniversität Leoben, Roseggerstraße 12 8700 Leoben, Austria

[c] Institute of Casting Research, Montanuniversität Leoben, Franz-Josef-Straße 18, 8700 Leoben, Austria

Abstract

An equiatomic AlTiVNb high-entropy alloy is subjected to severe plastic deformation using high-pressure torsion, leading to a substantial refinement of the microstructure. The nanocrystalline samples then are subjected to isochronal heat treatments performed for 1 hour and temperatures between 300°C and 700°C. This results in a significant hardness increase from approximately 7.4 GPa for the as-processed state to ~ 10.4 GPa for an annealing temperature of 700°C, while for higher temperatures the hardness starts to decrease due to the onset of structural coarsening. Furthermore the reduced modulus of the material is measured, which increases after annealing treatments as well. Investigations using electron microscopy, synchrotron x-ray diffraction and nanoindentation are performed in order to determine the origin of the unusual annealing response of the AlTiVNb alloy. It will be shown that the changes can be related to the formation of intermetallic phases basically creating a multi-phase nanocomposite material during annealing. Additionally nanoindentation testing is performed after the isothermal heat treatments at the peak hardness temperature of 700°C in order to study the kinetics of this process. The results obtained from the nanocrystalline materials therefore give new insights into the thermodynamic stability of this alloy, which are also relevant for coarser-grained microstructures.

C.1 Introduction

High entropy alloys (HEAs) are currently receiving overwhelming attention from the materials science community, demonstrated by the abundance of papers and events devoted to this topic [1]–[5]. On account of their diversity caused by their multi-principle element character and due to the rather loose definitions, the pool of alloys considered to be a HEA is tremendous, although alloys with a multi-phase microstructure are addressed as Constitutionally Complex alloys (CCAs) as a further distinction lately. In fact, only a minority of systems are true single phase alloys with typically face-centered-cubic (fcc)[6][7] or body-centered-cubic (bcc) structures [8][9]. Even in that small subset some alloys decompose to a multi-phase structure upon annealing, see for instance [10]–[12]. An often proposed potential field of application for HEAs in future is the high-temperature regime [8][13]–[16]due to their occasionally outstanding specific yield strengths [17]–[19] and their proposed sluggish diffusion behavior[2][20]. In recent years several alloys containing refractory metals for high-temperature use have been investigated [8][13]–[16]. One of the rare single-phase examples is the quaternary, equiatomic AlTiVNb [21] alloy, showing a bcc-structure in the as-cast state. It features exceptional compressive yield strength up to temperatures of 800°C and a low density of 5.59 g cm^{-3}. In addition, the AlTiVNb alloy also serves as a base for several other HEAs, e.g. with the addition of Zr [19] or Cr [22], where second phase precipitation is achieved, which might improve the high temperature properties further.

Recent studies concerning the thermodynamic stability of HEAs have extended to the nanocrystalline (NC) grain size regime [23]. It was shown that potential phase decomposition processes during annealing treatments at relatively low temperatures can occur rapidly in NC materials. The fast diffusion kinetics have been rationalized by the abundance of grain boundaries acting as fast diffusion pathways and preferential nucleation sites in the NC state. Another contributing factor to the enhanced diffusion in SPD processed materials might be the presence of a high number of deformation induced vacancies [24].Since the observed phase decomposition is of thermodynamic nature and not a sole peculiarity of the NC state, severe plastic deformation (SPD) processing offers a pragmatic way to study the thermodynamic stability of a certain HEA. In contrast, the investigation of the same alloy in its coarse-grained state often requires long-term heat treatments in order to achieve the same decomposition behavior [10][11].

Based on these ideas the AlTiVNb alloy was at first transformed into a NC state utilizing high-pressure torsion (HPT) processing and subsequently subjected to various heat treatments between 300°C and 1000°C. The annealed states then were both mechanically and microstructurally investigated in order to determine:

1. The effect of SPD processing on the mechanical properties of the AlTiVNb alloy.
2. The thermodynamic stability of the equiatomic AlTiVNb system as well as possible microstructural changes occurring during the annealing treatments.

With the indirect approach of investigating the NC-state of an alloy, thus having the advantage of accelerated kinetics, the obtained results can provide valuable information on the microstructural stability of the conventionally coarser-grained AlTiVNb HEA. In this way the results will help to evaluate the alloy's applicability as a high-temperature alloy in future.

C.2 Experimental

Button-shaped ingots (~ 20 mm in diameter, ~ 10 mm in height) were produced from high-purity elements (>99.99 wt%) using arc melting and then re-melted several times to improve the chemical homogeneity. Small cylinders with a diameter of 8 mm (length ~ 10 mm) were processed from the ingots by electrical discharge machining. From these cylinders disks for HPT deformation with 0.8 mm thickness were machined.

The material was processed by quasi-constrained HPT, an in-depth description of this processing technique is given in [25]. HPT processing was performed at room temperature with a pressure of 7.8 GPa using a rotational speed of 0.2 rotations/min. During HPT processing the ideal shear strain γ is given by

$$\gamma = \frac{2\pi r n}{t} \qquad \textbf{Equation C.1}$$

, where r is the sample radius, t is the sample thickness and n the number of rotations. For all samples 5 rotations were applied resulting in a saturation of grain-refinement at r > 1 mm. The deformed samples were subjected to isochronal (1h) heat treatments performed for temperatures between 300°C and 1000°C as well as isothermal heat treatments at 700°C for varying annealing times.

For nanoindentation as well as for investigations performed via scanning electron microscopy (SEM) the samples were ground and polished, first mechanically with SiC paper and then mechano-chemically (OPS). For transmission electron microscopy (TEM) specimen preparation, samples were first ground down to 100 µm, then mechanically dimpled to about 10 µm and finalized using Ar ion-milling.

The microstructure was studied by employing a SEM (Zeiss 1525) and a TEM from Philips (CM12), which was used for conventional bright field imaging and to obtain electron diffraction pattern images. An image-side Cs-corrected JEOL 2100F was further used for scanning-TEM-imaging as well as energy dispersive x-ray spectroscopy (EDX) measurements. Synchrotron X-ray diffraction (XRD) experiments were performed at the PETRA III beamline at the DESY Photon Science facility using a beam energy of 87.1 keV. The measured transmission diffraction patterns were analyzed using the software *FIT2D* [26] and *Match!* [27], utilizing the Crystallography Open Database, PDF-2 as well as the Inorganic Crystal Structure Database. The diffraction pattern of LaB_6 was used as a reference for detector geometry calibration.

For local characterization a platform nanoindenter G200 (Keysight-Tec) equipped with a diamond Berkovich tip, was utilized. Calibrations of tip shape and frame stiffness were performed regularly following the Oliver Pharr method with fused silica[28]. By using a continuous stiffness measurement (CSM, 45 Hz, 2 nm oscillation amplitude) unit depth dependent local mechanical properties were determined. All nanoindentation experiments were performed in constant strain rate mode and at thermal drift rates of less than 0.1 nm/s. Hardness and reduced indentation modulus[28][29] (Directly derived from the Sneddon's equation, containing both, the Young's modulus of tip and sample. However, since no information on the Poisson's ratio of the AlTiVNb alloy currently exists in literature no absolute Young's modulus can be evaluated) were determined by constant strain rate indentation (0.05 s^{-1}) to a preset indentation depth of 2500 nm. The calculated depth dependent mechanical properties were further averaged between 1500 nm and 2000 nm indentation depth. For strain rate jump tests [30] the applied strain rate was abruptly changed in 500 nm intervals. Thermally activated processes then could be

quantified by calculating the strain rate sensitivity (SRS) m and activation volume V^* ($V^* = C^* \cdot \sqrt{3} \cdot k_B \cdot T/mH$) instantaneously [31] from the measured dependence of hardness H on strain rate $\dot{\varepsilon}$ directly at the preset jump indentation in order to probe a constant microstructural state (with C^*: constraint factor of 2.8, k_B: Boltzmann constant, T: room - temperature 25 °C). Detailed information on these procedures can be found in the references [32][31].

C.3 Results

C.3.1 Microstructural evolution and hardness

The as-cast material shows a coarse-grained microstructure (Figure 1a) with grains in the size range of several hundreds of micrometers, exhibiting a dendritic structure. The dendritic regions are slightly enriched in Nb and interdentritic areas have a higher Al content as EDX-measurements revealed (not shown here).

The hardness evolution as a function of the shear strain is presented in Figure 1b. Two indentations at equivalent positions were made along the radius at intervals of 0.25 mm and averaged. The corresponding shear strains were calculated using Equation 1. The AlTiVNb alloy in its as-cast state has a relatively high hardness of ~ 6.2 GPa. With an increase in applied strain the hardness increases due to grain refinement. At a shear strain of about 50 a hardness plateau of ~ 7.4 ± 0.5 GPa is reached suggesting a saturation in grain refinement.

The changes in hardness are reflected by the changes in the microstructure. Figure 1c shows the near center region of the disk after n = ¼ rotation, which has experienced almost no shear deformation (γ~0) but some compressive deformation during loading of the HPT disk. The changes in contrast represent local changes in orientation and additionally some of the original grain boundaries can be detected near the center region. With higher applied strains the deformation starts to localize in shear bands, in which the microstructure is more refined compared to the material outside of the shear bands (Figure 1d). When the shear strain is increased further the number of bands increases as well, see Figure 1e. For significantly higher applied shear strains of about 50 (which is equivalent to a radial position of ~ 1 mm after 5 rotations) and above the microstructure is homogenously refined (Figure 2a) and a microstructural equilibrium state is reached.

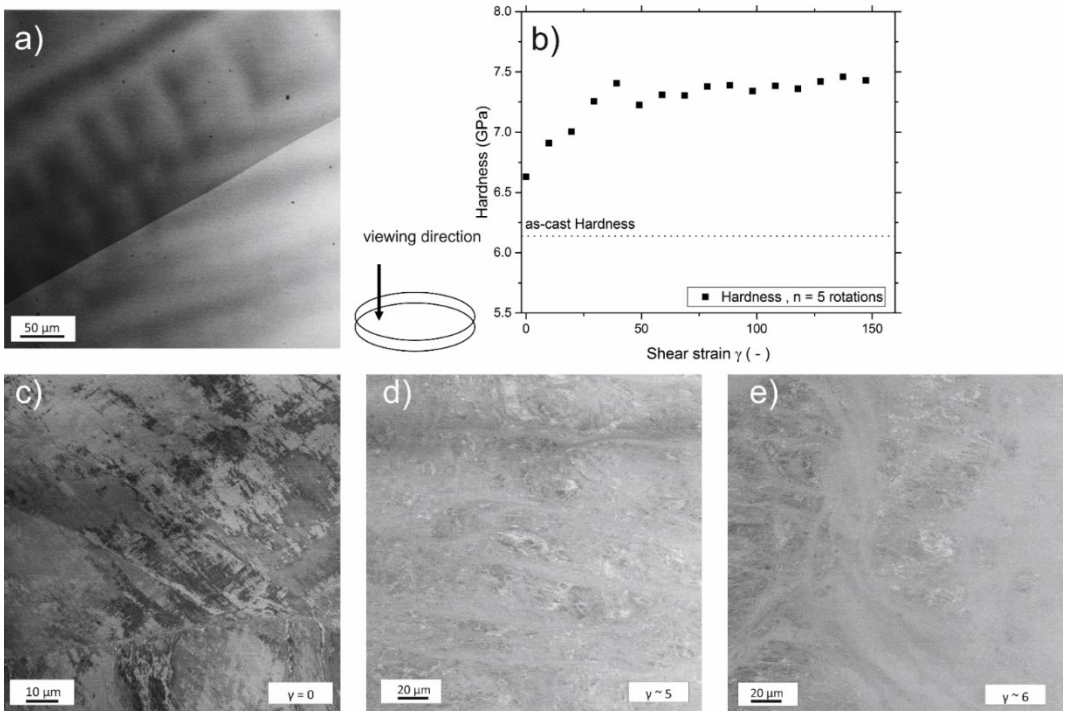

Figure 1: a) Low-magnification back scatter electron-micrograph showing the coarse-grained microstructure of the as-cast AlTiVNb high-entropy alloy. The average grain size is in the range of several hundred micrometers and most grains show a dendritic structure. b) Hardness evolution as a function of shear strain. A plateau is reached for shear strains larger than approximately 50. c-e) BSE images taken for different shear strains. c) near center region after a quarter rotation, ideally only compressed d) For shear strains of about 5 shear banding commences with a strongly refined microstructure within the bands e) Further increase in shear strain, γ~6, leads to an increase in the number of shear bands and a gradual transformation to a homogeneous NC structure.

C.3.2 Characterization of the saturation state

The saturation microstructure was studied more thoroughly using TEM, see Figure 2a. The formation of non-equilibrium grain boundaries during HPT and their characteristic property of exhibiting long-range elastic stresses leads to often poorly discernible structures and boundaries using classical TEM, thus making an exact measurement of the saturation grain size difficult [33]. However, based on the grains that are clearly visible in dark field imaging, it can be estimated that the saturation grain size of the investigated AlTiVNb-alloy is in the range of 50 nm. In the inset of Figure 2a the corresponding electron diffraction pattern is shown. All rings fit to a single-phase bcc material with a lattice constant of about 319 pm , which is in agreement with previous reports in literature, where a lattice constant of 318 ± 3 pm was measured via XRD by Stepanov et al. [21]. Additionally, it could be revealed that the AlTiVNb alloy retains its single-phase character after HPT deformation by synchrotron XRD measurements (Figure 2b), the corresponding lattice constant for the XRD measurements is ~ 319 pm. The small discrepancy between the lattice constant measured via XRD compared to the measurements performed by Stepanov et al. can be explained by the fact that the chemistry of the two alloys may not exactly be the same. Additionally slight inaccuracies in determining the detector-sample distance might also be a possible source of error. In Table 1 the average chemical

composition of the HPT deformed material can be seen. Average values and standard deviations were calculated using 50 datapoints of a line-scan in the saturation region performed by SEM-EDX.

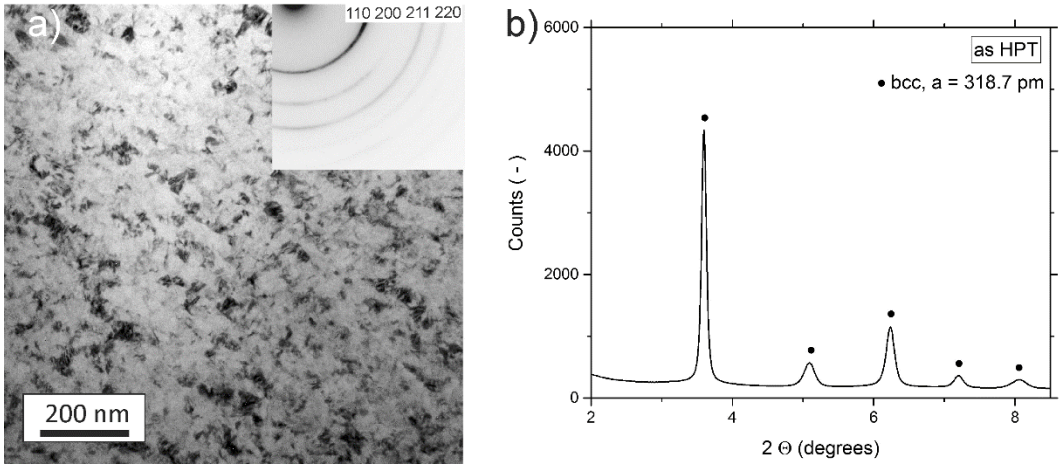

Figure 2: a) Bright-Field TEM image of the saturation state microstructure. The electron diffraction pattern (inset of a) reveals that the alloy is a single-phase bcc-alloy after HPT processing, which is in agreement with XRD-measurements (b). The corresponding lattice constant of the severely deformed alloy is ~ 319 pm.

Chemical Composition [at%]	
Al	25.3 ± 0.2
Nb	25.7 ± 0.5
Ti	24.5 ± 0.3
V	24.5 ± 0.2

Table 1: Average chemical composition of a HPT processed sample measured via SEM-EDX.

By applying strain rate jump tests, information on thermally activated deformation processes was obtained. For the coarse-grained as-cast state the SRS m is 0.0145 and the activation Volume V^* equals ~ $11.5 \cdot b^3$. However, for the nanocrystalline HPT state m increases to 0.019 and V^* drops to approximately $7.15 \cdot b^3$, see Table 2.

Microstructural state	Strain rate sensitivity m [-]	Activation volume V* [b^3]
as-cast	0.0145 ± 0.0006	11.50 ± 0.76
HPT	0.0192 ± 0.0011	7.15 ± 0.41

Table 2: Strain rate sensitivity and activation volume for the as-cast and HPT processed sample

C.3.3 Annealing response

Changes in hardness as well as reduced modulus were determined via nanoindentation testing. All values were obtained by averaging the results of six indents, the error bar represent the standard deviation between multiple equivalent indents, see Figure 3. Even for relatively low annealing temperatures a significant rise in hardness can be detected, which increases further up to 700°C exhibiting a hardness of about 10.4 GPa. This is a rise of about 3 GPa compared to the HPT state. For higher annealing temperatures the hardness starts to decrease to about 8.5 GPa for 1000°C.From the contact stiffness the reduced modulus of the corresponding annealing states could also be determined. The HPT state has a modulus of approximately 128.3 ± 0.7 GPa, which is significantly lower than the as-cast material with a reduced modulus of about 155.5 ± 5.25 GPa. When the NC material is annealed the reduced modulus increases as well, reaching a maximum at 800°C (170.8 ± 0.8 GPa). In contrast to the hardness the modulus shows no significant decrease for higher annealing temperatures of 800°C and above.

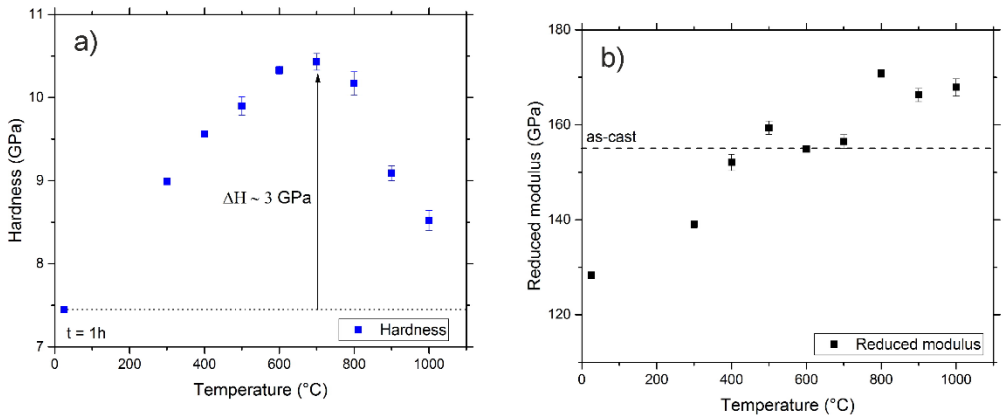

Figure 3: a) Hardness evolution during isochronal anneals (t= 1h) for temperatures between 300°C and 1000°C. The hardness reaches a maximum of about 10.4 GPa for an annealing temperature of 700°C, while for higher temperatures the alloy shows softening. b) Reduced modulus as a function of temperature. It increases with rising annealing temperatures as well, but unlike for the hardness there is no drop-off for heat treatments above 700°C.

In order to determine the causes of the peculiar changes in the mechanical properties during annealing synchrotron XRD measurement were employed. As seen in Figure 4a for relatively low annealing temperatures up to 500°C no changes in the XRD pattern can be detected. At an annealing temperature of 700°C, the formation of additional peaks can be

observed. Besides the original bcc phase the additional peaks suggest the presence of a Nb_2Al phase (Figure 4a and b). Noteworthy is that the peaks for the 700°C specimen are relatively broad. This can be an effect of the NC nature of the additional phase but also a result of the presence of another phase.

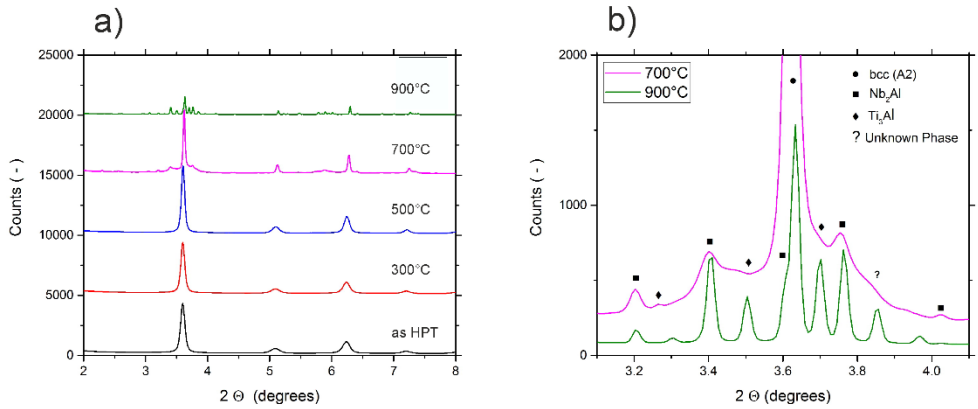

Figure 4: a) Synchrotron XRD-measurements imply that the SPD state as well as annealing states up to temperatures of 500°C for 1h show no changes in the single-phase bcc structure of the alloy. b) Further details of a). For the 700°C sample additional phases form. For the 900°C sample the multi-phase structure remains, at least one additional un-indexed peak appears as well.

For the 900°C sample the peaks have become narrower and more numerous. While the original bcc high-entropy phase is still present in the material, the peaks corresponding to the Nb_2Al phase have become much more pronounced. Additionally, due to the reduced width of the surrounding peaks, the partially overlapped peaks in the 700°C sample are now clearly separated. By reviewing conventional databases and taking into account the possible phases that can form and are known from the binary systems of the four base elements, the development of Ti_3Al seems to be most likely. However, not all peaks can be related to these phases, see Figure 4b, suggesting that an additional phase could be present as well.

In order to put these results into perspective TEM-experiments were performed, initially starting with a specimen annealed at 500°C for 1h. This complimentary method was chosen, because for XRD-measurements it is known that often volume-fractions of a few vol.% are required to be detectable [34]. Therefore, it is important to investigate the possibility of an onset of precipitation at lower temperatures than 700°C.

In Figure 5a the microstructure of a 1-hour annealed specimen at 500°C is presented. In comparison to the HPT state the microstructure appears slightly clearer although grain boundaries overall still seem ill-defined and the annealed specimen shows very little grain growth. The electron diffraction pattern does not show significant changes compared to the as-deformed state, all patterns can still be indexed as the original bcc phase. The sample annealed at 700°C for 1h (Figure 5b) shows much more pronounced changes. The microstructure now appears very clear and there has been noticeable grain growth. More importantly in the diffraction pattern additional rings are clearly visible, which can be ascribed to a Nb_2Al-phase. Additionally high-angle angular dark field (HAADF) imaging was performed, revealing darker and lighter regions. Subsequent analysis via TEM-EDX revealed that the lighter regions are distinctly enriched in Nb and Al. (Figure 5 c and d). Regarding the possible presence of Ti_3Al in the 700°C sample, no clear evidence could be found via TEM investigations. For annealing temperatures up to 700°C the microstructure

remains fine grained, as can be seen in Figure 5b. Higher annealing temperatures lead to a significant increase of the average grain size.

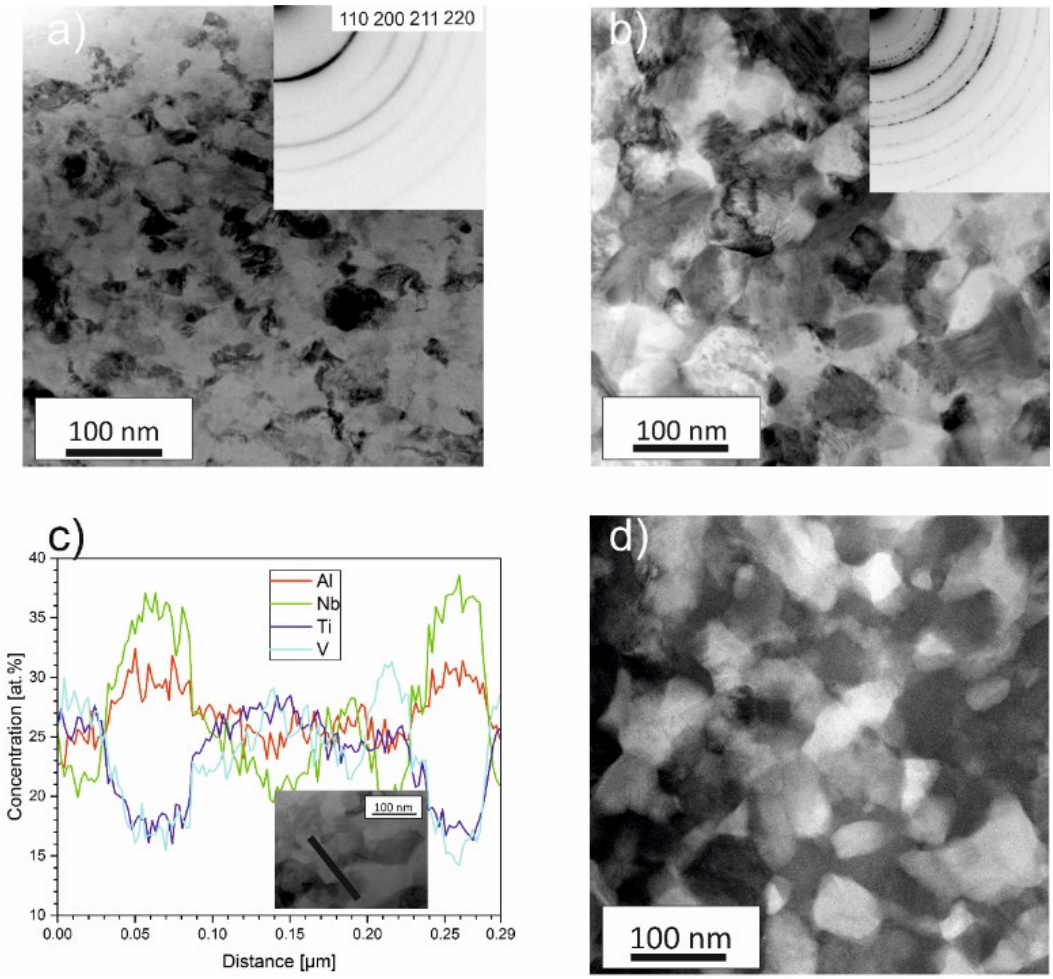

Figure 5: TEM images of specimens annealed at 500°C and 700°C for 1h. a) For the 500°C sample no additional phases can be detected and the grain boundaries still seem ill-defined. b) For the 700°C sample slight grain growth and the formation of additional phases occurs. c) Line scan indicating that lighter regions are enriched in Nb and Al. d) A high-angle angular dark-field (Z-contrast) image showing regions being distinctly lighter (Nb-rich) and darker.

To study the kinetics of the microstructural processes, isothermal heat treatments at 700°C were additionally performed for 5 minutes, 1 hour and 15 hours (Table 3). Even after just 5 minutes of annealing the increase in hardness, about 2.6 GPa, is very remarkable, almost reaching the value obtained after the 1h heat treatment. With a further increase in annealing time to 15h the hardness continues to increase only slightly. The reduced modulus shows an equally strong increase within very short term anneals as well, however, with prolonged annealing times the further increase in reduced modulus is much more pronounced compared to increase in hardness, reaching about 176.5 GPa.

Time	Reduced modulus [GPa]	Hardness [GPa]
HPT	128.3 ± 0.7	7.4 ± 0.5
5 minutes	155 ± 0.6	10.06 ± 0.05
1 hour	156.5 ± 1.4	10.43 ± 0.1
15 hours	176.5 ± 1.1	10.86 ± 0.03

Table 3: Evolution of the reduced modulus and the hardness as a function of time for isothermal anneals at 700°C.

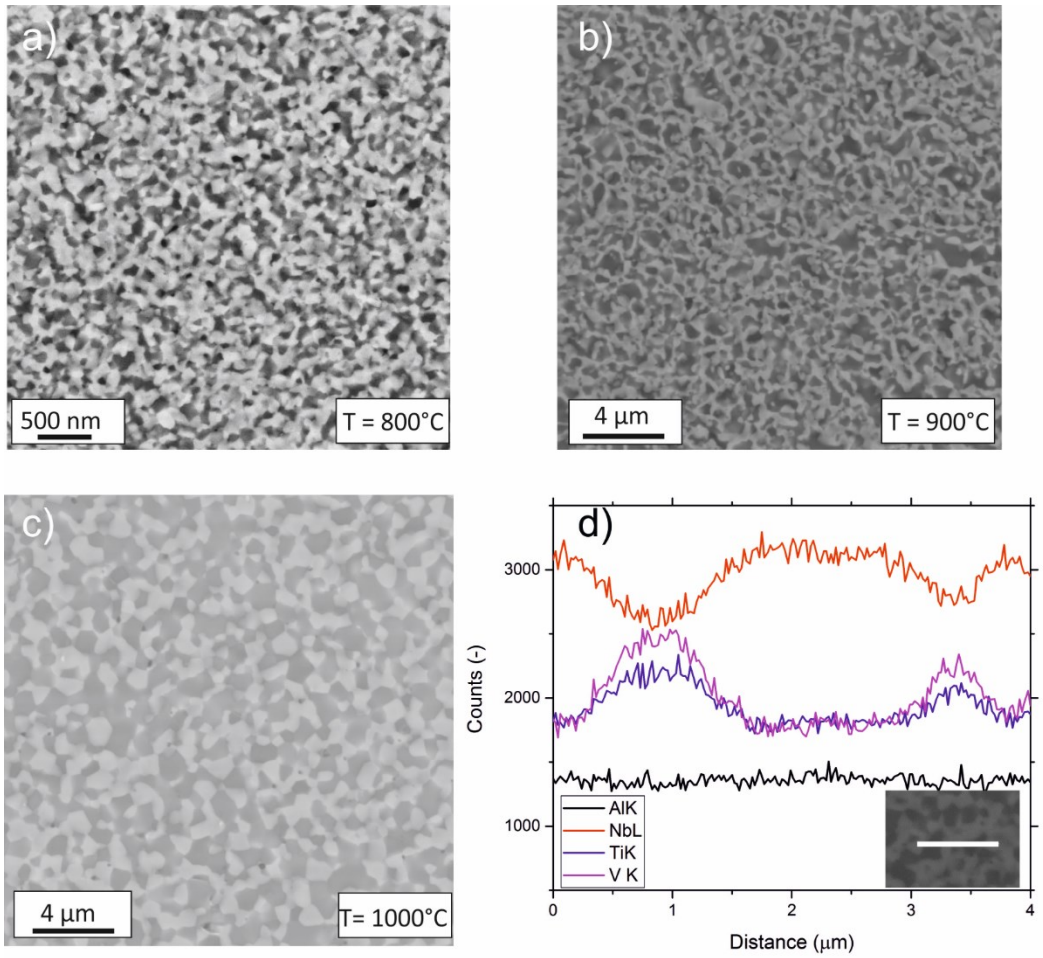

Figure 6: BSE micrographs of the samples annealed at 800°C (a), 900°C (b) and 1000°C (c) for 1h. While the average grain size for the 800°C sample is still in a sub-micrometer regime, for the 1000°C-anneal the grains have grown to an average grain size of 1-2 µm. d) Line-scan performed on a 1000°C sample showing areas enriched in Nb, which appear lighter in the BSE micrograph.

After a heat treatment of 800°C for 1h the grains are still in the sub-micrometer regime (Figure 6a), however at the maximum annealing temperature of 1000°C the grains already have grown to an average size of about 1-2 µm, see Figure 6c. The BSE micrograph of the

1000°C sample clearly shows lighter and darker regions. By utilizing SEM-EDX line scans it can be qualitatively shown that the lighter regions are again enriched in Nb (Figure 6d), which represents the Nb_2Al phase most likely.

C.4 Discussion

C.4.1 Microstructural Development and homogeneity

The as-cast state of the alloy experiences no homogenization treatment and is therefore chemically inhomogeneous. The high hardness of the coarse-grained as cast state most likely can be explained by a strong solid-solution hardening effect. In Fig. 1a, dendritic areas slightly enriched in elements with high melting point, in this case mostly Nb, and interdentritic regions, which show a somewhat higher Al contents, are visible. After HPT processing this chemical inhomogeneity could not be detected by utilizing SEM-EDX anymore. On this length scale, with probing areas in the range of several square-micrometers, homogeneity was achieved. In the literature, chemical homogenization by SPD processing has been reported previously. For instance Pouryazdan *et al.* [35] reported forced chemical mixing in an $Ag_{60}Cu_{40}$ alloy, where chemical homogenization of the original eutectic microstructure could be achieved by HPT processing. In a similar fashion Quelennec *et al.* [36] dispersed 50 nm thick iron filaments into a copper matrix and could show by means of 3-dimensional atom probe tomography that after 25 rotations via HPT a supersaturated solid solution could be created where the iron was uniformly distributed in the copper matrix.

C.4.2 Nanoindentation and strain rate sensitivity

At first the trends for the SRS m and the activation volume V^* obtained during nanoindentation (Table 2) testing seem highly peculiar for a single-phase bcc metal. Several authors previously discussed an opposite trend for different bcc-materials investigated by various testing techniques ranging from uniaxial macroscopic testing to multiaxial local testing and for different microstructures. Wei *et al.* [32] for instance reported a highly reduced SRS after they processed Fe and Ta by severe plastic deformation. Höppel *et al*. [37][38] found similar results for Fe and for Cr [39] and W [30] also a reduced SRS for the NC states was obtained at room temperature.

Generally this trend is opposite to that found in fcc materials where an increased SRS is recorded in NC materials. This is mainly discussed in terms of thermally activated dislocation motion and annihilation processes at high angle grain boundaries and moreover in close relationship to a considerably high ductility in these high strength materials. For bcc materials, however, the amount of SRS is directly dependent on the materials specific Peierls stress, which each dislocations has to overcome during deformation and which is strongly dependent on the testing temperature [40]. However, exemplarily, given the work performed by Maier *et al*. [39] for single-crystalline and ultra-fine grained Cr, it could be shown that for testing temperatures of 300°C this trend was reversed and the SRS started to increase with decreasing grain size, similar to results obtained within this study for AlTiVNb at room-temperature. This behavior was explained that if a certain critical temperature T_c is exceeded thermally activated dislocation-grain boundary interactions start to become more dominant. While for Cr T_c seems to lie somewhere between 100°C and 300°C the observed trend for AlTiVNb might be explained by the fact that T_c might be below or close to room temperature. This idea is also supported by the activation volumes V^* (Table 2). For the as-cast state a V^* of $\sim 11 \cdot b^3$ is calculated, showing that thermal activation due to the kink-pair mechanism is still present. This value is also in good

agreement with other bcc-metals exhibiting low critical temperatures such as Nb (T_c~350 K), where at room temperature $V^* \sim 10 \cdot b^3$ is reported [41].

C.4.3 Annealing Response

Both hardness as well as reduced modulus significantly increase even for very low annealing temperatures (Figure 3), while changes in the microstructure and formation of intermetallic phases could only be observed for annealing temperatures of 700°C and above (Figure 5b). A strong increase in hardness upon low temperature annealing has been reported for various NC metals and can potentially be explained via dislocation annihilation, since in NC metals there is an abundance of grain boundaries acting as dislocations sinks during annealing. In order to realize plastic deformation after annealing the activation of new dislocations sources might be necessary, which requires high stresses compared to the as-processed state [42]–[44]. Another explanation in the literature for the observed hardening is the segregation of solutes to the grain boundaries [42][45]. A major contribution to the hardening of the alloy especially after annealing at elevated temperatures can be ascribed to the formation of Nb_2Al and possibly Ti_3Al. However, for classical precipitation hardening the precipitates have to be relatively small compared to the grain size. In the present case the newly formed Nb_2Al phase after the 1h-anneal at 700°C has a similar size compared to the matrix grains (See Figure 5b and d). Therefore, the composite behavior constraining deformation should be the reason for the hardness increase. Unfortunately, due to the still relatively small size of the Nb_2Al phase, it was not possible to individually test it. Despite this deficiency the phase is known to have an intermetallic character, which is usually associated with high strength.

Along with the increase of hardness an increase of the reduced modulus was also observed, which can be explained by a composite behavior for higher annealing temperatures where additional phases form. More surprising is the behavior at low temperatures and the difference between the as cast and the SPD-state (see reduced modulus data point at 20 °C, Figure 4b). The measurements imply a reduction of the modulus through SPD-processing. A decrease of the reduced modulus of NC-materials compared to coarse-grained materials has been published frequently [46]–[48]. However, it could be often ascribed to inconsistencies of the measuring technique or to the introduction of porosity. Both is very unlikely in the present case. Firstly, the measurements were always performed with the same routine. Secondly, the introduction of porosity during deformation at the presence of high hydrostatic pressures, like in HPT-processing, is not plausible. A possible explanation could be based on a pronounced anelastic behavior of the alloy, which is often attributed to NC-metals [49]. This explanation in combination with the measuring technique, based on unloading sequences, could possibly lead to the observed reduction of the modulus. With increasing annealing temperature the defect structure and therefore also the anelasticity would be reduced so that the modulus approaches the value of the coarse-grained state, without showing any indication of grain growth. Another possible explanation is the formation of texture during the HPT processing, which has been reported before in the literature [50], thus the decrease in modulus could be explained by a preferred crystallographic orientation that is more compliant. At temperatures around 500 °C the modulus is fully regenerated and the further increase can be associated with the formation of intermetallic phases.

C.4.4 Formation of intermetallic phases during annealing

As demonstrated in Figure 4 and Figure 5 the formation of intermetallic phases can be observed via TEM and XRD measurements for specimens annealed at 700°C for 1 h. Both the diffraction patterns obtained by TEM as well as XRD suggest that the newly formed

phase is Nb_2Al. Additional HAADF images in combination with TEM-EDX revealed an enrichment of Nb in certain areas. This is in good agreement with the publication of Stepanov *et al.* [22], where the formation of an intermetallic phase upon hot deformation of the AlTiVNb alloy at 800°C as well as 1000°C was observed and the new phase was determined to be Nb_2Al by means of XRD measurements. Furthermore, according to their thermodynamic simulations the intermetallic phase that should form is Ti_3Al, for annealing temperatures of about 770°C and below, however the occurrence of such a phase could not be verified experimentally by them. Considering the XRD data in Figure 4b), for annealing temperatures of 700°C and 900°C, the formation of a third phase seems to occur. Considering our XRD data and the previous simulation results by Stepanov *et al*. [22] it seems likely that the third phase is Ti_3Al. However, subsequent investigations via TEM did not yield a clear proof of the formation of Ti_3Al. A possibility to prove the existence of Ti_3Al in the 700°C specimen and possibly even more additional phases in the 900°C sample could be 3-dimensional atom probe tomography measurements in future.

It also has to be considered that the occurrence of Ti_3Al at 900°C does not match the simulated results by Stepanov *et al.* [22]. In that regard it has to be noted that prediction of equilibrium phases via Thermo-Calc using the CALPHAD method has yielded results that are often only in partial agreement with experimental results when it comes to HEAs [20][51]–[53]. For instance Zhang *et al.* [54] predicted a multi-phase structure for the CrMnFeCoNi alloy correctly at lower temperatures. However it was experimentally shown [10][11][23][55] that the single-phase structure is not restored until about 800°C, while the CALPHAD results predicted a single-phase structure for temperatures of about 600°C and above. A main problem of utilizing CALPHAD for HEA systems is that generally available databases often do not extend to the center of the phase diagram. For HEAs however the used database should be valid in the entire composition range. [56] An in-depth description of the challenges of creating such databases can be found in reference [54].

There is a significant shift of the peak-positions in the XRD measurements of the suggested phases between the 700°C and the 900°C sample, see Figure 4. For instance at $2\Theta \sim 3.27°$ the 700°C sample clearly shows a peak at the position calculated for Ti_3Al, while for the 900°C sample the peak is shifted to $2\Theta \sim 3.3°$. On the other hand, at $2\Theta \sim 3.5\ °$ the fit for the 900°C sample is much better. The intermetallic phase Nb_2Al also contains relatively large amount of "impurities" in the form of Ti and V. This variation in chemical composition certainly should lead to a difference in lattice constant compared to the "pure" phase therefore explaining the shifts of the peak positions. Taking this into account, the difference in peak position for Ti_3Al between the 700°C and the 900°C sample can most likely be explained by a variation in their chemical compositions, either because the equilibrium composition for the specific temperatures is different or because the equilibrium composition has not yet been reached after annealing for 1h. Most likely both effects contribute to the observed peak shift.

Considering Table 3 it can be seen that for example for a heat treatment at 700°C for 1 h, the material has not reached its equilibrium state yet, since both hardness as well as reduced modulus are further increasing with longer annealing times. A reasonable explanation for the further increase in modulus is the continued formation of secondary phases. The fact that the relative hardness increase for longer annealing times is much less pronounced compared to the modulus change can be rationalized by grain growth which occurs at 700°C and counteracts the hardness increase gained by additional second phase precipitation.

Assuming that the contribution of the configurational entropy to the overall thermodynamic stability determined by Gibbs free energy decreases along with decreasing

temperature, it seems reasonable that some of the observed intermetallic phases should also be stable at much lower temperatures. For these temperatures the phase decomposition is merely restricted by diffusion kinetics. This seems plausible especially considering that the 700°C sample apparently does not seem to have reached an equilibrium state after 1 h of annealing despite the accelerated diffusion kinetics that should occur in NC materials. Therefore, long-term heat treatments to achieve equilibrium states for various temperatures should be a goal of future investigations in order to get a more profound understanding of the thermodynamics of this alloy.

C.4.5 Feasibility as a high temperature material

Due to its low density and high specific yield strength up to temperatures of 800°C [21] AlTiVNb was suggested as a potential material for high temperature applications in future. However, as for instance Miracle *et al.* have pointed out, measuring a single attractive property does not necessarily qualify a material for a certain structural application [56]. Instead a multitude of properties such as for instance adequate fracture toughness, oxidation resistance, creep and fatigue behavior as well as long-term microstructural stability are required for practical applications. The latter property, microstructural stability, was investigated in this paper. The result is that the single-phase bcc structure, after casting and subsequent processing via HPT, is not thermodynamically stable. Instead after an annealing treatment in the temperature range from 700°C to 1000°C a multi-phase microstructure formed and showed an exceptional hardness. While multi-phase structures are usually desired in high-temperature applications, as for instance the intermetallic Ni_3Al in Ni-superalloys, these microstructures are highly tailored with regard to size distribution but also, for example, the lattice misfit of precipitates.

HEA development for practical applications nowadays starts to stray away from the single-phase concept [53][56] in order to gain more favourable properties by second phase precipitation, as for instance Senkov *et al.* [15] have recently demonstrated by creating a microstructure similar to those occurring in Ni-superalloys. In this case however the multi-phase structure of AlTiVNb, as demonstrated here with the NC-state, merely is a result of phase-decomposition that would likely also occur in its variants with Cr und Zr additions. Thus, long-term microstructural stability of the single-phase bcc state is questionable over a wide temperature range. If the formation of these secondary phases can be tailored to occur in a favourable fashion, AlTiVNb might be a possible candidate for future applications. However, low density and high specific yield strength alone are hardly sufficient and further investigations of other mechanical properties especially in extreme environments need to be performed to determine the feasibility of AlTiVNb as a structural material.

C.5 Summary & Conclusion

The quaternary, equiatomic AlTiVNb high-entropy alloy was subjected to high pressure torsion, leading to a NC microstructure with an approximate grain size of 50 nm. The NC material was subjected to various heat treatments in order to assess the thermodynamic stability of the alloy. In order to identify changes in the mechanical properties and microstructure nanoindentation, XRD as well as TEM were employed. The findings can be summarized as follows:

- Information on deformation mechanisms and T_c was obtained by means of nanoindentation for the as-cast as well as the HPT-processed state.
- After isochronal heat treatments of 1h a strong increase in hardness as well as reduced modulus occurs. Softening of the material commences for annealing temperatures of 800°C and above.
- Changes in mechanical properties for relatively high annealing temperatures can be explained by formation of intermetallic phases (most likely Nb_2Al and Ti_3Al) and the corresponding creation of a multi-phase-nanocomposite material. For low temperature annealing a major contribution to the hardness changes might be due to dislocation mediated processes.
- Even for the maximum annealing temperature of 1000°C the alloy does not return to its single-phase bcc state.

In conclusion, the AlTiVNb alloy is not thermodynamically stable over an extended temperature range. Even though the formation of intermetallic phases leads to an outstanding hardness of 10.4 GPa it could also result in a further embrittlement of the alloy, which would be detrimental for room-temperature applications of the NC-material. Therefore, ductility and toughness related investigations should be in the scope of future investigations.

Acknowledgments

This work was supported by the Austrian Science Fund (FWF) in the framework of Research Project P26729-N19. Parts of this research were carried out at the light source PETRA III at DESY, a member of the Helmholtz Association (HGF). We would like to thank the Helmholtz-Zentrum Geesthacht and in particular Andreas Stark for assistance in using the beamline P07. Further financial support by the Austrian Federal Government (837900) within the framework of the COMET Funding Programme is highly appreciated. We would also like to thank Prof. Reinhard Pippan for the helpful discussions.

C.6 References

[1] Y. Zhang, T.T. Zuo, Z. Tang, M.C. Gao, K.A. Dahmen, P.K. Liaw, Z.P. Lu, Microstructures and properties of high-entropy alloys, Prog. Mater. Sci. 61 (2014) 1–93. doi:10.1016/j.pmatsci.2013.10.001.

[2] J.W. Yeh, Recent progress in high-entropy alloys, Ann. Chim. Sci. Des Mater. 31 (2006) 633–648. doi:10.3166/acsm.31.633-648.

[3] J.W. Yeh, Physical Metallurgy of High-Entropy Alloys, JOM 67 (2015) 2254–2261. doi:10.1007/s11837-015-1583-5.

[4] M.H. Tsai, Physical properties of high entropy alloys, Entropy 15 (2013) 5338–5345. doi:10.3390/e15125338.

[5] M.H. Tsai, J.W. Yeh, High-Entropy Alloys: A Critical Review, Mater. Res. Lett. 2 (2014) 107–123. doi:10.1080/21663831.2014.912690.

[6] B. Cantor, I.T.H. Chang, P. Knight, A.J.B. Vincent, Microstructural development in equiatomic multicomponent alloys, Mater. Sci. Eng. A. 375–377 (2004) 213–218. doi:10.1016/j.msea.2003.10.257.

[7] W. Wang, W. Wang, S. Wang, Y. Tsai, C. Lai, J. Yeh, Effects of Al addition on the microstructure and mechanical property of AlxCoCrFeNi high-entropy alloys, Intermetallics 26 (2012) 44–51. doi:10.1016/j.intermet.2012.03.005.

[8] O.N. Senkov, G.B. Wilks, D.B. Miracle, C.P. Chuang, P.K. Liaw, Refractory high-entropy alloys, Intermetallics 18 (2010) 1758–1765. doi:10.1016/j.intermet.2010.05.014.

[9] O.N. Senkov, G.B. Wilks, J.M. Scott, D.B. Miracle, Mechanical properties of $Nb_{25}Mo_{25}Ta_{25}W_{25}$ and $V_{20}Nb_{20}Mo_{20}Ta_{20}W_{20}$ refractory high entropy alloys, Intermetallics 19 (2011) 698–706. doi:10.1016/j.intermet.2011.01.004.

[10] E.J. Pickering, R. Muñoz-Moreno, H.J. Stone, N.G. Jones, Precipitation in the equiatomic high-entropy alloy CrMnFeCoNi, Scr. Mater. 113 (2016) 106–109. doi:10.1016/j.scriptamat.2015.10.025.

[11] F. Otto, A. Dlouhý, K.G. Pradeep, M. Kubênová, D. Raabe, G. Eggeler, E.P. George, Decomposition of the single-phase high-entropy alloy CrMnFeCoNi after prolonged anneals at intermediate temperatures, Acta Mater. 112 (2016) 40–52. doi:10.1016/j.actamat.2016.04.005.

[12] V. Maier-Kiener, B. Schuh, E.P. George, H. Clemens, A. Hohenwarter, Nanoindentation testing as a powerful screening tool for assessing phase stability of nanocrystalline high-entropy alloys, Mater. Des. 115 (2016) 479–485. doi:10.1016/j.matdes.2016.11.055.

[13] O.N. Senkov, S.V. Senkova, D.B. Miracle, C. Woodward, Mechanical properties of low-density, refractory multi-principal element alloys of the Cr–Nb–Ti–V–Zr system, Mater. Sci. Eng. A. 565 (2013) 51–62. doi:10.1016/j.msea.2012.12.018.

[14] O.N. Senkov, J.M. Scott, S. V. Senkova, F. Meisenkothen, D.B. Miracle, C.F. Woodward, Microstructure and elevated temperature properties of a refractory TaNbHfZrTi alloy, J. Mater. Sci. 47 (2012) 4062–4074. doi:10.1007/s10853-012-6260-2.

[15] O.N. Senkov, D. Isheim, D.N. Seidman, A.L. Pilchak, Development of a refractory high entropy superalloy, Entropy 18 (2016) 1–13. doi:10.3390/e18030102.

[16] J.P. Couzinié, G. Dirras, L. Perrière, T. Chauveau, E. Leroy, Y. Champion, I. Guillot, Microstructure of a near-equimolar refractory high-entropy alloy, Mater. Lett. 126 (2014) 285–287. doi:10.1016/j.matlet.2014.04.062.

[17] O.N. Senkov, S. V. Senkova, C. Woodward, Effect of aluminum on the microstructure and properties of two refractory high-entropy alloys, Acta Mater. 68 (2014) 214–228. doi:10.1016/j.actamat.2014.01.029.

[18] O.N. Senkov, C. Woodward, D.B. Miracle, Microstructure and Properties of Aluminum-Containing Refractory High-Entropy Alloys, JOM 66 (2014) 2030–2042. doi:10.1007/s11837-014-1066-0.

[19] N.D. Stepanov, N.Y. Yurchenko, V.S. Sokolovsky, M. a. Tikhonovsky, G. a. Salishchev, An AlNbTiVZr0.5 high-entropy alloy combining high specific strength and good ductility, Mater. Lett. 161 (2015) 136–139. doi:10.1016/j.matlet.2015.08.099.

[20] J.W. Yeh, Alloy design strategies and future trends in high-entropy alloys, JOM 65 (2013) 1759–1771. doi:10.1007/s11837-013-0761-6.

[21] N.D. Stepanov, D.G. Shaysultanov, G.A. Salishchev, M.A. Tikhonovsky, Structure and mechanical properties of a light-weight AlNbTiV high entropy alloy, Mater. Lett. 142 (2015) 153–155. doi:10.1016/j.matlet.2014.11.162.

[22] N.D. Stepanov, N.Y. Yurchenko, D.V. Skibin, M.A. Tikhonovsky, G.A. Salishchev, Structure and mechanical properties of the AlCrxNbTiV (x = 0, 0.5, 1, 1.5) high entropy alloys, J. Alloys Compd. 652 (2015) 266–280. doi:10.1016/j.jallcom.2015.08.224.

[23] B. Schuh, F. Mendez-Martin, B. Völker, E.P. George, H. Clemens, R. Pippan, A. Hohenwarter, Mechanical properties, microstructure and thermal stability of a nanocrystalline CoCrFeMnNi high-entropy alloy after severe plastic deformation, Acta Mater. 96 (2015) 258–268. doi:10.1016/j.actamat.2015.06.025.

[24] D. Setman, E. Schafler, E. Korznikova, M.J. Zehetbauer, The presence and nature of vacancy type defects in nanometals detained by severe plastic deformation, Mater. Sci. Eng. A. 493 (2008) 116–122. doi:10.1016/j.msea.2007.06.093.

[25] R. Pippan, S. Scheriau, A. Hohenwarter, M. Hafok, Advantages and Limitations of HPT: A Review, Mater. Sci. Forum. 584–586 (2008) 16–21. doi:10.4028/www.scientific.net/MSF.584-586.16.

[26] A.P. Hammersley, S.O. Svensson, M. Hanfland, A.N. Fitch, D. Hausermann, Two-dimensional detector software: From real detector to idealised image or two-theta scan, High Press. Res. 14 (1996) 235–248. doi:10.1080/08957959608201408.

[27] W.C. Oliver, G.M. Pharr, Improved technique for determining hardness and elastic modulus using load and displacement sensing indentation experiments, J. Mater. Res. 7 (1992) 1564–1580.

[28] V. Maier, C. Schunk, M. Göken, K. Durst, Microstructure-dependent deformation behaviour of bcc-metals – indentation size effect and strain rate sensitivity, Philos. Mag. 6435 (2014) 1–14. doi:10.1080/14786435.2014.982741.

[29] Q. Wei, S. Cheng, K.T. Ramesh, E. Ma, Effect of nanocrystalline and ultrafine grain sizes on the strain rate sensitivity and activation volume: Fcc versus bcc metals, Mater. Sci. Eng. A. 381 (2004) 71–79. doi:10.1016/j.msea.2004.03.064.

[30] K. Durst, V. Maier, Dynamic nanoindentation testing for studying thermally activated processes from single to nanocrystalline metals, Curr. Opin. Solid State Mater. Sci. 19 (2015) 340–353. doi:10.1016/j.cossms.2015.02.001.

[31] R.Z. Valiev, R.K. Islamgaliev, I. V. Alexandrov, Bulk nanostructured materials from severe plastic deformation, Prog Mater Sci. 45(2): 2000 103-189. doi:10.1016/S0079-6425(99)00007-9.

[32] M. Birkholz, Principles of X-ray Diffraction, Wiley-VCH Verlag GmbH & Co. KGaA, 2005. doi:10.1002/3527607595.ch1.

[33] M. Pouryazdan, D. Schwen, D. Wang, T. Scherer, H. Hahn, R.S. Averback, P. Bellon, Forced chemical mixing of immiscible Ag-Cu heterointerfaces using high-pressure torsion, Phys. Rev. B - Condens. Matter Mater. Phys. 86 (2012) 1–8. doi:10.1103/PhysRevB.86.144302.

[34] X. Quelennec, A. Menand, J.M. Le Breton, R. Pippan, X. Sauvage, Homogeneous Cu-Fe super saturated solid solutions prepared by severe plastic deformation, Philos. Mag. 90 (2010) 1179-1195. doi:10.1080/14786430903313682.

[35] H.W. Höppel, J. May, P. Eisenlohr, M. Göken, Strain-rate sensitivity of ultrafine-grained materials, Zeitschrift Für Met. 96 (2005) 566–571. doi:10.3139/146.101071.

[36] J. May, H.W. Höppel, M. Göken, Strain rate sensitivity of ultrafine grained fcc- and bcc-type metals, Mater. Sci. Forum. 503–504 (2006) 781–786. doi:10.4028/www.scientific.net/MSF.503-504.781.

[37] V. Maier, A. Hohenwarter, R. Pippan, D. Kiener, Thermally activated deformation processes in body-centered cubic Cr – How microstructure influences strain-rate sensitivity, Scr. Mater. 106 (2015) 42–45. doi:10.1016/j.scriptamat.2015.05.001.

[38] A. Seeger, Temperature and Strain-Rate Dependence of the Flow Stress of Body - Centered Cubic Metals: a Theory Based on Kink-Kink Interactions, Zeitschrift Fuer Met. Res. Adv. Tech. 72 (1981) 369–380.

[39] A.S. Schneider, C.P. Frick, B.G. Clark, P.A. Gruber, E. Arzt, Influence of orientation on the size effect in bcc pillars with different critical temperatures, Mater. Sci. Eng. A. 528 (2011) 1540–1547.

[40] E. Ma, T.D. Shen, X.L. Wu, Nanostructured metals: less is more., Nat. Mater. 5 (2006) 515–516. doi:10.1038/nmat1671.

[41] X. Huang, N. Hansen, N. Tsuji, Hardening by Annealing and Softening by Deformation in Nanostructured Metals, Science 312 (2006) 249–251. doi:10.1126/science.1124268.

[42] O. Renk, A. Hohenwarter, K. Eder, K.S. Kormout, J.M. Cairney, R. Pippan, Increasing the strength of nanocrystalline steels by annealing: Is segregation necessary?, Scr. Mater. 95 (2015) 27–30. doi:10.1016/j.scriptamat.2014.09.023.

[43] R.Z. Valiev, N.A. Enikeev, M.Y. Murashkin, V.U. Kazykhanov, X. Sauvage, On the origin of the extremely high strength of ultrafine-grained Al alloys produced by severe plastic deformation, Scr. Mater. 63 (2010) 949–952. doi:10.1016/j.scriptamat.2010.07.014.

[44] H.S. Kim, M.B. Bush, The effects of grain size and porosity on the elastic modulus of nanocrystalline materials, Nanostructured Mater. 11 (1999) 361–367. doi:10.1016/S0965-9773(99)00052-5.

[45] P.G. Sanders, J. A. Eastman, J.R. Weertman, Elastic and tensile behavior of nanocrystalline copper and palladium, Acta Mater. 45 (1997) 4019–4025. doi:10.1016/S1359-6454(97)00092-X.

[46] G.E. Fougere, L. Riester, M. Ferber, J.R. Weertman, R.W. Siegel, Young's modulus of nanocrystalline Fe measured by nanoindentation, Mater. Sci. Eng. A. 204 (1995) 1–6.

[47] F. Mompiou, D. Caillard, M. Legros, H. Mughrabi, In situ TEM observations of reverse dislocation motion upon unloading in tensile-deformed UFG aluminium, Acta Mater. 60 (2012) 3402–3414. doi:10.1016/j.actamat.2012.02.049.

[48] A.P. Zhilyaev, T.R. McNelley, T.G. Langdon, Evolution of microstructure and microtexture in fcc metals during high-pressure torsion, J. Mater. Sci. 42 (2007) 1517–1528. doi:10.1007/s10853-006-0628-0.

[49] C. Ng, S. Guo, J. Luan, S. Shi, C.T. Liu, Entropy-driven phase stability and slow diffusion kinetics in an Al 0.5CoCrCuFeNi high entropy alloy, Intermetallics 31 (2012) 165–172. doi:10.1016/j.intermet.2012.07.001.

[50] A. Manzoni, H. Daoud, S. Mondal, S. Van Smaalen, R. Völkl, U. Glatzel, N. Wanderka, Investigation of phases in Al23Co15Cr23Cu8Fe15Ni16 and Al8Co17Cr17Cu8Fe17Ni 33 high entropy alloys and comparison with equilibrium phases predicted by Thermo-Calc, J. Alloys Compd. 552 (2013) 430–436. doi:10.1016/j.jallcom.2012.11.074.

[51] E.J. Pickering, N.G. Jones, High-entropy alloys: a critical assessment of their founding principles and future prospects, Int. Mater. Rev. 61 (2016) 184–202. doi:10.1080/09506608.2016.1180020.

[52] F. Zhang, C. Zhang, S.L. Chen, J. Zhu, W.S. Cao, U.R. Kattner, An understanding of high entropy alloys from phase diagram calculations, Calphad Comput. Coupling Phase Diagrams Thermochem. 45 (2014) 1–10. doi:10.1016/j.calphad.2013.10.006.

[53] N.D. Stepanov, D.G. Shaysultanov, M.S. Ozerov, S.V. Zherebtsov, G.A. Salishchev, Second phase formation in the CoCrFeNiMn high entropy alloy after recrystallization annealing, Mater. Lett. 185 (2016) 1–4. doi:10.1016/j.matlet.2016.08.088.

[54] D.B. Miracle, High entropy alloys and their development as structural materials, Mater. Sci. Technol. 31 (2015) 1142–1147. doi:10.1179/1743284714Y.0000000749.

D.

Thermodynamic instability of a nanocrystalline, single-phase TiZrNbHfTa alloy and its impact on the mechanical properties

B. Schuh [a], B. Völker [a], J. Todt [b], N. Schell [c], L. Perriere[d], J.Li[e], J.P. Couzinié[d], A. Hohenwarter [a]

[a] Department of Materials Physics, University of Leoben, Jahnstraße 12, 8700 Leoben, Austria

[b] Erich-Schmid-Institute of Materials Science, Austrian Academy of Sciences, Jahnstraße 12, 8700 Leoben, Austria

[c] Institute of Materials Research, Helmholtz-Zentrum Geesthacht, Geesthacht, Germany

[d] Université Paris Est, ICMPE (UMR 7182), CNRS, UPEC, 2-8, Rue H. Dunant F-94320 Thiais, France

[e] Chair of Casting Research, University of Leoben, Franz-Josef-Strasse 18, 8700 Leoben, Austria

Abstract

An equiatomic, single-phase TiZrNbHfTa high-entropy alloy was subjected to high-pressure torsion, leading to a grain size below 100 nm. Introducing a nanocrystalline microstructure to the material should help to accelerate a possible phase decomposition of the material by having a high amount of fast diffusion pathways and possible nucleation sites in the form of grain boundaries. In order to test the materials thermodynamic stability the nanocrystalline high-entropy alloy was subjected to various heat treatments for temperatures between 300°C and 1100°C. Isochronal heat treatments (1h) resulted in a hardness increase from 420 HV1 for the as-processed state to 530 HV1 for an annealing temperature of 500°C, while for temperatures of 700 °C and higher a softening compared to the as-processed state occurred. In order to clarify this unexpected annealing response, analysis of selected microstructural states was performed utilizing electron microscopy, x-ray diffraction as well as mechanical testing to gain further information on microstructure-property relationships. Complementary, thermodynamic simulations were performed via the Calphad approach and compared to the experimental results. A phase decomposition of the originally equimolar single-phase high-entropy alloy into a NbTa-rich body-centered cubic phase and ZrHf-rich phases, which occurred in two different crystal structures depending on the annealing temperature, was the main reason for the property changes. The obtained results not only give valuable new insights into the phase stability of the

TiZrNbHfTa alloy, but also demonstrate the impact of the newly forming phases in regards to mechanical properties and its implication for a possible practical application of this alloy.

D.1 Introduction

High-entropy alloys (HEAs) are multi-principal element alloys, most commonly defined as having at least five different alloying elements varying in chemical composition from 5 at% to 35 at% [1,2]. Recently, multi-principal element alloys that do not strictly satisfy the single-phase definition are also regarded as compositionally complex alloys (CCAs) [3].

Among the large number of HEAs proposed in the last years, some show outstanding mechanical properties, such as the face-centered-cubic (fcc), equiatomic CrMnFeCoNi alloy [4–6]. Despite having a high tensile strength, it still remains highly ductile even at very low testing temperatures. Additionally, it also has an exceptionally high fracture toughness, making it a potential candidate for low temperature applications in future [6].

Among body-centered-cubic (bcc) HEAs, potential applications are found in the high temperature regime [7–10]. Frequently proposed reasons for this are two of the so called "core-effects" of HEAs. Firstly, there is a severe lattice distortion [11,12], which should lead to an inherently high strength due to strong solid solution hardening, especially in bcc HEAs [13]. The second reason is the sluggish diffusion effect, caused by the fluctuations in the potential energy of sites due to changing bonding configurations with different neighbouring elements, giving rise to some especially deep diffusion traps [12,14–16]. It should be noted, however, that both of these "core-effects" are still controversially discussed in the literature. For instance, recent neutron scattering experiments showed that the crystal lattice is not abnormally distorted in the CrMnFeCoNi alloy [17] and the sluggish diffusion effect is, so far, mostly based on indirect observations, such as slow grain growth. [3,16] A prominent example for a single-phase bcc HEA after casting and homogenization at high temperatures is the quinary TiZrNbHfTa system composed of 20 at% of each element, which has been well characterized in regards to mechanical properties and underlying deformation mechanisms for coarse-grained microstructures [18–23]. Its compression ductility exceeds 50 % [18], placing it among the most ductile bcc HEAs, which often show poor cold deformability [7,9,24]. The alloy's high yield strength and strain hardening in compression tests is also retained up to temperatures of 600 °C. For much higher temperatures (≥1000 °C) the onset of dynamic recrystallization and consequently a drop-off in the yield strength and steady-state flow have been reported [19]. However, it was also recently demonstrated by Senkov et al. that the single-phase structure is likely only the equilibrium condition at temperatures higher than 800 °C and that for lower temperatures the single-phase structure might only be retained due to slow diffusion kinetics [25]. Similar results were also obtained for the CrMnFeCoNi alloy, which was believed to be a thermodynamically stable single-phase high entropy alloy as well [26–29]. In general, no investigations into the ultra-fine grained or nanocrystalline (nc) grain size regime and its impact on the mechanical performance of the TiZrNbHfTa alloy have been conducted so far, to the best of the author's knowledge.

A pragmatic way to determine the formation of additional phases in HEAs, especially at lower annealing temperatures without requiring extensive annealing times, is to introduce fast diffusion pathways in the form of grain boundaries [26,30]. Another advantage of having a very fine-grained microstructure is that it reduces the need for site-specific investigations, since even a small sample volume is representative for the overall microstructure. Therefore investigations of possible phase decompositions have also

transitioned to the nc grain size regime. For instance, for the CrMnFeCoNi alloy a phase decomposition of the single-phase fcc material into a multi-phase microstructure occurs much faster for nc structures compared to coarse-grained ones [26–29]. A potent way to achieve nc microstructures is high-pressure torsion (HPT), which allows deformation even for relatively brittle materials at room temperature [31].

Consequently, in this study an equiatomic TiZrNbHfTa alloy was processed by HPT to induce a nc microstructure. These samples then were subjected to various heat treatments in order to evaluate the thermodynamic stability of this alloy. The resulting microstructures were investigated by electron microscopy as well as by synchrotron x-ray diffraction (XRD) and complementary mechanical testing via microhardness and tensile testing was performed. Additionally, thermodynamic simulations were conducted using the Calphad (CALculation of PHAse Diagrams) approach and compared to experimental data. The obtained results give a comprehensive overview of the microstructural stability of the TiZrNbHfTa alloy and the impact of possible phase decompositions on the mechanical properties of the material in the nanocrystalline grain size regime.

D.2 Experimental

The studied alloy was prepared as described elsewhere [32]. Two mother alloys (TiZrHf and NbTa) were first melted twice by arc melting under Ar atmosphere. The final composition was obtained by mixing the two mother alloys first by arc melting, then by induction melting under He atmosphere in a Cu cold crucible to insure chemical homogeneity. Shaping of the ingot as a 8 mm diameter, 60 mm long rod was obtained through a last step by arc melting. The thickness was then reduced down to 0.8 mm by cold rolling. The final grain size was controlled by a heat treatment at 1100°C for 5h under He atmosphere. The material in this state will be referred to as “as-received” in the text.

Subsequently disks with 8 mm in diameter and a thickness of 0.8 mm were machined from the as-received material and deformed by quasi-constrained HPT for up to 5 rotations. Processing was performed at room temperature with a pressure of 7.8 GPa and a rotational speed of 0.2 rotations/minute. Detailed information on this processing technique can be found in [33]. For HPT processing the ideal shear strain γ can be calculated using Equation D.1, where r is the sample radius, t the sample thickness and n the number of rotations [33].

$$\gamma = \frac{2\pi rn}{t} \ (-) \qquad \textbf{Equation D.1}$$

For a shear strain of about 40, which is equivalent to a radial position of ~ 1 mm after 5 rotations, the material reaches a microstructural equilibrium. At this stage microstructure features such as grain size and percentage of high-angle grain boundaries no longer change even if the strain is increased further. Samples that have reached this equilibrium or “steady-state” condition are then subjected to isochronal (t = 1h) heat treatments for temperatures between 300°C and 1100°C or isothermal (T = 500°C) heat treatments for annealing times ranging from 5 minutes to 100 hours.

For hardness testing the samples were ground mechanically with SiC paper and then mechano-chemically polished (OPS). Hardness testing was performed with a microhardness tester Micromet 5104 from Buehler, at a load of 1000gf with 15 seconds of dwell time. For investigations via scanning electron microscopy (SEM) samples were additionally polished with an OPS solution from Struers for 4 hours utilizing a Bühler VibroMet 2. Samples for transmission electron microscopy (TEM) were taken from edge

regions of the HPT disks in axial viewing direction (onto the top of the disk), then first ground down to 100 µm, subsequently mechanically dimpled to about 10 µm and finalized using Ar ion-milling. Investigations of the microstructure were performed both by SEM (Zeiss 1525) and TEM (Philips CM12/ JEOL 2100F). The Philips CM12 was mainly utilized for bright-field imaging and for obtaining electron diffraction patterns. An image-side Cs-corrected JEOL 2100F was further used for scanning-TEM (STEM) imaging as well as energy-dispersive x-ray (EDX) measurements. To gain additional microstructural information synchrotron XRD measurements were done. The measurements were performed using a beam energy of 87.1 keV at the beamline P07/HEMS of the PETRA III synchrotron within the DESY Photon Science facility. Detector geometry calibration was performed using LaB_6 as a reference material. For data analysis two software packages were used, FIT2D [34] and Match! [35] as well as several crystallography databases, including the Crystallography Open Database, PDF-2 and the Inorganic Crystal Structure Database.

Tensile samples were prepared by a newly developed grinding tool to manufacture miniaturized, circular tensile samples [36]. The preform of the tensile samples were HPT disks cut in half, therefore the dimensions are: a length of 8 mm, a maximum width of 4 mm and 0.8 mm in thickness. The center of the tensile specimen's gauge length was situated at a radius of 2 mm of the former HPT disk. Tensile samples had a cross sectional diameter of approximately 500 µm and a gauge length of 2.5 mm and at least 4 samples were tested per investigated microstructural state. Tensile tests were performed at room temperature in a tensile testing machine from Kammrath and Weiss using a 2 kN load cell and a crosshead speed of 2.5 µm/s. During testing a commercial single-lens camera was used to record up to 3.1 frames/s. All data then was evaluated by using automated digital image correlation utilizing the MatLab [37] software package. All further details on specimen production, tensile testing and data evaluation can be found in reference [36].

CALPHAD modelling was used to describe the temperature-dependent evolution of the phases (mole/mass fraction, compositions) for the TiZrNbHfTa system. The approach considers the calculation of thermodynamic properties and also phase diagrams by extrapolation of binary systems descriptions. Simulations were performed with the TCHEA1 database, which was introduced by Thermo-calc [38] and especially developed for high-entropy alloys. TCHEA1 has been recently used for CoCrFeMnNi, MnFeNiCuPt and MnFeNiCuCo multi-component systems [39,40].

D.3 Results

D.3.1 Characterization of the as-received material and processing

The as-received material was first studied by means of electron back-scatter diffraction (EBSD) and EDX measurements. Figure 1a) shows that the as-received state has a homogenous, coarse-grained microstructure with an average grain size of ~ 100 µm. The equiatomic character of the alloy was verified by averaging 100 individual EDX measurements performed in a line scan, see inset in Figure 1a). According to literature, the TiZrNbHfTa alloy in this microstructural state should be a single-phase bcc alloy, which was verified by XRD measurements (not displayed in the present paper) and all performed EBSD scans only indicated the presence of a bcc phase. The lattice constant of the TiZrNbHfTa alloy was determined to be 341.9 pm, which is in good agreement with published data [18,32].

The evolution of the microstructure and hardness as a function of the shear strain γ during HPT processing is presented in Figure 1 b)-e). Hardness values were obtained by averaging four indents at an equivalent radial position, the standard deviation is indicated by the error bars (Figure 1b)). The coarse-grained, as-received material has a hardness of 309 ± 6 HV1. The hardness increases with increasing strain up to about 419.4 ± 2.5 HV1 for γ ~ 40, for higher shear strains a plateau is reached.

Figure 1c) – e) depict back-scatter electron (BSE) micrographs illustrating the microstructural changes during shear deformation. Figure 1 c) shows a near center region of a sample after ¼ of a rotation. At such low applied shear strains (γ ~ 1) the formation of dislocation substructures, as often observed during HPT processing, can be evidenced [33]. Additionally, the deformation starts to localize into bands, in which the microstructure is significantly more refined than in the surrounding material. This strong localization in grain refinement is also the cause for the relative large standard deviation regarding the materials hardness at low applied shear strains. With increasing shear strain γ, the number of deformation bands increases as well (Figure 1d) and Figure 1e)). For very high shear strains of γ > 40 a steady state microstructure is reached, due to an equilibrium in the generation and annihilation of defects caused by the ongoing deformation and dynamic recovery processes. This microstructural state is homogenous with nanocrystalline, equiaxed grains. This saturation in grain refinement is also reflected in the hardness reaching a plateau at this point, see Figure 1b).

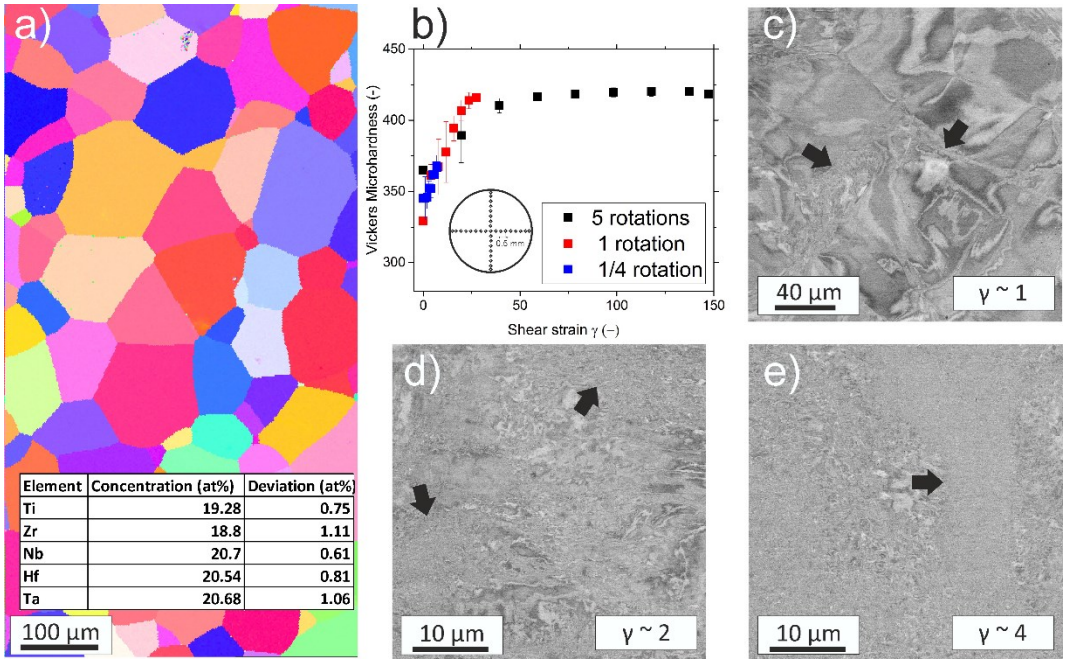

Figure 1: a) Microstructure of the coarse-grained, as-received state. In the inset the average chemical composition determined by an EDX line scan can be seen. b) Evolution of hardness as a function of shear strain during HPT processing. For γ larger than 40 a saturation in hardness is achieved. c)-e) BSE images of the microstructure development at relatively low shear strains. c) At γ close to 1 the typical formation of dislocation substructures as well as the onset of a localization of deformation (see arrows) can be observed. d) and e) show an increase in the number of deformation bands with an increase in shear strain.

D.3.2 Characterization of the HPT processed material

The severely deformed material ($\gamma > 40$), which has reached the steady-state regime was subsequently characterized by TEM and STEM imaging in more detail. Figure 2 a) depicts a nc microstructure with rather blurry boundaries, which is characteristic for many HPT processed materials and typically attributed to the formation of non-equilibrium grain boundaries during processing [41]. Since boundaries are often difficult to discern for this microstructural state, the grain size estimation in the processed material bears difficulties, but based on a large number of dark-field images the average grain size of the TiZrNbHfTa material in the steady-state regime can be estimated to be close to 50 nm. In the inset of Figure 2 a) a corresponding electron diffraction pattern can be seen. Since all Debye Scherrer rings can be attributed to one bcc phase with a lattice constant of 340.2 pm, the TiZrNbHfTa alloy apparently retains its single phase character during HPT processing. This could also be confirmed by complimentary measurements via XRD for which a lattice constant of 341.1 pm was determined, see Figure 2b).

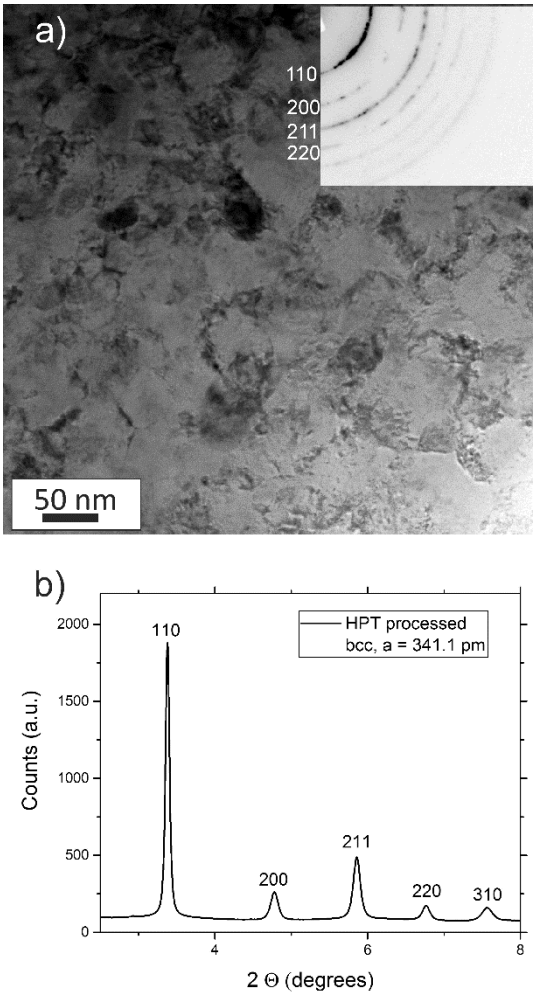

Figure 2: a) STEM image of the steady-state microstructure of the TiZrNbHfTa alloy after being subjected to shear strains larger than 40. The inset is a corresponding electron diffraction pattern, showing that the material retains its single-phase bcc character during HPT deformation. b) This was also confirmed via synchrotron XRD measurements.

D.3.3 Annealing response of the HPT processed TiZrNbHfTa alloy

The TiZrNbHfTa alloy in the steady-state condition after HPT processing was subsequently isochronally annealed for 1h at temperatures between 300°C and 1100°C, Figure 3a). Even for very low annealing temperatures of only 300°C the hardness of the material increases markedly by about 60 HV1 and continues to increase further with higher annealing temperatures up to 500°C, for which a maximum hardness increase of more than 110 HV1 is reached. At higher heat treatment temperatures (T>500°C) the hardness decreases quickly.

In order to get better insights into the kinetics of this hardening process additionally isothermal anneals at the peak hardness temperature of 500°C were performed. The majority of the hardening occurs within very short time spans, as can be seen in Figure 3 b). After 5 minutes of annealing the hardness increases by approximately 80 HV1 to 499 ± 6 HV1. For isothermal annealing the maximum hardness is again reached for 1h of heat treatment, longer annealing times lead to moderate decreases in the materials hardness.

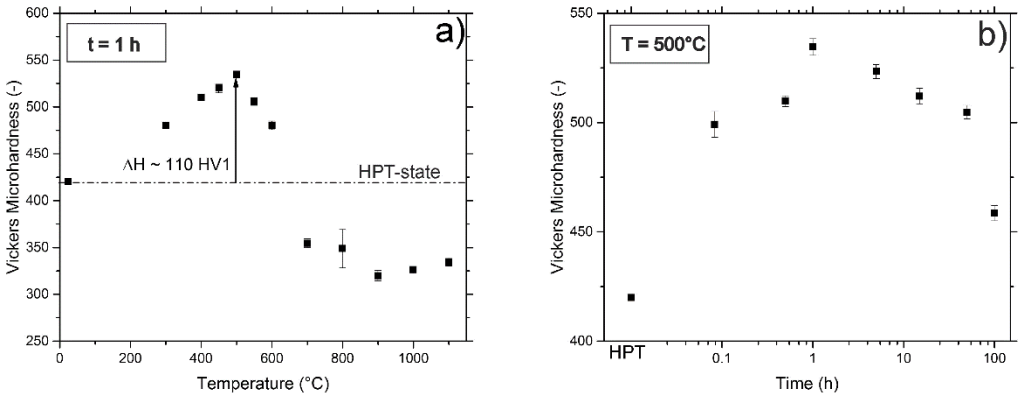

Figure 3: a) Isochronal annealing treatments performed for 1h lead to an increase in hardness up to annealing temperatures of 600°C. b) Isothermal heat treatments at 500°C reveal that a significant portion of the hardening occurs within very short times spans of just 5 minutes.

In order to gain additional information on the microstructural response to the heat treatment, three annealed samples, namely 500°C for 1h and for 100h as well as 800°C for 1h, were complementarily investigated by TEM.

Figures 4 a) and b) show the microstructure after a heat treatment at 500°C for 1h. During annealing the non-equilibrium grain boundaries of the HPT processed state rearrange to a more equilibrium-like state. Microstructural features seem therefore a lot clearer compared to the as-deformed state. Complementary imaging via high-angle annular dark field (HAADF) was performed along with additional EDX measurements, see Figure 5 a) and b). The lighter and darker grains visible in Figure 4 a) and 4b), could be correlated to a Nb-Ta (bcc, according to the electron diffraction pattern inset) and Zr-Hf (hcp) enriched phases, respectively.

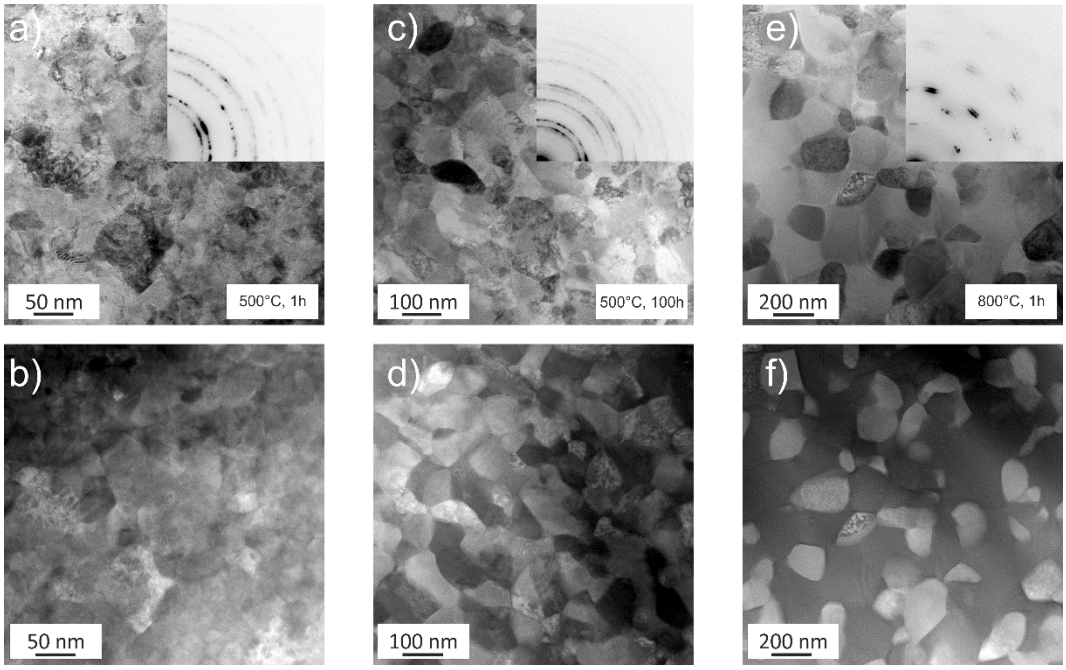

Figure 4: a) Bright field image of a specimen annealed at 500°C for 1h and b) a HAADF image of the same position, showing a two-phase microstructure. c) and d) for longer annealing times of 100 h grain coarsening occurs, but no additional phases compared to the 1h state can be detected. e) and f) after an annealing treatment at 800°C for 1h the microstructure is still ultra-fine grained and shows a phase decomposition of the bcc high entropy phase. The insets in a), c) and e) show corresponding electron diffraction patterns.

Prolonged annealing at 500°C for 100h leads to further grain growth (Figure 4 c)) and d)), but no additional phases form. However, with longer annealing times the chemical compositions of the present phases changes markedly compared to the 500°C, 1h specimen, see Figure 5 a) and c). After the isochronal annealing treatment at 800°C (Figure 4 e)) and f)) the sample still has a grain size in the sub-micron regime. Looking at the electron diffraction pattern (inset of Figure 4 e)) and EDX measurements (Figure 5 e)), it can be seen that a second Zr-Hf rich phase with a bcc crystal structure and a lattice constant of approximately 356 pm is occurring at higher temperatures instead of the Zr-Hf rich hcp phase. The Nb-Ta rich phase retains its bcc character, with a lattice constant of about 342 pm.

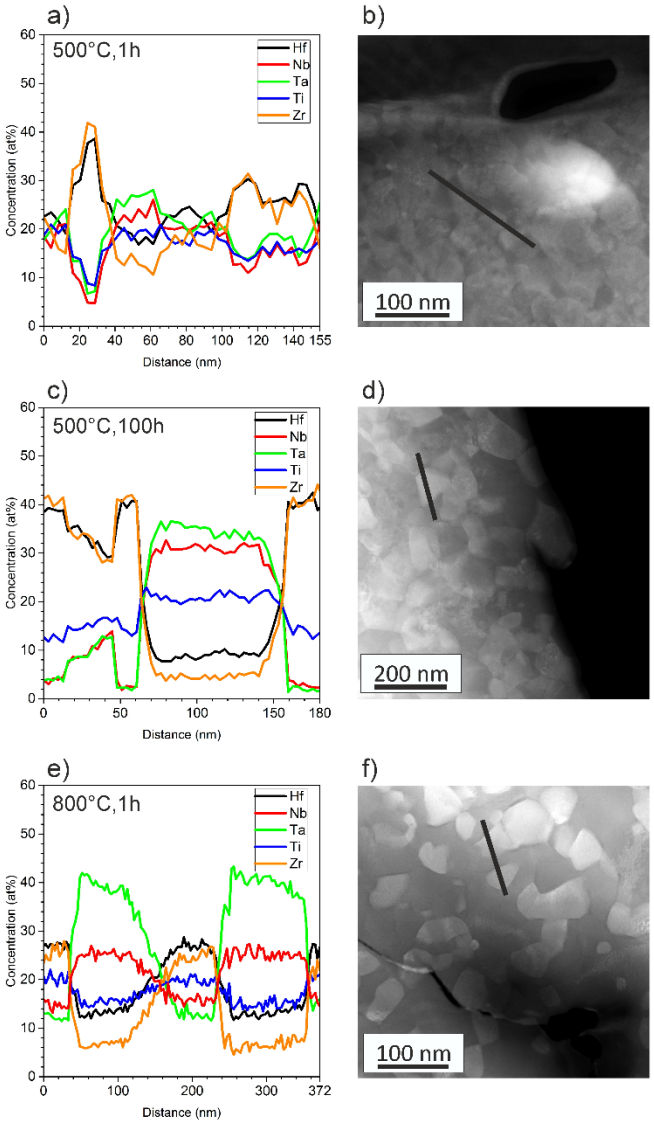

Figure 5: EDX line-scan data (a), c) and e)) of the annealed specimens, show the changes in the chemical composition occurring during the phase decomposition, while the HAADF images show the location, where the scans where performed (b), d) and f)). a) Sample annealed at 500°C for 1h. The hcp phase (darker regions in the HAADF image b)) is clearly enriched in Zr and Hf, while differences in chemistry in the bcc phase (Nb-Ta) are not that pronounced yet. c) For longer annealing times (t=100h) at 500°C the changes get more pronounced and the bcc phase (lighter regions) is much richer in Nb and Ta. e) At 800°C for 1h phases enriched in Nb-Ta and Zr-Hf occur as well.

Samples that were annealed at higher temperatures were subsequently investigated via BSE imaging in the SEM. For heat treatment temperatures of 900°C the microstructure is partially recrystallized, with some grains significantly growing in size, while other grains are pinned by fine grain boundary precipitates (Figure 6a)). Annealing at even higher temperatures leads to a single-phase microstructure, while further grain growth occurs, see Figure 6 b) and c). Grain sizes for samples annealed at 1000°C for 1h and 1100°C for 1h are close to 25 µm and 50 µm as determined by EBSD scans (area-weighted, not shown in the present manuscript).

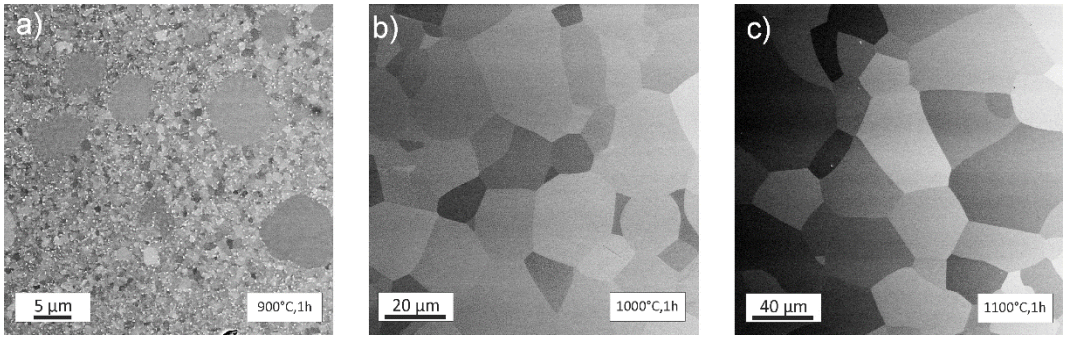

Figure 6: BSE images of samples annealed for 1h at a) 900°C, b) 1000°C and c) 1100°C. Samples at 900°C show an inhomogeneous microstructure, where some grains have grown, while others still remain fine-grained with second-phase precipitation occurring at the grain boundaries. Samples at higher temperatures, see b) and c), have recrystallized and the only phase occurring is the original bcc high-entropy phase.

Samples annealed for 1h in a temperature range from 300°C to 1100°C additionally were investigated by means of synchrotron XRD-measurements in order to obtain microstructural information on a much larger sample volume compared to a TEM specimen. In Figure 7a) a large range of 2Θ angles featuring many peaks is displayed, while Figure 7b) focuses on the immediate region around the (110) peak of the original bcc high-entropy phase in order to better highlight the occurring changes. For the 300°C sample no distinct changes compared to the as–deformed sample can be detected, all peaks still correspond to a single-phase bcc material. However, the 500°C annealed specimens clearly show a decomposition of the bcc-high entropy phase into two different phases, where one still has a bcc crystal structure with a slightly diminished lattice constant of about 335.4 pm. The second phase on the other hand has a hcp structure with the lattice parameters of a = 318.7 pm and c = 506.7 pm, close to the lattice constants of pure Hf.

Additional measurements were performed for a sample annealed at 500°C for 100h, which show that for longer annealing times the hcp-related peaks start to become more pronounced. Compared to the specimen annealed at 500°C for 1h, the peak positions shift slightly, indicating a change in the lattice parameters occurring for longer annealing times. Since with longer annealing times the defect density in the material is reduced, the peak broadening is reduced as well. This is in good agreement with the prior TEM investigations, where a Nb-Ta rich bcc and a Zr-Hf rich hcp phase were observed for these annealing states.

The specimen annealed at 800°C for 1h is likely containing three different phases. The disordered bcc phase is still present, however a change in peak positions is occurring (the lattice constant now is 334.5 pm). Besides this bcc phase, two more phases occur, another disordered bcc phase as well as small amounts of a hcp phase – The diffraction peaks of these 2 phases are partially overlapping. However, no hcp phase could be found for the 800°C, 1h annealing state utilizing TEM, see Figure 4 e) and f), likely due to this phase occurring at a low volume fraction at this point.

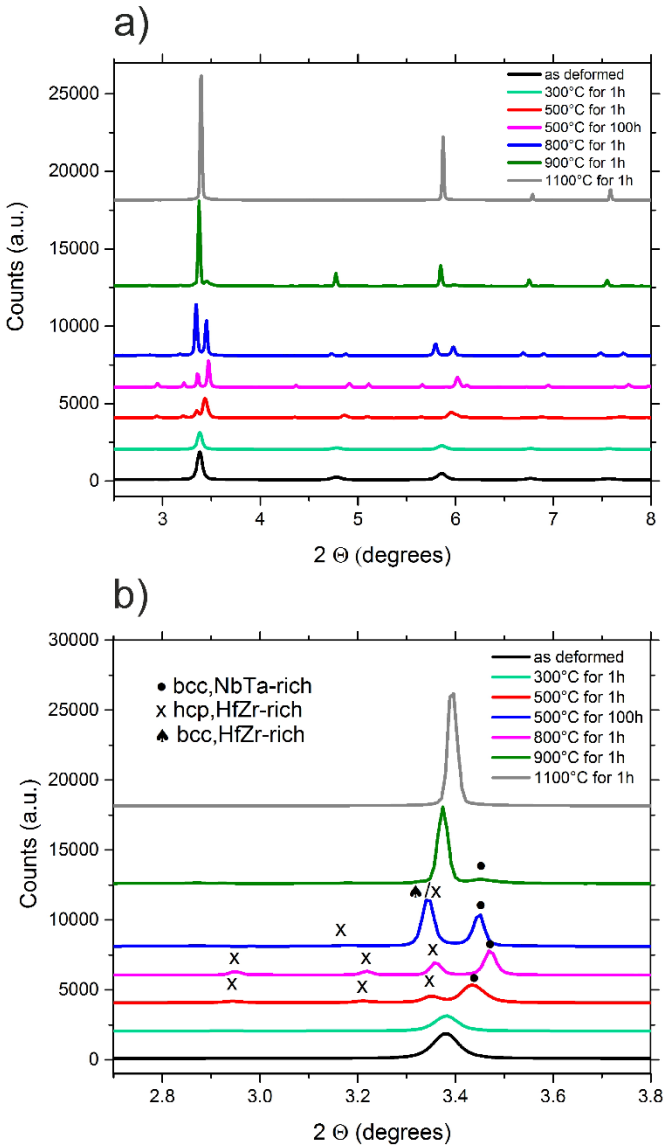

Figure 7: a) Synchrotron XRD data of the HPT deformed and subsequently annealed material. For 500°C a phase decomposition of the single-phase HEA into a bcc and hcp phase can be detected. At 800°C two bcc and one hcp phase are present. b) Detailed view of a) over a reduced 2Θ range. The additional information on the chemistry was obtained by TEM investigations.

A summary of these findings can be found in Table 1.

Microstructural State	Occurring Phases		
SPD	High-entropy bcc phase, a = 341.1 pm		
300°C, 1h	High-entropy bcc phase , a = 340.1 pm		
500°C, 1h	NbTa rich bcc, a = 335.5 pm	ZrHf rich hcp , a = 319.8 pm , c = 506.7 pm	
500°C, 100h	NbTa rich bcc, a = 335.4 pm	ZrHf rich hcp, a = 318.7 pm, c = 506.7 pm	
800°C, 1h	NbTa rich bcc, a = 334.5 pm	ZrHf rich bcc, a = 344.9 pm	ZrHf rich hcp, a = 322.8 pm , c = 511.5 pm
900°C, 1h	bcc , a = 333.9 pm	bcc, a = 341.6 pm	
1100°C, 1h	High-entropy bcc phase, a = 340.1 pm		

Table 1: Phases occurring in different microstructural states as determined via TEM and XRD investigations. For the 900°C, 1h annealing state no complimentary TEM analysis was made.

D.3.4 Thermo-Calc simulation

Thermodynamics results from the Calphad modelling are given in Figure 8. From the obtained simulations, the equimolar TiZrNbHfTa alloy seems to be thermodynamically stable as a single-phase disordered bcc alloy denoted BCC_B2#2 (Figures 8 a) and b)) for temperatures of about 1020°C up to its solidus temperature. Below 1020°C the single-phase state is no longer thermodynamically favourable and decomposes into a multi-phase structure. Two bcc phases co-exist between 800 and 1020°C (BCC_B2#1 and BCC_B2#2). With decreasing temperature in this two-phase region, the original equimolar BCC_B2#2 phase is significantly enriched in Hf and Zr and to a smaller amount in Ti whereas the new BCC_B2#1 is predicted to contain predominantly Ta and Nb (Figures 8 c) and d)).

For temperatures between 800°C and 700°C the equilibrium condition is calculated to be a 3-phase state, where in addition to the two phases mentioned above a hcp (HCP_A3#1) phase is present, which is also relatively rich in Zr and Hf (Figure 8 e)). Below 700°C the original high-entropy BCC_B2#2 phase is no longer thermodynamically stable and the microstructure consists of BCC_B2#1 and HCP_A3#1. For low temperatures the B2#1 phase gets progressively richer in Ta and Nb until it consists of 50 at% each. The HCP_A3#1 phase remains fairly constant in Hf and Zr content at around 35 at%, with some small fluctuations, while the Ti content increases continually for temperatures below 800°C. Overall, these calculations reflect the experimental findings very well. A comparison of the phase composition between simulation and experiment can be found in Table 2.

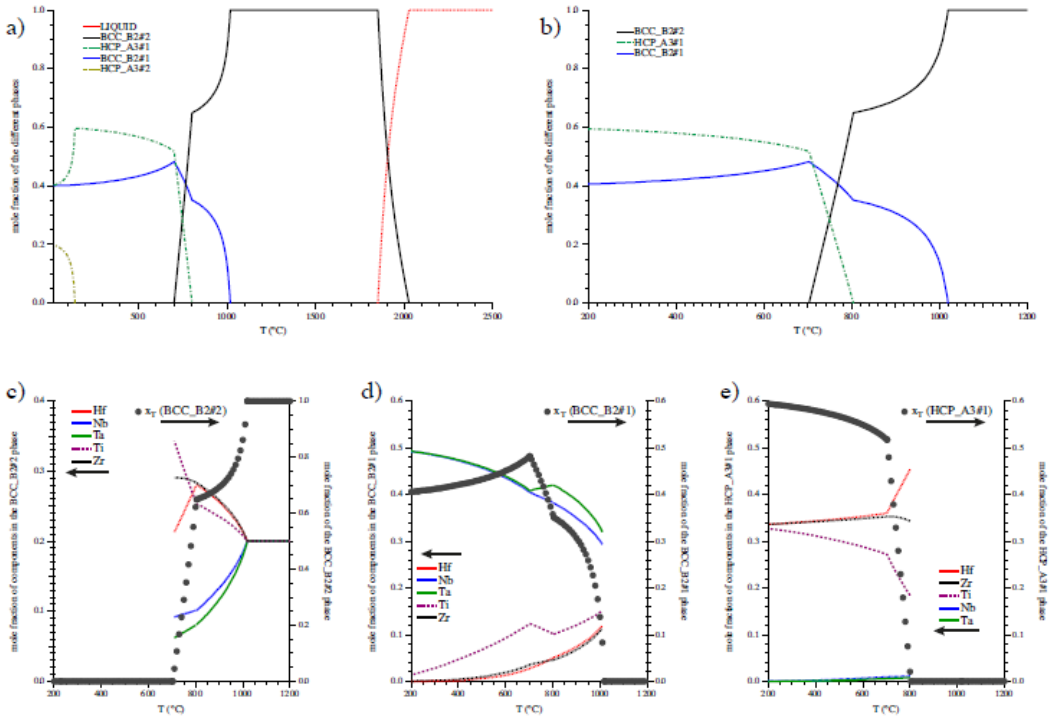

Figure 8: Calphad simulations of the TiZrNbHfTa alloy with the TCHEA1 database: a) evolution with temperature of the mole fraction of the stable phases; b) zoom of the 200-1200°C range of a); Evolution of the composition for the different phases (left axis) for BCC_B2#2 (c), BCC_B2#1 (d) and HCP_A3#1 (e). The mole fraction is given on the right axis. All the solid phases (BCC_B2#1, B2#2, HCP_A3#1, A3#2) are disordered.

		T=500°C		T=800°C		
		BCC_B2#1	HCP_A3#1	BCC_B2#1	BCC_B2#2	HCP_A3#1
Mole Fraction (%)		43.27	56.73	35.75	62.18	2.07
Mass Fraction (%)		47.84	52.16	39.13	58.7	2.16
Chemical composition	Hf	0.6	**34.8**	4.98	**27.79**	**45.37**
		(10.74)	**(37.7)**	(14.94)	**(26.4)**	**(-)**
	Nb	**45.69**	0.41	**38.3**	10.11	1.11
		(29.23)	(5.39)	**(24.14)**	(15.5)	(-)
	Ta	**45.94**	0.22	**41.98**	8	0.79
		(32.22)	(5.07)	**(36.11)**	(13.38)	(-)
	Ti	6.8	**30.07**	10.19	**25.69**	18.4
		(20.89)	**(14.26)**	(16.06)	**(20)**	(-)
	Zr	0.97	**34.52**	4.54	**28.41**	**34.34**
		(6.92)	**(37.91)**	(8.74)	**(24.4)**	**(-)**
		at. %	at. %	at. %	at. %	at. %

Table 2: Mole fraction and composition of the system at 500°C and 800°C taken from Calphad simulations (TCHEA1 base). The values in the brackets are experimental data, obtained via EDX line scans, for comparison (data from 500°C, 100h and 800°C, 1h annealed specimens). Bold numbers indicate the major elements forming the phase.

D.3.5 Impact on mechanical properties

In order to determine the influence of HPT processing and subsequent annealing treatments on the mechanical properties of the TiZrNbHfTa alloy, tensile tests were performed (Figure 9a)). The as-received state has a relatively low tensile strength of about 830 MPa with a moderate ductility, and a total elongation to failure of about 9%. The corresponding fracture surface can be seen in Figure 9 b). Grain refinement via HPT processing leads to a significant increase in the materials strength, the tensile strength of the HPT samples is around 1900 MPa. More surprisingly, despite the large increase in strength, the specimens remain fairly ductile with a total elongation to failure of 7.9%. Annealing treatments and the ensuing phase decomposition heavily impact the mechanical properties as well. Upon annealing the material at 500°C for 1h shows a strong decrease in ductility and tensile samples, while still having high strength (~ 1500 MPa), fail without much prior plastic deformation. At higher annealing temperatures of 800°C some of the ductility is restored but at the cost of a significant loss in strength, with the tensile strength being decreased to roughly 795 MPa. All mechanical properties are summarised in Table 3, where the reduction in the cross-sectional area of the tensile specimen during testing was added as an additional measure of ductility.

These changes are also reflected in the fracture surfaces – While the HPT processed sample shows a dimple fracture, which is characteristic for ductile fractures, see Figure 9 c), after annealing at 500°C for 1h, the samples fractures in an intercrystalline fashion, Figure 9 d). Ductility is regained for heat treatments at 800°C, as can be seen in Figure 9 e).

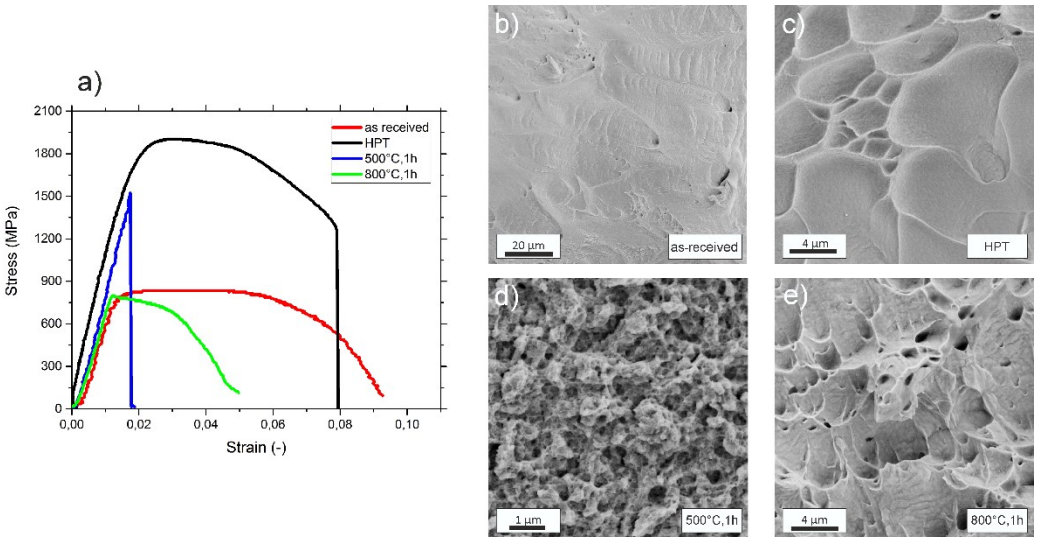

Figure 9: a) Tensile stress-strain curves of the TiZrNbHfTa alloy in different microstructural states. b)-e) secondary electron images of fractured tensile samples. b) shows the ductile fractures surfaces of the as-received material. c), after HPT processing the specimens still shows a dimple fracture. After annealing the samples at 500°C the fracture mode changes to an intercrystalline fracture, d). e) increasing the annealing temperatures further leads to a recovery of ductility.

Microstructural State	Tensile strength (MPa)	Total elongation to failure (%)	Reduction of area (%)
as-received	830	9.2	69
HPT	1900	7.9	49
500°C,1 h	1520	1.7	5
800°C, 1 h	795	5.0	67

Table 3: Summary of mechanical properties obtained during tensile testing.

D.4 Discussion

D.4.1 Microstructural changes during HPT processing

Reports are available on the deformation mechanisms present in the TiZrNbHfTa alloy in the case of a coarse-grained microstructure for relatively low deformation strains. Senkov et al. [19] reported on simultaneous dislocation and twinning activity during compression testing at room temperature of the cast alloy and concluded this to be a likely reason for the good compression ductility of TiZrNbHfTa. Later investigations also revealed extensive deformation banding after cold rolling, with bands having a certain inclination with respect to the rolling direction [25]. Studies of the compressive properties of TiZrNbHfTa after casting with in-depth TEM investigations showed that work hardening can be separated into three distinct stages and came also to the conclusion, that for larger plastic strains a localization of the deformation occurs [20]. Contrary to the study by Senkov et al. [19] no evidence of twinning could be found in reference [23]. Rather, an inhomogeneous microstructure for low strains due to an early onset of shear banding, is reported, which becomes more homogenous at higher strains.

The results obtained in this study are in line with the existing results in literature. If the sample is only subjected to relatively low shear strains, the formation of dislocation cells can be observed via BSE imaging (Figure 1c)) but also lenticular or lamellae-like structures are seen, as already reported in the references [19,21]. Senkov et al. [19] first described these structures as a mixture of shear bands and deformation twins. However in this present study, despite similar structures occurring, no conclusive proof could be found, that they are related to mechanical twinning, similar to observations in [22,23].

With increasing shear strain the deformation then quickly localizes into bands, which also drastically increase in number with increasing strain. Since a higher degree of deformation is realized inside of these deformation bands, the grain refinement is much more pronounced there than in the surrounding material. The microstructure is therefore rather inhomogeneous during early stages of deformation, but for very high strains and the steady-state regime the microstructure-homogeneity is restored. A similar deformation behavior during HPT processing has also been seen for another bcc HEA, AlTiVNb [30].

D.4.2 Evolution of hardness after heat treatments

After the isochronal (t=1h) anneals at low temperatures up to 600°C a distinct increase in the material's hardness can be detected. Even for the lowest annealing temperature of 300°C, for which no precipitation of second phases could be detected by means of XRD, a hardness increase of about 60 HV1 was measured, see Figure 3a). For nc metals several studies report a hardness increase occurring during low temperature annealing. The origin of this phenomenon is still controversially discussed [42–45]. The occurring change in hardness is often ascribed to a change in the defect structure of the material during annealing. Since in nc metals there is an abundance of grain boundaries, which act not only as dislocation sources but also as sinks and enable rapid dislocation annihilation during the annealing treatment. This might require the activation of new dislocation sources if plastic deformation is to be realised after the heat treatment, needing higher stresses compared to the as-deformed state [42,46]. Other explanations consider grain boundary-dislocation interactions as the main reason for the observed hardening. Annealing might cause an elevated concentration of solutes at the grain boundaries, which subsequently could suppress the emission of dislocations due to solute drag [44]. At slightly higher annealing temperatures the onset of a phase decomposition is observed and the formation of a multi-phase microstructure could also possibly lead to an increase in hardness. However, given the low hardness and strength of the 800°C annealing state (Figures 3 a) and 9 a)), in spite of having a fine-grained multi-phase microstructure (Figure 4 e)), this idea can be questioned. The reason for the low strength of the 800°C annealing state is most likely twofold. Firstly, a strong decrease in solid solution hardening due to the occurring phase decomposition. Senkov et al. [18] estimated the contribution of solid solution hardening in the TiZrNbHfTa alloy [47]. Since conventional models for solid solution strengthening are usually based on "dilute" alloying systems, where the solvent element and the solute elements can be clearly distinguished, in the case of the equiatomic TiZrNbHfTa a pseudobinary solid solution was assumed. Due to the very low atomic size difference Ta, Nb and Ti were considered the solvent, while Hf and Zr where thought of as the solute. A majority of the contribution to the solid solution strengthening due to atomic size misfit is therefore arising from the misfit between Ta-Nb-Ti and Hf-Zr, while the misfit and thus the strengthening contribution within Ta-Nb-Ti and Hf-Zr is negligible. The second contribution to solid solution strengthening is the elastic modulus difference and is by far the largest around Ta atoms in the TiZrNbHfTa alloy and comparably small between all other elements [18]. However, annealing at 800°C leads to a phase decomposition into Nb-Ta and Zr-Hf rich phases, thus leading to a strong reduction in the strength contribution via atomic size misfit, since both phases mostly contain elements between which the size difference is small. Secondly, while the 800°C annealing state might still possess an ultra-fine grained microstructure, the hardening contribution due to grain refinement is not that distinct in the TiZrNbHfTa alloy. As can be seen in Figure 1b), reducing the grain size in the coarse-grained as received state with a grain size of about 100 µm down to about 50 nm in the SPD processed state only leads to a hardness increase of ~ 110 HV1 (~ 35% hardness increase, compared to the as-received state). This is different to other single-phase bcc metals, such as chromium [48], where reducing the grain size from about 10 µm to approximately 250 nm for instance, leads to a roughly threefold increase in hardness.

In order to explain quantitatively the hardness and strength of the 800°C, 1h annealing state, the two main phases occurring in this microstructural state were reproduced according to the chemical information obtained by EDX line-scans in the TEM (Figure 5e)) and then subjected to HPT processing. Both phases show a similar hardness after casting (~ 280 HV1 for the ZrHf-rich phase and ~ 268 HV1for the NbTa-rich bcc phase). Introducing a nanocrystalline microstructure via HPT and subsequent hardness testing

reveal, that the hardening due to grain refinement is not pronounced, especially in the Zr-Hf phase (~ 31% hardness increase, ~79% for the Nb-Ta-rich phase), see Table 4.

Phase	Microstructural State	Vickers Microhardness (-)
Zr-Hf-rich	As-cast	280.5 ± 11.9
	HPT processed	367.2 ± 2.4
Nb-Ta-rich	As-cast	267.7 ± 13.6
	HPT processed	478.6 ± 3.4

Table 4: Hardness values of the individually cast phases occurring in the 800°C, 1h annealing treatment, before and after HPT processing

Since the newly forming phases at this stage are very similar in size the mechanical behavior can be best envisioned as a composite material. However, in such a material a hard phase usually exists, which constraints the deformation in the softer matrix phase, thus leading to an overall increase in the strength of the material. In this case, both phases are very similar in their hardness (Table 4), thus it is reasonable to observe that the hardness of the composite does not differ strongly from the hardness of the two individual phases.

After the maximum hardness of approximately 530 HV1 is reached for 1h of annealing at 500°C, the material starts to get softer again with prolonged heat treatment time. The reason for the hardness maximum at 500°C for 1h of annealing is most likely twofold. First, the above described "hardening by annealing" phenomena is occurring as well, likely even more pronounced given the higher mobility of defects at this temperature. Secondly, while a phase decomposition is already occurring at this temperature, the changes in the phase chemistry after just 1h of annealing are not strong yet (see Figure 5 a) and c)) – Therefore solid solution strengthening in both occurring phases should still be significant. However, after 100h the phase decomposition is much more pronounced leading to a strongly decreased contribution of atomic size misfit to the solid solution hardening in both individual phases, which then results in the lower hardness of this microstructural state. A less important factor is the onset of grain growth (Figure 4 c)), which also could offset the hardness contribution by annealing (either due to a change in the defect structure or due to grain-boundary dislocation interactions, as described above).

D.4.3 Changes in tensile properties

Many materials processed by HPT techniques show extraordinarily high mechanical strengths but often only a moderate amount of plasticity [49]. Especially the tensile ductility is usually limited, which is often related to low strain hardening in these materials, which would help to prevent an early localization of deformation [49,50]. Several strategies exist to potentially gain better ductility, usually centered around gaining a higher strain hardening rate. This, for instance, could be achieved by introducing a bi-modal grain size distribution or nanoparticles, which could promote the accumulation of dislocations. Furthermore, a high density of twins should also improve the ductility of SPD processed materials [49,51]. However, since in the HPT processed TiZrNbHfTa alloy none of these microstructural features are found, the reason for the high ductility must lie elsewhere. For instance, it was shown that a higher ductility in SPD materials may also result from a

change in deformation mechanism or that a change in the grain boundary state could possibly influence the mechanical properties [51]. Valiev et al. [52] reported that it was possible for severely deformed copper and titanium to have both high tensile strength and high ductility. They related this to a possible change in the primary deformation mechanism, from dislocation and/or twinning mediated deformation for the coarse grained material to possibly grain boundary sliding or enhanced grain rotation for the nc materials.

It also has to be noted that the grain size of the as-received state is relatively large in comparison to the typical diameter of a tensile sample (approximately 500 μm) and therefore the tested samples might not be completely representative of the coarse-grained, polycrystalline material due to the low number of grains. However, the results seem to be in relatively good agreement with existing data on the coarse-grained material in literature performed on standard specimens [21].A closer investigation into the high tensile ductility by measuring the strain rate sensitivity of the TiZrNbHfTa alloy will be the goal of future investigations.

A common strategy to restore some of the limited ductility in HPT processed materials is a subsequent annealing treatment [50]. However, in the case of the TiZrNbHfTa alloy this is no valid approach. As can be seen in Figure 9 d) an annealing treatment at 500°C for 1h leads to a severe embrittlement of the alloy and intercrystalline fracture. The reason for the apparent loss in strength compared to the HPT processed sample likely is also caused by this pronounced embrittlement and an early failure of the specimen in the elastic regime of the tensile test. The change from a ductile fracture mode to an intercrystalline one can have several causes, such as precipitation of a brittle phase at grain boundaries. As can be seen in Figure 4a) and b) the microstructure for this annealing state consists of two phases of similar grain size, so the most likely cause of the transition to an intercrystalline fracture is a weak interface strength between the hcp and the bcc phase.

On the other hand a good strength-ductility ratio also cannot be achieved at higher annealing temperatures. At 800°C the TiZrNbHfTa alloy is more ductile again, as especially can be seen in the large area-reduction occurring during tensile testing, see Table 3). However, the material seems very prone to damage localization, since necking occurs during testing with very little prior uniform elongation. Likely reasons for this behavior can be found in the multi-phase microstructure and a very low work hardening rate. In addition, the tensile strength of this microstructural state is already significantly decreased. The hardness data also shows a similar trend for temperatures exceeding 800°C, see Figure 3a).

D.4.4 Comparison between experiment and simulation

In a previous publication by Senkov et al. [25] it has already been shown, that after heavy cold rolling and subsequent annealing at 800°C for 2 h, the TiZrNbHfTa alloy no longer is a single-phase bcc alloy. Since the entropic contribution to the Gibbs free energy decreases with decreasing temperature it was concluded, that for lower temperatures the observed phase decomposition should occur as well.

In this study the phase decomposition could be observed even for much lower annealing temperatures within very short time frames due to the fast diffusion kinetics in nc materials, caused by the high amount of grain boundaries. Experimental observations and simulated data are generally in good agreement regarding phase formation and temperature.

Considering the phase chemistry however, experiment and simulation are only in partial agreement but the trends are satisfactory (see Table 2). In general, the enrichment of elements (especially in the Nb-Ta rich phase) is more pronounced in the simulated data compared to what could be observed in experiments. The reason for this can be twofold: Firstly, the equilibrium condition has not yet been reached for the annealed specimens, which for instance could be seen when comparing specimen annealed at 500°C for 1h and 100h, where in the latter a more pronounced phase decomposition could be observed (Figure 5 a) and c)). Secondly, the Calphad approach often only leads to results that are in partial agreement with experiments in regards to HEAs, since calculating multi-component phase diagrams is more challenging than for traditional alloys, where it is often sufficient for the thermodynamic database to only focus on the corner of the phase diagram, while for HEAs the database should be valid over the entire composition range [53].

D.5 Summary and Conclusions

In order to evaluate the thermodynamic stability of an equiatomic, single-phase TiZrNbHfTa alloy it was nanostructured by utilizing HPT. The nc samples then were subjected to various annealing treatments and the resulting specimens were investigated comprehensively by electron microscopy, XRD and tensile testing to determine microstructure-property relationships. The results can be summarized as follows:

- HPT-processing of the coarse-grained TiZrNbHfTa alloy results in a significant grain refinement down to a minimum grain size of approximately 50 nm and, without losing the single-phase character, leads to a more than twofold increase in tensile strength up to 1900 MPa.
- After subjecting the nc samples to various heat treatments for temperatures below 1000°C a clear tendency towards a phase decomposition could be observed. For temperatures between 800°C and 900°C the TiZrNbHfTa alloy decomposes mostly into two different bcc phases (Nb-Ta and Zr-Hf rich). For lower temperatures a second Zr-Hf-rich phase with a hcp crystal structure can occur as well.
- The phase decomposition also heavily impacts the mechanical performance of the alloy. While after HPT processing the alloy possesses excellent mechanical strength and good ductility, annealing can lead to a severe embrittlement of the alloy.
- The experimentally observed phases are in good agreement with the predictions by thermodynamic simulations.

In summary, the presented results shed new light on the occurring phases of the former single-phase TiZrNbHfTa alloy and their impact on the mechanical properties. In addition, the initially single-phase alloy might constitute a practical basis to synthesize complex nanocomposite structures. The volume fraction of the individual phases could be tailored by selecting the appropriate annealing time and temperature to optimize the trade-off between strength and ductility.

Acknowledgments

This work was supported by the Austrian Science Fund FWF in the framework of Research Project P26729-N19.

D.6 References

[1] J.W. Yeh, S.K. Chen, S.J. Lin, J.Y. Gan, T.S. Chin, T.T. Shun, C.H. Tsau, S.Y. Chang, Nanostructured high-entropy alloys with multiple principal elements: Novel alloy design concepts and outcomes, Adv. Eng. Mater. 6 (2004) 299–303.

[2] M.H. Tsai, J.W. Yeh, High-Entropy Alloys: A Critical Review, Mater. Res. Lett. 2 (2014) 107–123.

[3] D.B. Miracle, O.N. Senkov, A critical review of high entropy alloys and related concepts, Acta Mater. 122 (2017) 448–511. doi:10.1016/j.actamat.2016.08.081.

[4] A. Gali, E.P. George, Tensile properties of high- and medium-entropy alloys, Intermetallics 39 (2013) 74–78.

[5] F. Otto, A. Dlouhý, C. Somsen, H. Bei, G. Eggeler, E.P. George, The influences of temperature and microstructure on the tensile properties of a CoCrFeMnNi high-entropy alloy, Acta Mater. 61 (2013) 5743–5755.

[6] B. Gludovatz, A. Hohenwarter, D. Catoor, E.H. Chang, E.P. George, R.O. Ritchie, A fracture-resistant high-entropy alloy for cryogenic applications, Science 345 (2014) 1153–1158.

[7] O.N. Senkov, C. Woodward, D.B. Miracle, Microstructure and Properties of Aluminum-Containing Refractory High-Entropy Alloys, JOM 66 (2014) 2030–2042.

[8] O.N. Senkov, D. Isheim, D.N. Seidman, A.L. Pilchak, Development of a refractory high entropy superalloy, Entropy 18 (2016) 1–13.

[9] N.D. Stepanov, D.G. Shaysultanov, G.A. Salishchev, M.A. Tikhonovsky, Structure and mechanical properties of a light-weight AlNbTiV high entropy alloy, Mater. Lett. 142 (2015) 153–155.

[10] O.N. Senkov, C.F. Woodward, Microstructure and properties of a refractory NbCrMo0.5Ta0.5TiZr alloy, Mater. Sci. Eng. A. 529 (2011) 311–320.

[11] Y. Zhang, T.T. Zuo, Z. Tang, M.C. Gao, K. A. Dahmen, P.K. Liaw, Z.P. Lu, Microstructures and properties of high-entropy alloys, Prog. Mater. Sci. 61 (2014) 1–93.

[12] J.W. Yeh, Physical Metallurgy of High-Entropy Alloys, JOM 67 (2015) 2254–2261.

[13] J.W. Yeh, S.-J. Lin, T.-S. Chin, J.-Y. Gan, S.-K. Chen, T.-T. Shun, C.-H. Tsau, S.-Y. Chou, Formation of simple crystal structures in Cu-Co-Ni-Cr-Al-Fe-Ti-V alloys with multiprincipal metallic elements, Metall. Mater. Trans. A. 35 (2004) 2533–2536.

[14] J.W. Yeh, Alloy design strategies and future trends in high-entropy alloys, JOM 65 (2013) 1759–1771.

[15] J.W. Yeh, Recent progress in high-entropy alloys, Ann. Chim. Sci. Des Mater. 31 (2006) 633–648.

[16] E.J. Pickering, N.G. Jones, High-entropy alloys: a critical assessment of their founding principles and future prospects, Int. Mater. Rev. 61 (2016) 184-202.

[17] L.R. Owen, E.J. Pickering, H.Y. Playford, H.J. Stone, M.G. Tucker, N.G. Jones, An assessment of the lattice strain in the CrMnFeCoNi high-entropy alloy, Acta Mater. 122 (2017) 11–18.

[18] O.N. Senkov, J.M. Scott, S. V. Senkova, D.B. Miracle, C.F. Woodward, Microstructure and room temperature properties of a high-entropy TaNbHfZrTi alloy, J. Alloys Compd. 509 (2011) 6043–6048.

[19] O.N. Senkov, J.M. Scott, S. V. Senkova, F. Meisenkothen, D.B. Miracle, C.F. Woodward, Microstructure and elevated temperature properties of a refractory TaNbHfZrTi alloy, J. Mater. Sci. 47 (2012) 4062–4074.

[20] G. Dirras, J. Gubicza, A. Heczel, L. Lilensten, J.-P. Couzinié, L. Perrière, I. Guillot, A. Hocini, Microstructural investigation of plastically deformed Ti20Zr20Hf20Nb20Ta20 high entropy alloy by X-ray diffraction and transmission electron microscopy, Mater. Charact. 108 (2015) 1–7.

[21] G. Dirras, L. Lilensten, P. Djemia, M. Laurent-Brocq, D. Tingaud, J.P. Couzinié, L. Perrière, T. Chauveau, I. Guillot, Elastic and plastic properties of as-cast equimolar TiHfZrTaNb high-entropy alloy, Mater. Sci. Eng. A. 654 (2016) 30–38.

[22] G. Dirras, H. Couque, L. Lilensten, A. Heczel, D. Tingaud, J.P. Couzinié, L. Perrière, J. Gubicza, I. Guillot, Mechanical behavior and microstructure of Ti20Hf20Zr20Ta20Nb20 high-entropy alloy loaded under quasi-static and dynamic compression conditions, Mater. Charact. 111 (2016) 106–113.

[23] J.P. Couzinié, L. Lilensten, Y. Champion, G. Dirras, L. Perrière, I. Guillot, On the room temperature deformation mechanisms of a TiZrHfNbTa refractory high-entropy alloy, Mater. Sci. Eng. A. 645 (2015) 255–263.

[24] O.N. Senkov, S.V. Senkova, D.B. Miracle, C. Woodward, Mechanical properties of low-density, refractory multi-principal element alloys of the Cr–Nb–Ti–V–Zr system, Mater. Sci. Eng. A. 565 (2013) 51–62.

[25] O.N. Senkov, S.L. Semiatin, Microstructure and properties of a refractory high-entropy alloy after cold working, J. Alloys Compd. 649 (2015) 1110–1123.

[26] B. Schuh, F. Mendez-Martin, B. Völker, E.P. George, H. Clemens, R. Pippan, A. Hohenwarter, Mechanical properties, microstructure and thermal stability of a nanocrystalline CoCrFeMnNi high-entropy alloy after severe plastic deformation, Acta Mater. 96 (2015) 258–268.

[27] E.J. Pickering, R. Muñoz-Moreno, H.J. Stone, N.G. Jones, Precipitation in the equiatomic high-entropy alloy CrMnFeCoNi, Scr. Mater. 113 (2016) 106–109.

[28] N.D. Stepanov, D.G. Shaysultanov, M.S. Ozerov, S.V. Zherebtsov, G.A. Salishchev, Second phase formation in the CoCrFeNiMn high entropy alloy after recrystallization annealing, Mater. Lett. 185 (2016) 1–4.

[29] F. Otto, A. Dlouhý, K.G. Pradeep, M. Kubênová, D. Raabe, G. Eggeler, E.P. George, Decomposition of the single-phase high-entropy alloy CrMnFeCoNi after prolonged anneals at intermediate temperatures, Acta Mater. 112 (2016) 40–52.

[30] B. Schuh, B. Völker, V. Maier-Kiener, J. Todt, J. Li, A. Hohenwarter, Phase Decomposition of a Single-Phase AlTiVNb High-Entropy Alloy after Severe Plastic Deformation and Annealing, Adv. Eng. Mater. 19 (2017) 1-10.

[31] R. Pippan, S. Scheriau, A. Hohenwarter, M. Hafok, Advantages and Limitations of HPT: A Review, Mater. Sci. Forum. 584–586 (2008) 16–21.

[32] J.P. Couzinié, G. Dirras, L. Perrière, T. Chauveau, E. Leroy, Y. Champion, I. Guillot, Microstructure of a near-equimolar refractory high-entropy alloy, Mater. Lett. 126 (2014) 285–287.

[33] R. Pippan, S. Scheriau, A. Taylor, M. Hafok, A. Hohenwarter, A. Bachmaier, Saturation of fragmentation during severe plastic deformation, Annu. Rev. Mater. Res. 40 (2010) 319–343.

[34] A.P. Hammersley, S.O. Svensson, M. Hanfland, A.N. Fitch, D. Hausermann, Two-dimensional detector software: From real detector to idealised image or two-theta scan, High Press. Res. 14 (1996) 235–248.

[35] CrystalImpact ; http://www.crystalimpact.com/, Match! Phase Identification from Powder Diffraction, (2016).

[36] G.B. Rathmayr, A. Bachmaier, R. Pippan, Development of a new testing procedure for performing tensile tests on specimens with sub-millimetre dimensions, J. Test. Eval. 41 (2013) 1–12. doi:10.1520/JTE20120175\r10.1016/j.msea.2012.09.061;

[37] MathWorks, MatLab, (2017). https://de.mathworks.com/.

[38] Thermo-Calc Software, http://www.thermocalc.com/media/35873/tchea10_extended_info_bh.pdf, [accessed 05 July 17], (2017).

[39] G. Bracq, M. Laurent-Brocq, L. Perriére, R. Pirés, J.M. Joubert, I. Guillot, The fcc solid solution stability in the Co-Cr-Fe-Mn-Ni multi-component system, Acta Mater. 128 (2017) 327–336.

[40] A. Takeuchi, T. Wada, Y. Zhang, MnFeNiCuPt and MnFeNiCuCo high-entropy alloys designed based on L10 structure in Pettifor map for binary compounds, Intermetallics 82 (2017) 107–115.

[41] R.Z. Valiev, R.K. Islamgaliev, I. V. Alexandrov, Bulk nanostructured materials from severe plastic deformation, Prog Mater Sci. 45(2): 2000 103-189.

[42] X. Huang, N. Hansen, N. Tsuji, Hardening by Annealing and Softening by Deformation in Nanostructured Metals, Science 312 (2006) 249–251.

[43] E. Ma, T.D. Shen, X.L. Wu, Nanostructured metals: less is more., Nat. Mater. 5 (2006) 515–6.

[44] R.Z. Valiev, N.A. Enikeev, M.Y. Murashkin, V.U. Kazykhanov, X. Sauvage, On the origin of the extremely high strength of ultrafine-grained Al alloys produced by severe plastic deformation, Scr. Mater. 63 (2010) 949–952.

[45] T.D. Shen, R.B. Schwarz, S. Feng, J.G. Swadener, J.Y. Huang, M. Tang, J. Zhang, S.C. Vogel, Y. Zhao, Effect of solute segregation on the strength of nanocrystalline alloys: Inverse Hall-Petch relation, Acta Mater. 55 (2007) 5007–5013.

[46] O. Renk, A. Hohenwarter, K. Eder, K.S. Kormout, J.M. Cairney, R. Pippan, Increasing the strength of nanocrystalline steels by annealing: Is segregation necessary?, Scr. Mater. 95 (2015) 27–30.

[47] R.L. Fleischer, Substitutional solution hardening, Acta Metall. 11 (1963) 203-209.

[48] C.P. Brittain, R.W. Armstrong, G.C. Smith, Hall-Petch dependence for ultrafine grain size electrodeposited chromium, Scr. Metall. 19 (1985) 89–91.

[49] E. Ma, Eight routes to improve the tensile ductility of bulk nanostructured metals and alloys, JOM 58 (2006) 49–53.

[50] Y. Wang, M. Chen, F. Zhou, E. Ma, High tensile ductility in a nanostructured metal., Nature 419 (2002) 912–915.

[51] R.Z. Valiev, Y. Zhu, Recent Findings in Superior Strength and Ductility of Ultrafine-Grained Materials, Trans. Mat. Res. Soc. Japan 318 (2015) 309–318.

[52] R.Z. Valiev, I. V Alexandrov, Y.T. Zhu, T.C. Lowe, Paradox of strength and ductility in metals processed by severe plastic deformation, J. Mater. Res. 17 (2002) 5–8.

[53] F. Zhang, C. Zhang, S.L. Chen, J. Zhu, W.S. Cao, U.R. Kattner, An understanding of high entropy alloys from phase diagram calculations, Calphad Comput. Coupling Phase Diagrams Thermochem. 45 (2014) 1–10.